Ore Geology Reviews 76 (2016) 463–503

Contents lists available at ScienceDirect

Ore Geology Reviews

journal homepage: www.elsevier.com/locate/oregeorev

The Ranger uranium deposit, northern Australia: Timing constraints, regional and ore-related alteration, and genetic implications for unconformity-related mineralisation

Roger G. Skirrow [a,*], Julien Mercadier [b], Richard Armstrong [c], Tehani Kuske [a], Etienne Deloule [d]

[a] Geoscience Australia, GPO Box 378, Canberra, ACT 2601, Australia
[b] Université de Lorraine, CNRS, CREGU, GeoRessources, UMR 7359, Boulevard des Aiguillettes, B.P. 239, F-54506 Vandoeuvre-lès-Nancy, France
[c] PRISE, Australian National University, ACT 2600, Australia
[d] Centre de Recherches Pétrographiques et Géochimiques, UMR 7358, CNRS, Université de Lorraine, 15 rue Notre Dame des Pauvres, BP 20, 54501 Vandoeuvre-lès-Nancy, France

ARTICLE INFO

Article history:
Received 9 December 2014
Received in revised form 19 August 2015
Accepted 1 September 2015
Available online 7 September 2015

Keywords:
Uranium
Ranger 1 deposit
Unconformity-related uranium deposits
Pine Creek Orogen
Geochronology
Hydrothermal alteration

ABSTRACT

The Ranger 1 unconformity-related uranium deposit in the Northern Territory of Australia is one of the world's largest uranium deposits and has ranked in the top two Australian producers of uranium in recent years. Mineralisation at the Ranger, Jabiluka and other major unconformity-related deposits in the Alligator Rivers Uranium Field (ARUF) occurs in Paleoproterozoic metamorphic basement rocks immediately beneath the unconformity with the Paleo- to Mesoproterozoic McArthur Basin.

The sites of uranium mineralisation and associated alteration at the Ranger 1 deposit (Number 3 orebody) were fundamentally controlled by reactivated shear zones that were initiated during the regional Nimbuwah tectonothermal event. The timing of shearing at medium metamorphic grade was constrained by ion microprobe U–Pb dating of zircons in two pegmatites, one weakly foliated (1867.0 ± 3.5 Ma) and another that is unfoliated and cuts the shear fabric (1862.8 ± 3.4 Ma). The younger age of ~1863 Ma represents the minimum age of D1 shearing during the Nimbuwah event at the Ranger 1 deposit (Number 3 orebody). Titanite within veins of amphibole-plagioclase-apatite yielded an ion microprobe U–Pb age of 1845.4 ± 4.2 Ma, which represents a previously unrecognised hydrothermal event in the ARUF. Based on previous data, retrograde hydrothermal alteration during D2 reactivation of D1 shear zones is interpreted to have occurred at ~1800 Ma during the regional Shoobridge tectonothermal event.

Detailed paragenetic observations supported by whole-rock geochemical data from the Ranger 1 deposit (Number 3 orebody) reveal a sequence of post-D2 hydrothermal events, as follows. (1) Intense magnesium-rich chlorite alteration and brecciation, focussed within schists of the Upper Mine Sequence in the Cahill Formation. (2) Silicification of Lower Mine Sequence carbonate rock units and overlying schist units, comprising quartz ± Mg-foitite (tourmaline) ± muscovite ± pyrite ± marcasite, and rare uraninite (early U1). (3) Formation of main stage uranium ore and heterolithic breccias including clasts of olivine–phyric dolerite, with breccia matrix composed of uraninite (U1), Mg-chlorite ± Mg-foitite and minor pyrite and chalcopyrite. (4) A second generation of uraninite (U2) veinlets with disordered graphitic carbon and quartz of hydrothermal origin. (5) Late-stage veinlets of massive uraninite (U3). As inferred in a previous study and confirmed herein, olivine–phyric dolerite dykes at Ranger are mineralised and chloritised, and are geochemically similar to the regional Oenpelli Dolerite. A maximum age for uranium mineralisation at the Ranger 1 deposit is therefore set by the age of the Oenpelli Dolerite (~1723 Ma).

In-situ ion microprobe U–Pb analysis of texturally oldest U1 uraninite yielded a discordia array with a $^{206}Pb/^{238}U$–$^{207}Pb/^{235}U$ upper intercept age of 1688 ± 46 Ma. The oldest individual ion microprobe ^{207}Pb–^{206}Pb age is 1684 ± 7 Ma whereas the oldest age determined by in-situ electron microprobe chemical dating of U1 uraninite is ~1646 Ma. Another sample containing both U1 and U2 uraninite yielded discordant data with a $^{206}Pb/^{238}U$–$^{207}Pb/^{235}U$ upper intercept age of 1421 ± 68 Ma. When the $^{207}Pb/^{206}Pb$ ages are considered the data are suggestive of U2 uraninite formation and possible resetting of the U1 age between ~1420 Ma and ~1040 Ma. All ion microprobe analyses of U1 and U2 uraninite indicate variable and possibly repeated lead loss. In contrast ion microprobe U–Pb dating of the third generation of uraninite (U3) yielded several near-concordant analyses and a $^{206}Pb/^{238}U$–$^{207}Pb/^{235}U$ upper intercept age of 474 ± 6 Ma. This age is supported by electron microprobe chemical ages of U3 uraninite between 515 Ma and 385 Ma.

* Corresponding author.
E-mail address: roger.skirrow@ga.gov.au (R.G. Skirrow).

http://dx.doi.org/10.1016/j.oregeorev.2015.09.001

The new results constrain the timing of initial uranium mineralisation at the Ranger 1 deposit (Number 3 orebody) to the period ~1720 Ma to ~1680 Ma, which just overlaps with a previous U–Pb age of 1737 ± 20 Ma for uraninite-rich whole-rock samples. Our results are consistent with individual laser-ICPMS $^{207}Pb/^{206}Pb$ and chemical ages of uraninite as old as 1690–1680 Ma reported from other deposits and prospects in the ARUF.

Whole-rock geochemical data in this study of the Ranger 1 deposit (Number 3 orebody) and in other studies in the ARUF demonstrate that zones of intense chloritisation associated with uranium mineralisation experienced large metasomatic gains of Mg, U, Co, Ni, Cu and S and losses of Si, Na, Ca, Sr, Ba, K, Rb, Y and the light REE. More broadly in the ARUF, a regionally extensive illite–hematite ± kaolinite-bearing 'paleoregolith' zone in basement beneath the McArthur Basin exhibits depletion of about half of its uranium as well as major losses in Na, Sr, Pb, Ba and minor losses of Mg. These features together with new petrographic observations suggest this zone is a regional sub-McArthur Basin alteration zone produced by interaction with diagenetic or hydrothermal fluids of primary basinal origin, rather than representing a low-temperature paleo-weathering zone before the deposition of the McArthur Basin, as previously suggested.

Based on these results and a synthesis of previous work, a new multi-stage model is proposed for the Ranger 1 ore-forming mineral system that may apply to other major unconformity-related uranium deposits in the ARUF and which may be used for targeting new deposits in the region. As in most recent models, oxidised diagenetic brines within the McArthur Basin are envisaged as crucial in mobilising uranium. However, a different architecture of fluid flow is proposed involving the sub-unconformity regional basement alteration zone as a preferential source of leached uranium. Possibly driven by convection during regional magmatism at ~1725–1705 Ma, oxidised basinal brines were drawn downwards and laterally through fault networks and fractures in the regional sub-unconformity alteration zone, leaching uranium from hematite-altered basement rocks. Simultaneously within deeper and lateral parts of the hydrothermal system, Mg-metasomatism produced chloritic alteration and brines with increased acidity and silica content (from the desilicification of the basement rock), analogous to processes described in sub-seafloor hydrothermal systems. Silicification occurred locally (e.g., Ranger deposit) within upflow zones of convective systems due to decreases in temperature and/or pressure of the brines and/or CO_2 generation during carbonate dissolution. Interruptions to convection during transient regional extensional or strike-slip tectonic events resulted in generalised lateral and downwards flow of fluids from the McArthur Basin through deepened zones of sub-unconformity alteration, transferring leached uranium into reactivated shear zones within the basement. The main stage of uraninite precipitation at the Ranger deposit and elsewhere in the ARUF is proposed to have occurred between ~1720 Ma and ~1680 Ma as a result of reduction of oxidised and evolved basin-derived ore fluids during reaction with pre-existing Fe^{2+}-bearing minerals and/or mixing of the ore fluids with basement-reacted silica-rich brines.

A second, volumetrically minor but locally high-grade, stage of uraninite mineralisation was associated with hydrothermal disordered carbon and quartz of presently unknown origin. Available data suggest formation between ~1420 Ma and ~1040 Ma. Almost a billion years later at ~475 Ma, fluids capable of mobilising uranium again resulted in uraninite (U3) deposition as sparse veinlets in the Ranger deposit, representing the first documentation of uranium mineralisation of this age in the region.

1. Introduction

Unconformity-related uranium deposits are the world's most important sources of high grade uranium ore, recoverable at low cost (OECD, 2014, recoverable at <USD$40/kg U). Deposits associated with the Proterozoic Athabasca Basin in Saskatchewan, Canada, and with the northern McArthur Basin in Australia host the largest known resources of unconformity-related uranium, with global resources of this type totalling 765 000 t U (OECD, 2014; reasonably assured + inferred resource categories, recoverable at <USD$260/kg U). The Athabasca deposits occur within both the basin and the metamorphic basement rocks, and also at the unconformity itself; the highest grade ores occur at and above the unconformity, with average grades of up to 14% U (OECD, 2014). In contrast the known unconformity-related deposits in the Alligator River Uranium Field (ARUF) in Australia are hosted by Archean-Proterozoic basement of the Pine Creek Orogen (PCO) and are of generally lower grade than the Canadian counterparts. Nevertheless, total uranium resources are large: the undeveloped Jabiluka deposit contains 141 640 t U_3O_8 @ 0.48% U_3O_8 (as at 31 December 2014, Energy Resources Australia announcement, 6 February 2015; cutoff 0.15% U_3O_8, reserves plus resources), and the Ranger 1 deposit is one of the largest uranium deposits in the world, having a total endowment (past production plus remaining resource) of 130 000 t U (MODAT, 2011, www.nt.gov.au). Recent exploration including >47 km of drilling since 2009 in the Ranger 3 Deeps zone has identified a new resource of 34 867 t U_3O_8 @ 0.28% U_3O_8 (as at 31 December 2014, Energy Resources Australia announcement, 6 February 2015; cutoff 0.15% U_3O_8, measured + indicated + inferred resources). A major challenge for exploration and mining companies is the discovery of high grade uranium ores within the ARUF, of similar quality to deposits in the Athabasca region.

Targeting of unconformity-related uranium deposits and higher grade mineralisation can benefit from an understanding of the processes that resulted in uranium deposition, not only at the deposit scale but also within the regional- to crustal-scale 'mineral system' (Wyborn et al., 1998). This comprises the full set of geological conditions leading to a coincidence in time and space of (1) source(s) of uranium and other ore-forming components such as mineralising fluids, (2) energy source(s) to 'drive' hydrothermal fluid flow, (3) structural architecture favourable for the transfer of fluids and for the transport and deposition of large quantities of uranium, and (4) gradients in physico-chemical conditions favourable for the deposition of uranium ores. The identification and mapping of each of these necessary components of the mineral system will allow predictive targeting of mineralisation, potentially in areas not previously known to be mineralised.

A general consensus has emerged for the involvement of basin-derived brines in the formation of unconformity-related uranium deposits, building on the pioneering 'diagenetic-hydrothermal' model of Hoeve and Sibbald (1978). There is less agreement on the sources of uranium in both the basin-hosted and basement-hosted deposits (Kyser and Cuney, 2009), with some advocating a basin source (e.g., Wilde and Wall, 1987; Wilson and Kyser, 1987; Fayek and Kyser, 1997; Polito et al., 2004, 2005, 2011) and others proposing a basement rock source of uranium (e.g., Hecht and Cuney, 2000; Derome et al., 2003; Richard et al., 2010; Mercadier et al., 2012, 2013a). Published

genetic models can be grouped into two sets — involving either a basin source or a basement source of uranium. Within each set, variations have been proposed for basin/unconformity-hosted and basement-hosted deposits that propose either fluid mixing or (single) fluid-rock reaction as key processes in uranium mineralisation (Fig. 1). The model of Hoeve and Sibbald (1978) for basin/unconformity-hosted deposits involves a basin source of uranium and fluid mixing at and above the unconformity, between oxidised basinal brines and a fault-controlled ascending reduced fluid that was of originally basinal (oxidised) origin. The latter fluid was proposed to have been reduced via reaction with the basement (Fig. 1A). Variants of this mixing model involving basinal uranium sources and basement-derived reduced fluids were presented by Wilson and Kyser (1987); Kotzer and Kyser (1995); Fayek and Kyser (1997); Cloutier et al. (2010), and Ng et al. (2013) (see also Jefferson et al., 2007 and references therein). Models for the basement-hosted deposits that involve a basinal source of uranium reaction propose reaction of descending, oxidised, uranium-bearing, basinal brines with reduced basement rocks in and around fault zones to deposit uranium via redox and/or other chemical reactions (Fig. 1B; Wilde and Wall, 1987; Wilde et al., 1989; Polito et al., 2004, 2005, 2011; Jefferson et al., 2007 and references therein). The possibility of mixing of the descending U-bearing brine with a reduced, ascending, fluid beneath the unconformity was also suggested by Wilde et al. (1989) (Fig. 1B, shown with arrow labelled '± reduced fluid'). Although reverse fault settings are proposed in most models, Cui et al. (2012) envisaged formation of basement-hosted deposits via downflow during normal faulting and extension, as illustrated in Fig. 1B. Alternative, ascending-fluid, models also have been presented for some basement-hosted deposits (e.g., Fisher et al., 2013, for the Ranger 1 deposit, ARUF).

Models proposing a basement source of uranium generally involve percolation of basin-derived Na-rich brines into basement, exchange of Ca for Na, leaching of uranium, and then mixing of the Na- and Ca–U-rich brines to precipitate uranium (Fig. 1C; Derome et al., 2005; Mercadier et al., 2010, 2012; Richard et al., 2010). A variation of this model was suggested by Derome et al. (2003) for the ARUF in which basement-sourced uranium was first transferred into the basin by calcic brines and then transported back into the basement by Na–Ca–U-bearing brines where mixing occurred with an ascending, reduced, low salinity fluid (Fig. 1D). It is interesting to note that low salinity fluids have not been reported from unconformity-related uranium deposits in the Athabasca region. A similar two-stage process of uranium transfer from basement to basin then convective downflow of U-bearing fluids into the basement was envisaged by Solomon and Groves (1994).

Although altered U-bearing minerals have been identified as possible sources in both basin and basement rocks (e.g., monazite, Hecht and Cuney, 2000), no studies have so far recognised large scale alteration zones representing the uranium-leached source rocks and definitively linked them genetically to the uranium deposits. Identification of such zones, while challenging, could provide important exploration guides towards mineralisation. The so-called 'paleoregolith' zones that occur regionally and directly beneath the unconformity of the Athabasca Basin (Macdonald, 1980) and in the ARUF where they are uranium-depleted (e.g., Miller et al., 1992) could represent parts of the uranium mineral systems, and so it is surprising these zones have received little research attention.

The age of mineralisation in unconformity-related uranium deposits is also a contentious issue yet is crucial to constrain robust genetic and exploration models. Unfortunately most of the available mineral geochronometers in unconformity-related uranium hydrothermal systems such as uraninite (U–Pb–Th isotope system) and white mica (K-Ar and $^{40}Ar/^{39}Ar$ isotope systems) are susceptible to resetting and therefore record, in most cases, minimum ages of mineralisation. In the ARUF U–Pb isotope dating of uraninite by LA-ICPMS and 'chemical' dating of uraninite by electron microprobe (based on the chemical concentrations of U, Th and Pb) have revealed individual spot ages as old as 1685 Ma ($^{207}Pb/^{206}Pb$ ages) and 1691 Ma (chemical age) for the major Jabiluka deposit and King River prospect, respectively (Polito et al., 2005, 2011). A wide range of younger U–Pb ages, to ~500 Ma, have also been reported for uraninite in other deposits of the ARUF (e.g., Polito et al., 2004, 2005, 2011). Application of whole-rock Sm-Nd and Rb-Sr isotopic dating gave isochron ages for initial uraninite formation of 1615 ± 50 Ma (Sm-Nd for the Nabarlek deposit, 1619 ± 30 Ma

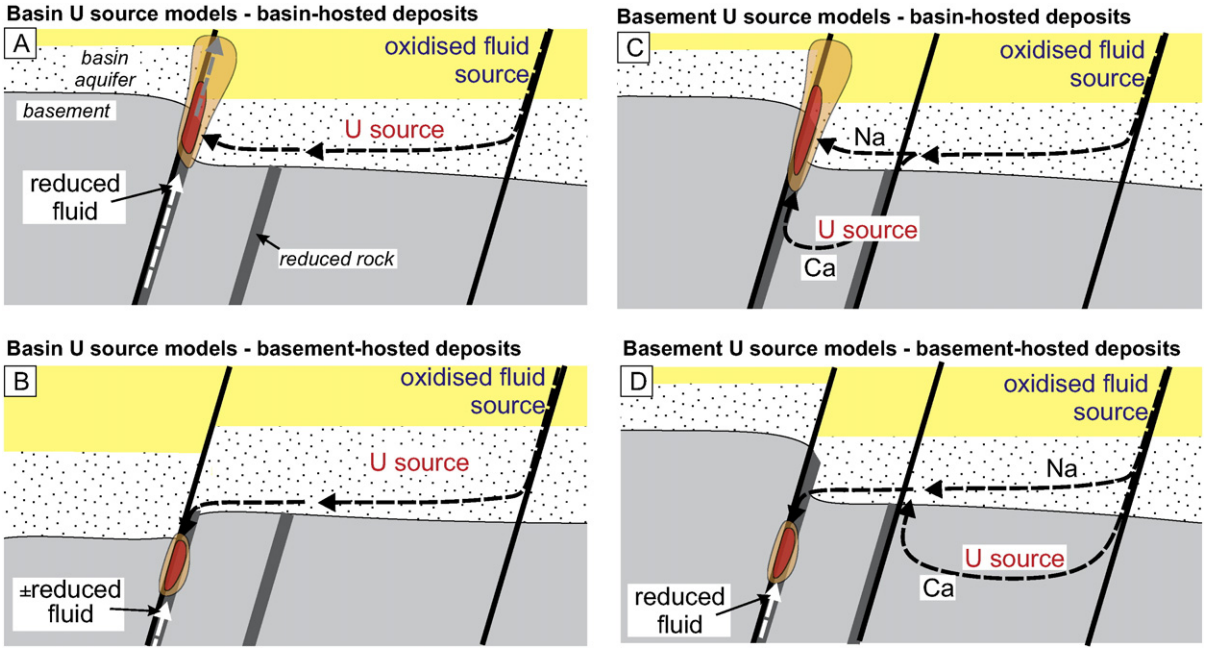

Fig. 1. Schematic summary of published genetic models of unconformity-related uranium deposits. See text for references.

(Rb-Sr) for the Nabarlek deposit and 1614 ± 132 Ma (Sm-Nd) for the Jabiluka deposit (Maas, 1989). Problematically, however, these ages are inconsistent with an age of 1737 ± 20 Ma determined for the major Ranger deposit from U–Pb isotope analysis of uraninite-rich whole-rock samples (Ludwig et al., 1987) and also differ from the $^{40}Ar/^{39}Ar$ ages of sericite and illite dated from these deposits (Polito et al., 2004, 2005, 2011). It should be noted, however, that there may be technical limitations in applying the $^{40}Ar/^{39}Ar$ dating technique to very fine-grained minerals (see Clauer, 2013 for a review). The age of earliest uranium mineralisation in the ARUF therefore has not been tightly constrained, which has limited the confidence of any correlations between uranium mineralisation and regional tectonic and thermal events.

@To address key gaps in knowledge of unconformity-related uranium systems outlined above, we undertook a study of the Ranger 1 deposit and aspects of its broader ore-forming mineral system. Despite its size and significance as the only operating mine in the district, there have been few published studies of the Ranger 1 deposit since the 1980s. The Ranger 1 deposit comprises the mined-out Number 1 orebody and the Number 3 orebody located ~2 km to the north, which was mined as an open pit until 2013. Mining of deeper extensions of the Number 3 orebody, the 'Ranger 3 Deeps' zone, has been deferred indefinitely (www.energyres.com.au, media release 11 June 2015). Early studies of the Numbers 1 and 3 orebodies (e.g., Eupene et al., 1975; Ewers and Ferguson, 1980; Donnelly and Ferguson, 1980; Kendall, 1990) were followed by various studies of the geochronology and isotopic characteristics of uranium deposits in the ARUF, including the Ranger 1 Number 3 orebody (Ludwig et al., 1987; Maas, 1989; Annesley et al., 2002). Structural studies including the Ranger 1 deposit were undertaken by Johnston (1984) and by Hein (2002) on the Number 1 and Number 3 orebodies. Whole-rock geochemical patterns were described by Potma et al. (2012) and Fisher et al. (2013). Oxygen and hydrogen isotope data were reported by Polito et al. (2011) for seven chlorite and quartz samples from the Ranger deposit. Fluid inclusions were investigated in a sample of Kombolgie Subgroup sandstone at the Ranger 1 Number 3 orebody by Derome et al. (2003).

The Ranger 1 Number 3 deposit provides an opportunity to sample some of the deepest known uranium mineralisation in the ARUF, thereby testing and constraining models of descending basin-derived fluids (e.g., Wilde and Wall, 1987; Polito et al., 2011) versus models of ascending ore fluids (e.g., Fisher et al., 2013).

The present study focuses on the relative and absolute timing of tectonic, igneous and hydrothermal events prior to and during formation of the uranium ores. Building on our earlier study of dating hydrothermal alteration in the Ranger 1 deposit (Mercadier et al., 2013b) we present (a) a new and detailed paragenetic event framework, (b) U–Pb ion microprobe geochronology results for zircon in pre-ore syn-tectonic pegmatites and for titanite in pre-ore alteration, (c) ion microprobe U–Pb dating and electron microprobe 'chemical' dating results for uraninite, and (d) whole-rock geochemical data for the alteration. We also report observations from 'paleoregolith' zones distal from the Ranger deposit and show that these areas may represent zones of basinal fluid inflow into the basement and possible sources of at least some of the U and Mg concentrated in the Ranger and other uranium deposits. The results of the study confirm the importance of pre-ore structural and chemical architecture of the basement in controlling the location of uranium mineralisation, as recognised in previous studies of the ARUF. Finally, the results are integrated into a new mineral system model involving multi-stage 3-dimensional fluid flow within the basin and basement, which differs significantly from previous models of uranium ore formation in the ARUF. We demonstrate that a simple single-stage model of descending oxidised basinal brines reacting with reduced basement rocks cannot adequately account for the complex sequence of hydrothermal and tectonic events leading to ore formation at the Ranger deposit nor in other unconformity-related uranium deposits in the ARUF.

2. Regional geological setting

The Pine Creek Orogen (PCO) is an Archean to Mesoproterozoic inlier in the Northern Territory that hosts Australia's major unconformity-related uranium deposits (Fig. 2). Neoarchean basement outcropping in the Nimbuwah and Central Domains of the PCO comprises ~2670–2510 Ma granite and gneiss (Worden et al., 2008; Hollis et al., 2009, 2011; Hollis and Wygralak, 2012). Neoarchean felsic orthogneiss of the Nanambu Complex to the west of the Ranger and Jabiluka deposits has yielded a magmatic age of 2520 ± 3 Ma (Hollis et al., 2009). Neoarchean rocks in the Nimbuwah Domain were unconformably overlain by, or in faulted contact with, ~2020 Ma to ~1870–1860 Ma continental to marine basins and volcanic rocks of the Woodcutters Supergroup and then by the Cahill Formation and Nourlangie Schist (previously known as the Myra Falls Metamorphics). The Cahill Formation comprises siliciclastic to pelitic schists (including carbonaceous units), carbonate and calc-silicate rocks, and amphibolites, and is the host sequence for the Ranger, Jabiluka and several other uranium deposits in the ARUF. The Nourlangie Schist hosts the Nabarlek deposit (Hollis and Wygralak, 2012).

The Nimbuwah orogenic event at ~1865–1855 Ma resulted in metamorphism to medium grade in the Nimbuwah Domain and in lower grades in the Central Domain, and was accompanied by deformation and granitoid intrusions of the Nimbuwah Suite (Worden et al., 2008; Hollis et al., 2011; Hollis and Wygralak, 2012). Pegmatites at the Ranger deposit with a monazite U–Pb age of 1847 ± 1 Ma (Annesley et al., 2002) have been interpreted to record the latest stage of the Nimbuwah event (Worden et al., 2008) or to have been emplaced after the Nimbuwah event (Hollis and Wygralak, 2012).

Volcanism and renewed basin formation at ~1829–1825 Ma (Edith River Group, El Sherana Group) was accompanied and outlasted by magmatism of the Cullen Suite and Jim Jim Suite between ~1835 and ~1818 Ma (Fig. 2; Worden et al., 2008). A low-metamorphic grade tectonothermal overprint at ~1780 Ma was originally defined as the Shoobridge event by Stuart-Smith et al. (1993) in the central PCO on the basis of whole-rock Rb-Sr isotope data. However, the widespread Rb-Sr and K-Ar muscovite, biotite and whole-rock ages of ~1800 Ma in the Nimbuwah Domain (Page et al., 1980) together with a new U–Pb monazite age of 1800 ± 9 Ma from the Ranger deposit led Mercadier et al. (2013b) to suggest that the Shoobridge event could have extended from as early as ~1800 Ma to ~1780 Ma. Shearing, retrograde metamorphism in the greenschist facies, and gold mineralisation accompanied the Shoobridge event (Mercadier et al., op. cit.).

The Kombolgie Subgroup, the basal part of the Katherine River Group within the McArthur Basin in the eastern PCO (Fig. 2), was deposited unconformably on the pre-1818 Ma basement and comprises a generally flat-lying sequence of quartz sandstone, conglomerate, and minor mafic volcanic and volcaniclastic rocks (Hollis et al., 2011; Hollis and Wygralak, 2012). This maximum age of ~1818 Ma is consistent with detrital zircon U–Pb data indicating a maximum depositional age of ~1810–1820 Ma for the Kombolgie Subgroup (Page, 1996a). The mafic volcanic units (Nungbalgarri Volcanic Member; Gilruth Volcanic Member) are strongly altered in places (Needham, 1988) and may be time-equivalents of the 1780–1760 Ma Siegal Volcanics in other parts of the McArthur Basin (Scott et al., 2000; Polito et al., 2011). The Kombolgie Subgroup was unaffected by the low metamorphic grade regional Shoobridge event which we have proposed commenced at ~1800 Ma (Mercadier et al., 2013b), setting this as a likely maximum age for the Kombolgie Subgroup. This unit is, however, locally

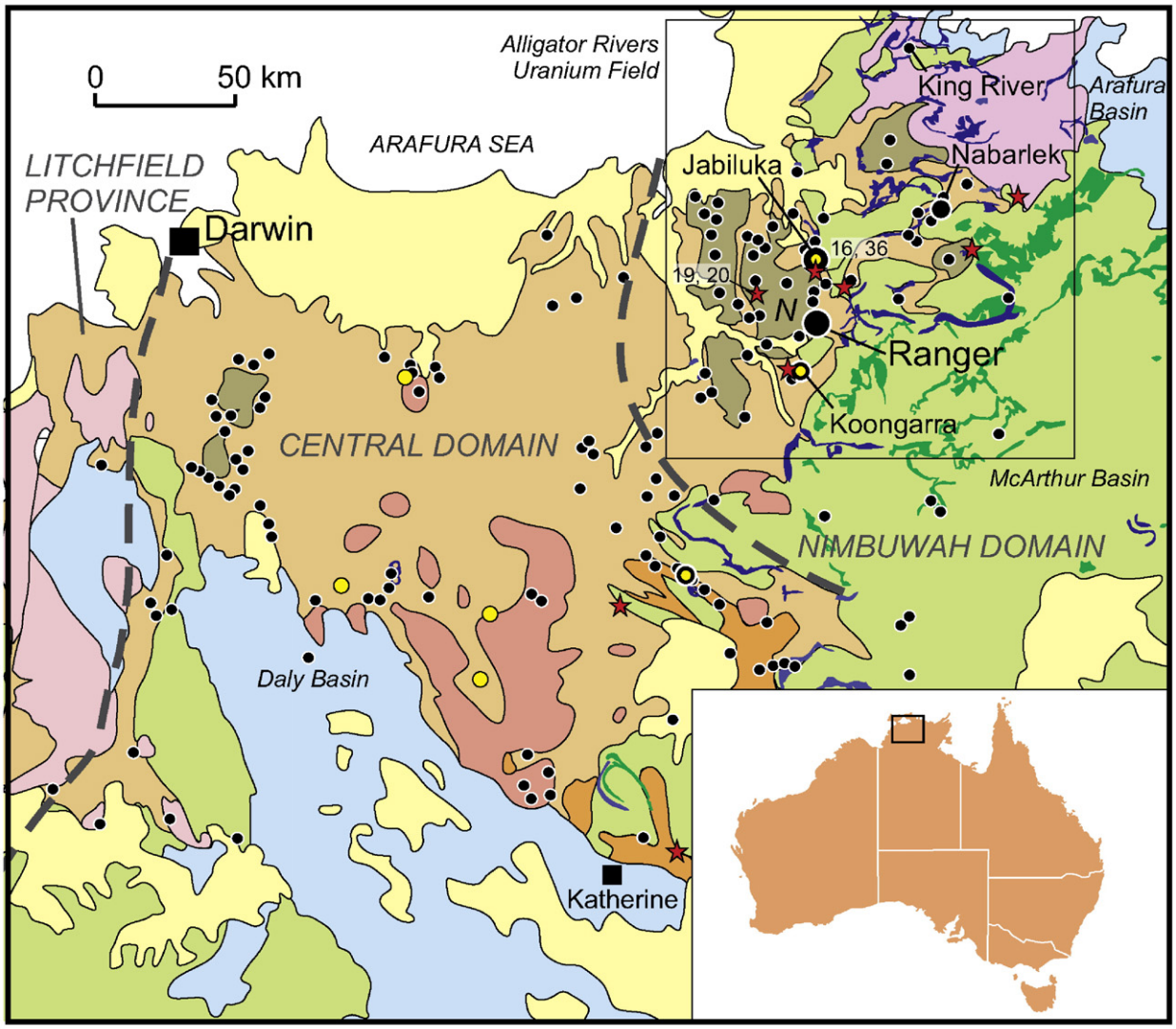

Mesozoic to Cenozoic basins

Paleozoic basins

Oenpelli Dolerite (~1723 Ma)

Post-1800 Ma Paleo-Mesoproterozoic basins;
Mafic volcanic units in Kombolgie Subgroup of McArthur Basin

~1829-1825 Ma Edith River Group, El Sherana Group

~1835-1818 Ma Cullen Suite, Jim Jim Suite granites

~1863-1853 Ma Allia Suite, Wagait Suite granitoids

~1867-1862 Ma Nimbuwah Suite granitoids

~2020-1860 Ma metasedimentary and metaigneous rocks;
(including Cahill Formation in Nimbuwah Domain)

Neoarchean (including Nanambu Complex (N) in Nimbuwah Domain)

Large uranium deposit

Medium sized uranium deposit

Uranium occurrence or small deposit

Significant gold deposit

'Paleoregolith' sub-unconformity alteration profile (Miller et al., 1992)

Fig. 2. Location and geology of the Pine Creek Orogen, comprising the Nimbuwah, Central and Litchfield Domains, and the location of the Ranger 1 deposit within the Alligator Rivers Uranium Field. Modified from Hollis and Wygralak (2012) with map data for the Oenpelli Dolerite (Page, 1996b) and mafic volcanic units in the McArthur Basin from Thorne et al. (2014). The Neoarchean Nanambu Complex is labelled 'N'. Sites of 'paleoregolith' profiles studied by Miller et al. (1992) are shown as red stars; some of the samples from these sites investigated in this study are labelled'19, 20′ (samples 83120019, 83120020, Granite Hill, latitude −12.5341°S longitude 132.9038°E) and'16, 36′ (samples 83120016, 85121036, Pancontinental drillhole GT5, latitude −12.5070°S longitude 132.9013°E).

Table 1
Conventional (TIMS) U–Pb baddeleyite data for syenitic differentiate in the Oenpelli Dolerite from the Nabarlek uranium deposit, reproduced from Page (1996b)*.

Analysis No.	Weight (μg)	U ppm	Pb total	$^{206}Pb/^{204}Pb$	$^{206}Pb/^{204}Pb$	$^{208}Pb/^{206}Pb \pm 2\sigma$	$^{206}Pb/^{238}U \pm 2\sigma$	$^{200}Pb/^{235}U \pm 2\sigma$	$^{207}Pb/^{206}Pb$ age (Ma) $\pm 2\sigma$
1220	5.5	417.5	123.0	4364	0.0068	0.3035 ± 76	4.418 ± 110	0.10555 ± 21	1724 ± 4
1222	4.0	449.8	127.8	4360	0.0105	0.2917 ± 45	4.239 ± 66	0.10539 ± 21	1721 ± 4
1223	5.0	281.1	83.8	2286	0.0103	0.3016 ± 44	4.438 ± 68	0.10672 ± 47	1744 ± 8
1224	7.0	554.2	159.2	18,089	0.0121	0.2978 ± 31	4.338 ± 45	0.10564 ± 15	1726 ± 3
1225	4.6	461.0	142.2	992	0.0074	0.3019 ± 36	4.367 ± 53	0.10492 ± 21	1713 ± 4

Each analysis included between 2 and 5 baddeleyite grains.
Processing Pb blank 9-12 pg. Composition: 206/204 = 17.97; 207/204 = 15.55; 208/204 = 37.71.
Geoscience Australia site ID: 88126035.
Geoscience Australia sample ID: 88126035.
Location: latitude 12.306579° south, longitude 133.322072° (GDA94).
Sample number: 1463499, collected by R. Page.
Nabarlek deposit, drillhole DDH98, depth 46–47 m (same sample with whole-rock geochemistry, Table 3), from latitude −12.306579 longitude 133.322072 (Page, 1996b).
* Data unavailable at present from original source.

chloritised, quartz-veined, steeply dipping, and is offset by reverse faults at the Koongarra, Ranger and Jabiluka uranium deposits (Snelling, 1990; Hein, 2002; Polito et al., 2005). The timing of this reverse faulting is not known but the region was subjected to a number of post-Kombolgie compressive events including those at ~1755–1730 Ma (Bull and Rogers, 1996) and at ~1690–1665 Ma (Scott et al., 2000). Diagenetic processes commenced in the Kombolgie Subgroup as early as 1798 ± 13 Ma based on a $^{40}Ar/^{39}Ar$ plateau age for diagenetic illite, and occurred at temperatures of up to ~230°C (Polito et al., 2004, 2005; Beaufort et al., 2005; Hiatt et al., 2007).

The Kombolgie Subgroup and basement were intruded by the Oenpelli Dolerite, which has a baddeleyite U–Pb age of 1723 ± 6 Ma from a drill hole at the Nabarlek uranium deposit (Fig. 2; Page, 1996b). The data for this widely cited sample are reproduced in Table 1, due to their current unavailability from the original source and because of the significance of this age for the timing of uranium mineralisation (see below). Sweet et al. (1999) suggested a minimum age of 1720 Ma for the Kombolgie Subgroup, based on ages of the West Branch Volcanics (~1712–1705 Ma) at the top of the Katherine River Group in the McArthur Basin, the ~1720 Ma Jimbu Microgranite which intrudes the upper Katherine River Group, and correlations with the southern McArthur Basin. Collectively these ages constrain the timing of deposition of the Kombolgie Subgroup to <1800 Ma and >1723 Ma; further work is required to better define the age of this important sequence, including the ages of the Nungbalgarri and Gilruth volcanics.

Remnants of Paleozoic basins are preserved in parts of the southern Central Domain (Daly Basin), Litchfield Province, and northeastern Nimbuwah Domain (Arafura Basin; Fig. 2).

3. Unconformity-related uranium deposits of the ARUF

The geology of unconformity-related uranium deposits in the ARUF has been described in numerous previous studies (see Polito et al., 2011; Ahmad and Munson, 2013; and references therein), and only a summary of salient features is presented here. The Ranger, Jabiluka and Koongarra deposits (Fig. 2) are hosted by the Cahill Formation, which in the vicinity of these deposits comprises variably altered pelitic to psammitic and locally carbonaceous schists (e.g., quartz–biotite–feldspar–muscovite ± garnet ± amphibole ± graphite). Thin carbonate units (partly silicified) are present within the schists at Jabiluka (Polito et al., 2005), and a lower carbonate-rich unit is also present at the Ranger 1 deposit where it hosts up to one-third of the ore in the Ranger 3 Deeps zone (Energy Resources Australia, www.energyres.com.au). By comparison, the Nabarlek deposit (Fig. 2) is hosted by interlayered pelitic to psammitic schist (with rare graphite and garnet) and amphibolite, possibly correlated with the Nourlangie Schist (Wilde and Wall, 1987; Polito et al., 2004; Hollis et al., 2009; Hollis and Wygralak, 2012). Unlike the Athabasca Basin no major uranium mineralisation has been reported within the overlying Kombolgie Subgroup of the McArthur Basin.

A strong structural control is evident in all of the major deposits and at prospects such as King River, which is hosted by faults cutting Archean gneisses and the Nimbuwah Complex (Polito et al., 2011). The Koongarra deposit lies in the hangingwall of a silicified reverse fault with Kombolgie Subgroup sandstones in the footwall, well below the level of the regional unconformity (Snelling, 1990). The Jabiluka deposit occurs within brecciated and sheared Cahill Formation rocks; the contact of these mineralised basement rocks with the Kombolgie Subgroup rocks dips moderately in the area of the deposit (Polito et al., 2005) such that the sandstones are present at a structural level below that of the regional unconformity. The Nabarlek deposit is situated along a fault inferred to cut the Oenpelli Dolerite with reverse displacement (Wilde and Wall, 1987; Polito et al., 2004). Outcrops and pit exposures of the Kombolgie Subgroup in the western parts of the Ranger 1 Number 3 orebody indicate post-Kombolgie fault activity (Kendall, 1990). As at Koongarra and Jabiluka, these volumes of Kombolgie Subgroup occur below the level of the regional unconformity. At the Jabiluka, Ranger and Koongarra deposits, most uranium mineralisation occurs as disseminations and veinlets in sheet-like zones, lenses and breccia zones subparallel to the strong foliation within intensely chloritized schists. The breccias are commonly cemented by chlorite and uraninite. These altered schists have been described as lithostratigraphic units but at the Ranger deposit there is evidence that some of the chloritized schist zones represent altered broad shear zones sub-parallel to compositional layering within siliciclastic metasedimentary rocks (Hein, 2002; Mercadier et al., 2013b; see also below).

Uraninite (pitchblende) is the primary ore mineral with generally minor coffinite and brannerite, accompanied in most deposits by minor pyrite, galena and chalcopyrite. Gold is present at levels of >100 ppb to several ppm in some deposits including Jabiluka, Koongarra and Ranger, where higher gold grades tend to correlate with higher uranium grades, but ore grade uranium mineralisation does not necessarily contain elevated gold (Hegge et al., 1980; Potma et al., 2012; Fisher et al., 2013).

It has long been recognised that uranium mineralisation is associated with intense chloritization, at least at the Jabiluka, Ranger and Koongarra deposits. Hydrothermal white-mica (illite and sericite) alteration generally occurs in outer zones as replacements of feldspar and other minerals. However, at the Nabarlek deposit uranium mineralisation was mined from zones of massive white mica, which grades outwards to zones of

chlorite and white mica alteration (Wilde and Wall, 1987; Polito et al., 2004). Nevertheless, in all cases documented there is a consistent spatial pattern of zoning in chlorite compositions whereby distal chlorite that replaced biotite, amphibole and garnet has Fe-rich compositions whereas chlorite proximal to uranium mineralisation has Mg-rich compositions (Ewers and Ferguson, 1980; Binns et al., 1980a; Wilde and Wall, 1987; Polito et al., 2004, 2005; Beaufort et al., 2005). In detail there are complexities in the timing of Fe- and Mg-chlorite alteration that are not yet fully resolved. Minor hematite is associated with sericite alteration and uraninite at the Nabarlek deposit (Polito et al., 2004) although Wilde and Wall (1987) describe a hematitic 'shell' outside the ore zone at this deposit. Hematite also occurs with sericite–chlorite–uraninite at the Jabiluka deposit (Polito et al., 2005), and is present with chloritisation at the Ranger deposit, as described below. Less well documented and understood are the zones of silicification observed at or near all of the major deposits, represented by jasper or chert after carbonate at Jabiluka and Ranger (Hegge et al., 1980; Gustafson and Curtis, 1983; Polito et al., 2005), silicified zones adjacent to the Oenpelli Dolerite at Nabarlek (Wilde and Wall, 1987; Polito et al., 2004), and silicified fault breccia at the Koongarra deposit (Snelling, 1990). Silicification is also present in the Kombolgie Subgroup (Derome et al., 2003, 2007).

Fluid characteristics were summarised by Polito et al. (2011) based on fluid inclusion, stable isotope and mineral chemical constraints. An enduring problem with the fluid inclusion studies is that hydrothermal quartz generally did not form during the main stages of uraninite deposition, with rare exceptions (e.g., Jabiluka and King River; Polito et al., 2004, 2011). According to Polito et al. (2011) the available stable isotope, fluid inclusion and mineralogical data are consistent with uranium deposition at ~200°C, involving fluids with oxygen and hydrogen isotopes compositions typical of basinal brines that evolved from marine pore fluids, confirming the hypothesis presented by Derome et al. (2007) based on the halogen contents of the fluid inclusions in hydrothermal quartz. Fluid inclusions in hydrothermal quartz in the Kombolgie Subgroup described as either syn-ore (Derome et al., 2003, 2007) or post-ore (Polito et al., 2004, 2005, 2011) trapped fluids with a wide range of salinities and Ca:Mg:Na ratios, and recorded homogenisation temperatures from ~100°C up to 280 ± 50°C. Similar ranges have been reported in hydrothermal quartz within some of the basement-hosted uranium deposits, and can be explained by fluid mixing (Derome et al., 2003, 2007; Polito et al., 2004, 2005, 2011). However, the significance of the high-temperature low-salinity and low-temperature high-salinity end-members with respect to uranium mineralising processes remains unclear. Also enigmatic are some calculated $\delta^{18}O_{(fluid)}$ values of up to 8.6 per mil for post-ore chlorite in the Kombolgie Subgroup (Jabiluka); up to 8.2 per mil for post-ore chlorite in the basement (Jabiluka); and up to 12.1 per mil for uraninite at Nabarlek (Polito et al., 2004, 2005). These are 'heavier' than the compositions of the basinal brine ore fluids proposed by Polito et al. (2004, 2005, 2011), and may indicate the involvement of basement-derived or basement-reacted fluids at least during post-ore hydrothermal stages. The roles of basin versus basement as sources of metals in the uranium ores of the ARUF was also investigated by Maas (1989) using Sm-Nd isotopes. Their data are consistent with basinal sources of Nd at Jabiluka, Nabarlek and Ranger if an age of 1614–1616 Ma is assumed, but an older, basement (Cahill Formation and Archean), contribution is required at Ranger if the age of ~1737 Ma of Ludwig et al. (1987) is assumed for mineralisation (Maas, 1989).

4. Sub-unconformity alteration ('paleo-regolith') zone

4.1. Previous work

Basement rocks in many areas of the ARUF have been affected by distinctive hematitic and/or clay-rich alteration in a sub-horizontal zone extending downwards from the unconformity beneath the Kombolgie Subgroup for up to ~50 m, first described by Needham (1988) and Miller et al. (1992) (Fig. 2). These authors interpreted the alteration as a paleo-regolith zone that formed before the deposition of the sedimentary basin, and overprinted by diagenetic processes. Similar features in basement beneath the Athabasca Basin also were interpreted to represent paleo-regolith with diagenetic overprinting (Macdonald, 1980). We prefer to use the non-genetic term 'sub-unconformity alteration' to describe such zones.

The widespread sites described by Needham (1988) and Miller et al. (1992) (Fig. 2) represent different zones within the regional sub-unconformity alteration and so a composite profile was constructed by these workers. The alteration is developed in a variety of basement rocks including granitic gneisses of the Nanambu Complex. It comprises (a) an upper zone directly beneath the unconformity with abundant disseminated very fine grained hematite and illite; kaolinite and diaspore occur as an uppermost sub-zone in two localities but this sub-zone appears to be absent in other areas; and (b) a chloritic zone that is inferred to grade downwards into less altered protolith rock. Illite in the hematitic zone has crystallinity consistent with formation at anchizone conditions typical of diagenetic environments (Miller et al., 1992). The study of Beaufort et al. (2005) revealed two types of illite above the unconformity in the Kombolgie Subgroup and below, and within basement distal from uranium mineralisation: coarser diagenetic illite with crystallinity indicating formation at ~200°C, and finer, later, hydrothermal illite with crystallinity typical of formation at ~180°C. No kaolinite was identified by Beaufort et al. (2005), nor was there any evidence of clays with crystallinity typical of low-temperature weathering environments. Although the kaolinite and diaspore reported by Miller et al. (1992) could represent relicts of a paleo-weathering profile, existing data suggest that the principal clay in the hematitic alteration zone is illite of hydrothermal and/or diagenetic origin.

Two types of chlorite were distinguished in altered rocks beneath the hematitic zone: an Fe-rich variety replacing biotite of similar Mg:Fe ratio and a finer grained magnesian type (Miller et al., 1992) that may be equivalent to the sudoite documented by Beaufort et al. (2005).

The REE-bearing mineral parageneses within the basin and basement rocks are of particular interest due to their significance for understanding ore-forming processes and for exploration. Gaboreau et al. (2005) and Beaufort et al. (2005) documented the occurrence and systematic spatial variation in the mineralogy and composition of LREE-bearing aluminium-phosphate-sulfate (APS) minerals in samples of the lower Kombolgie Subgroup and of basement rocks close to the unconformity, at sites proximal and distal from the major uranium deposits in the ARUF. Examples of the APS minerals replacing monazite were reported in both studies. Gaboreau et al. (2005) suggested that APS minerals distal from uranium mineralisation have Sr- and SO_4-rich compositions (near svanbergite end-member) whereas those proximal to mineralisation have REE- and P-rich compositions (near florencite end-member). The APS minerals were interpreted by Gaboreau et al. (2005) as the product of hydrothermal and/or diagenetic fluids within hydrological systems linked to the formation of the uranium deposits, although they did not refer to the 'paleo-regolith' zone nor described in detail the locations of samples in this context. Similar APS mineralogy and compositional variations with respect to mineralisation has been described near uranium deposits in the Athabasca Basin region (Gaboreau et al., 2007), with florencitic compositions (associated with ore-forming fluids) overprinting svanbergitic zones within APS minerals (Adlakha and Hattori, 2015). Arsenic-rich florencitic APS compositions are inferred to have formed during pre-basin paleo-weathering.

Whole-rock geochemical analyses were reported by Miller et al. (1992) for samples of hematitic and chloritic alteration and for the metamorphic protoliths. A sub-set of these data has been re-plotted in Fig. 3 to

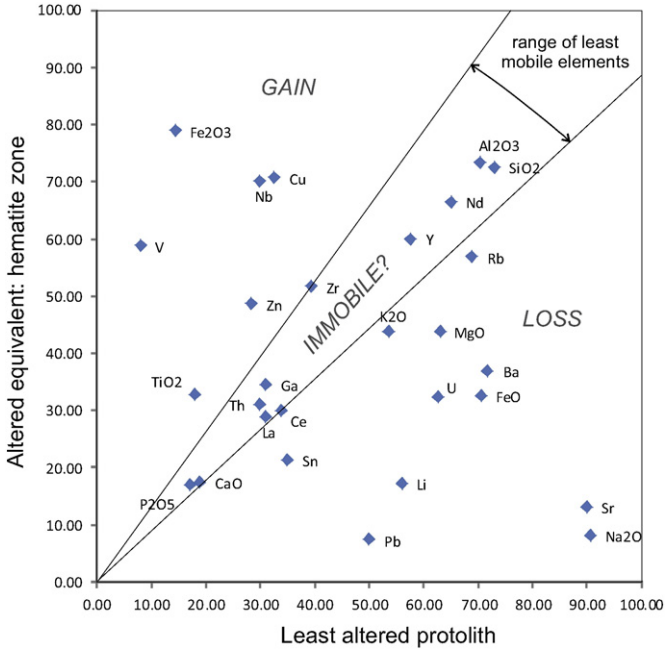

Fig. 3. Diagram of gains and losses of chemical components (method of Grant, 1986) during metasomatism in the sub-unconformity alteration zone, based on the whole-rock geochemical data of Miller et al. (1992) for drill hole GT5, 1 km south–southeast of the Jabiluka deposit (location shown in Fig. 2). Weight percent concentrations, scaled to values of less than 100, of least altered Nanambu Complex metasedimentary rock (average of 2 samples, depths 70–81 m) compared with scaled values for hematite–illite altered equivalents (average of 3 samples, depths 19–22 m below surface). Least mobile elements such as Zr, Y, Th and Al have been selected to define a field between the two diagonal 'isocons' of little or no mass transfer, labelled 'range of least mobile elements'. Elements plotting below this field show mass losses from the rock during alteration, whereas those above this field show mass gains.

show metasomatic gains and losses of elements in hematitic alteration relative to least altered equivalent protolith, using the method of Grant (1986). The data of Miller et al. (1992) show that the hematitic zone was strongly depleted in Na_2O, Sr, Pb and Li, and moderately depleted in U, Ba and MgO relative to the least altered granitic gneiss. Importantly, approximately half of the U was removed from the hematised zone. The REE, Y, Th, Zr, P_2O_5, Al_2O_3, SiO_2, K_2O and Rb were relatively immobile, whereas V, Cu, Zn and Nb were moderately to strongly enriched in the hematitic zone. Iron as Fe_2O_3 increased dramatically at the expense of FeO, indicating oxidation during hematitic alteration. In contrast, chloritic alteration in this sub-unconformity environment resulted in only minor metasomatism (Miller et al., 1992).

4.2. New results

In order to better understand the spatial distribution of key phases such as monazite and the APS minerals in the 'paleo-regolith', we undertook petrography on the original thin sections of the Miller et al. (1992) study, stored at Geoscience Australia. This work was supported by scanning electron microscope (SEM) energy-dispersive spectrometric (EDS) identification and analysis of key minerals.

Two textural and compositional end-member types of monazite are present in altered granitic gneisses of the basement (Table 2): Th-rich generally coarser subhedral monazite and fine grained anhedral Th-poor monazite. Reconnaissance analysis of 24 monazite grains by EDS indicates a range from <2 to ~15 weight percent ThO_2, and <1.2 weight percent UO_2. The Th-rich monazite is interpreted to be of igneous or medium grade metamorphic origin based on its texture and composition. The Th-poor fine grained anhedral monazite is broadly similar in texture and composition to low-Th monazite within the alteration halo of the Ranger 1 Number 3 orebody, which contains <0.4 weight percent ThO_2 (Mercadier et al., 2013b). The Ranger monazite yielded an ion probe U–Pb age of 1800 ± 9 Ma and was interpreted to be of retrograde metamorphic or hydrothermal origin. Attempts to date the low-Th monazite in the sub-unconformity alteration using the SHRIMP ion probe were unsuccessful due to low uranium contents.

Our observations of LREE-bearing APS minerals replacing monazite confirms the results of Gaboreau et al. (2005) and Beaufort et al. (2005) and additionally demonstrates that this replacement process occurred within the hematitic zone of the sub-unconformity alteration (Fig. 4A). However, several compositions of APS minerals from LREE- to Sr-rich are present at locations 19 and 20 (Fig. 2), which are distal from known major uranium deposits (Fig. 4A, B, Table 2). This points to a possibly more complex spatial pattern of APS mineral compositional variation than proposed by Gaboreau et al. (2005).

Other minerals identified using SEM in the sub-unconformity alteration include: Th–U–Zr–Si-bearing minerals (possibly U-rich thorian zircon and/or U-rich zirconian thorite; a U–Ti mineral intergrown with chlorite (Fig. 4C) and uraninite overgrowing pyrite in the chloritic zone (Fig. 4D); native gold (sample 83120016), barite (83120023, 85121038), and rare Bi-, Pd- and Ir-bearing minerals.

Table 2
Reconnaissance scanning electron microscope analyses (by energy dispersive spectrometry) of representative monazite and APS minerals in sub-unconformity alteration zones, ARUF. Locations shown in Fig. 2.

	Monazite				APS minerals			
Sample	83120019	83120019	83120019	83120019	83120020	83120020	83120020	83120019
Analysis	1	2	3	4	5	6	7	8
Al_2O_3	1.03				29.81	40.01	31.34	33.37
SiO_2	2.15	3.15	1.11	2.76				
P_2O_5	24.4	28.39	30.37	29.12	25.96	26.87	26.85	29.15
CaO	1.13	1.24	1.11	1.77	3.3	3.52	3.52	
Ag_2O	5.85	9.88			3.93			
SO_3					3.14	2.45		
SrO					19.8		9.12	
FeO					4.03	4.71	6.99	4.58
ZrO_2					6.22	6.76	5.86	
La_2O_3	15.79	14.94	14.66	12.51				16.92
CeO_2	28.69	28.54	29.81	25.05	3.81	9.72	5.54	15.97
Nd_2O_3	12.45	13.85	15.6	13.85				
ThO_2			7.34	14.95		4.17	10.77	
K_2O						1.78		

Analyses by energy-dispersive spectrometry using the scanning electron microscope at Geoscience Australia. Weight percent oxides totalled to 100%.
Sample 83120019 from Granite Hill, altered Nanambu Complex, hematite zone, 1.2 m below the unconformity. Pancontinental drillhole GT5, latitude −12.5341°S longitude 132.9038°E (see location, Fig. 2).
Sample 83120020 from Granite Hill, hematite zone, 3.1 m below unconformity. Pancontinental drillhole GT5, latitude −12.5341°S longitude 132.9038°E (see location, Fig. 2).

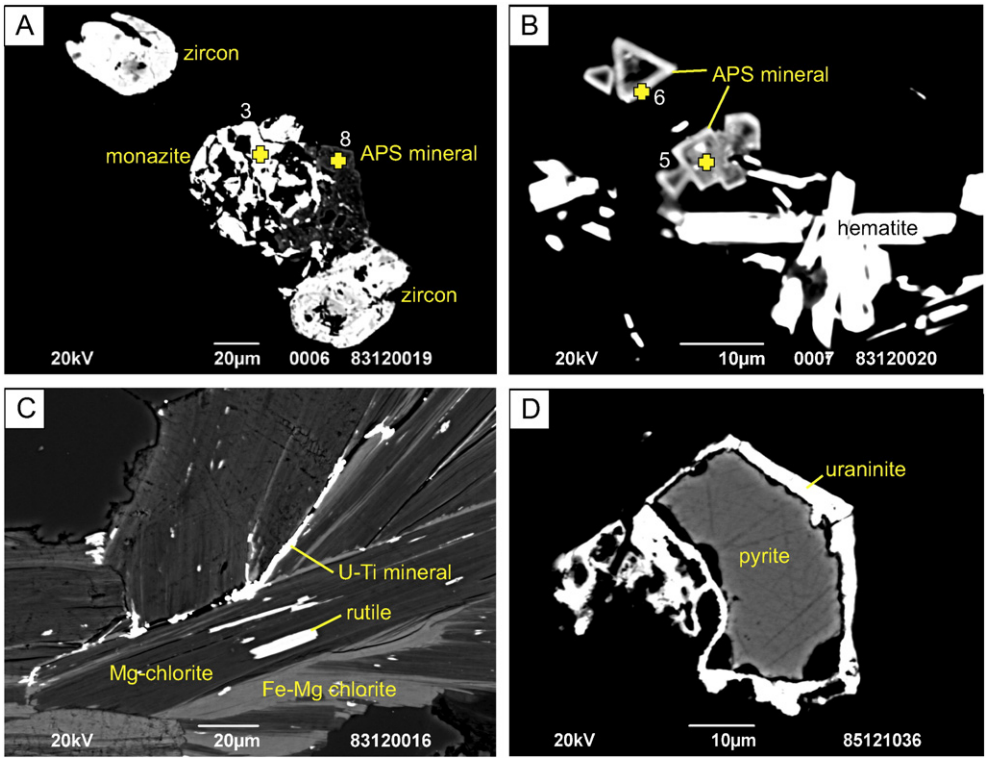

Fig. 4. Sub-unconformity alteration zone, scanning electron microscope images. A. Thorium-rich monazite (EDS analysis 3, Table 1) partly altered to REE-rich APS mineral (EDS analysis 8, Table 1). Sample 83120019, altered Nanambu Complex, hematite zone, 3.1 m below unconformity, from Granite Hill, latitude −12.5341°S longitude 132.9038°E. B. Zoned APS mineral(s) with strontium-rich core (EDS analysis 5, Table 1) and cerium-rich strontium-poor rim (analysis 6, Table 1). Sample 83120020, altered Nanambu Complex, hematite zone, 3.1 m below unconformity, from Granite Hill, latitude −12.5341°S longitude 132.9038°E. C. Uranium-rich titanium-bearing mineral(s) (U:Ti = 0.58 M ratio, from EDS analysis) and rutile in chlorite after biotite. Sample 83120016, altered Nanambu Complex, chlorite zone, 1 km south–southeast of Jabiluka, Pancontinental drillhole GT5, latitude −12.5070°S longitude 132.9013°E. D. Pyrite overgrown by uraninite. Sample 83120016, altered Nanambu Complex, chlorite zone, 1 km south–southeast of Jabiluka, Pancontinental drillhole GT5, latitude −12.5070°S longitude 132.9013°E.

5. Geology, alteration, mineralisation and event history of the Ranger 1 deposit

5.1. Lithostratigraphic and structural context

The Cahill Formation at the Ranger 1 Number 1 and Number 3 orebodies comprises an easterly dipping package of strongly foliated and partly altered biotite–amphibole ± garnet-bearing metasedimentary schists and amphibolites, termed the Hangingwall Sequence, underlain by intensely altered, brecciated and mineralised schists, termed the Upper Mine Sequence (Fig. 5). Carbonaceous (graphitic) zones are present locally. These are underlain by generally dolomite-rich carbonate rock units of the Lower Mine Sequence, which is magnesite rich in shallower parts of the LMS and is variably mineralised and altered to 'chert' and chlorite- and hematite-bearing carbonate (Fig. 5B). The 3-dimensional distributions of lithologies and whole-rock geochemical patterns at the Number 3 orebody were described by Potma et al. (2012) and Fisher et al. (2013), based on company data and new analyses. Most uranium mineralisation occurs within the Upper Mine Sequence in zones elevated in Mg, Cu, Au and Ni and depleted in Na, Ba, K and Ca. Mineralisation extends to more than 500 m depth in the eastern Ranger 3 Deeps zone where it tends to be more Cu-rich and terminates against a major north-trending fault (Potma et al., 2012; Fisher et al., 2013). The results of Potma et al. (2012) and Fisher et al. (2013) also show a gross spatial association between the uranium mineralisation, chlorite-rich rocks in the UMS and LMS, hematitic carbonate in the LMS, and 'chert' in mainly the LMS and also less abundantly in a structurally higher zone (Fig. 5B). Similar patterns were reported for the Number 1 orebody by Potma et al. (2012), and an association of mineralisation with zones of 'thinned' silicified carbonates was also recognised in earlier studies (e.g., Kendall, 1990). Hematitic carbonate is mostly restricted to the northern part of the Number 3 orebody, within an east–west trending trough in the contact between the Upper Mine Sequence and the Lower Mine Sequence (Fisher et al., 2013). The southern boundary of this trough is marked by an east–west trending fault zone. Taken together, we interpret these spatial patterns in mineralogy as a series of nested alteration zones, from distal to proximal as follows: (1) weak to moderately intense sericite–chlorite alteration in mainly the HWS; (2) hematitic and chloritic alteration of LMS carbonate; (3) silicified LMS carbonate and less abundant silicified UMS ('chert'); (4) uranium mineralisation and intense chlorite alteration, within the UMS and LMS.

Based on recent drilling by Energy Resources Australia, relatively high grade uranium mineralisation (e.g., 7 m @ 1.3% U_3O_8, Energy Resources Australia, announcement 20 October 2014) occurs mainly within brecciated UMS rocks and in zones of complex faulting. Some faults with steep east-northeast dips and north–northwest trend show a reverse component of displacement of the east-dipping LMS-UMS contact on east–west sections. While it was beyond the scope of the present study to document and interpret the detailed kinematics of structures, we see this deposit-scale architecture as compatible with dextral strike-slip on the north–northwest striking steep faults. Other kinematics also could have produced the observed geometries. Flexures in these faults where they sole into the shallow-dipping fabric of the UMS, as shown in company cross sections, may have been the locus of dilation and brecciation that controlled the location and grades of uranium mineralisation. Lesser mineralisation also occurs within chloritic 'lenticular schists' deeper within the LMS.

The following sub-sections document new and detailed paragenetic observations of the sequence of deformation and hydrothermal events and mineral assemblages at the Ranger 1 Number 3 orebody, which

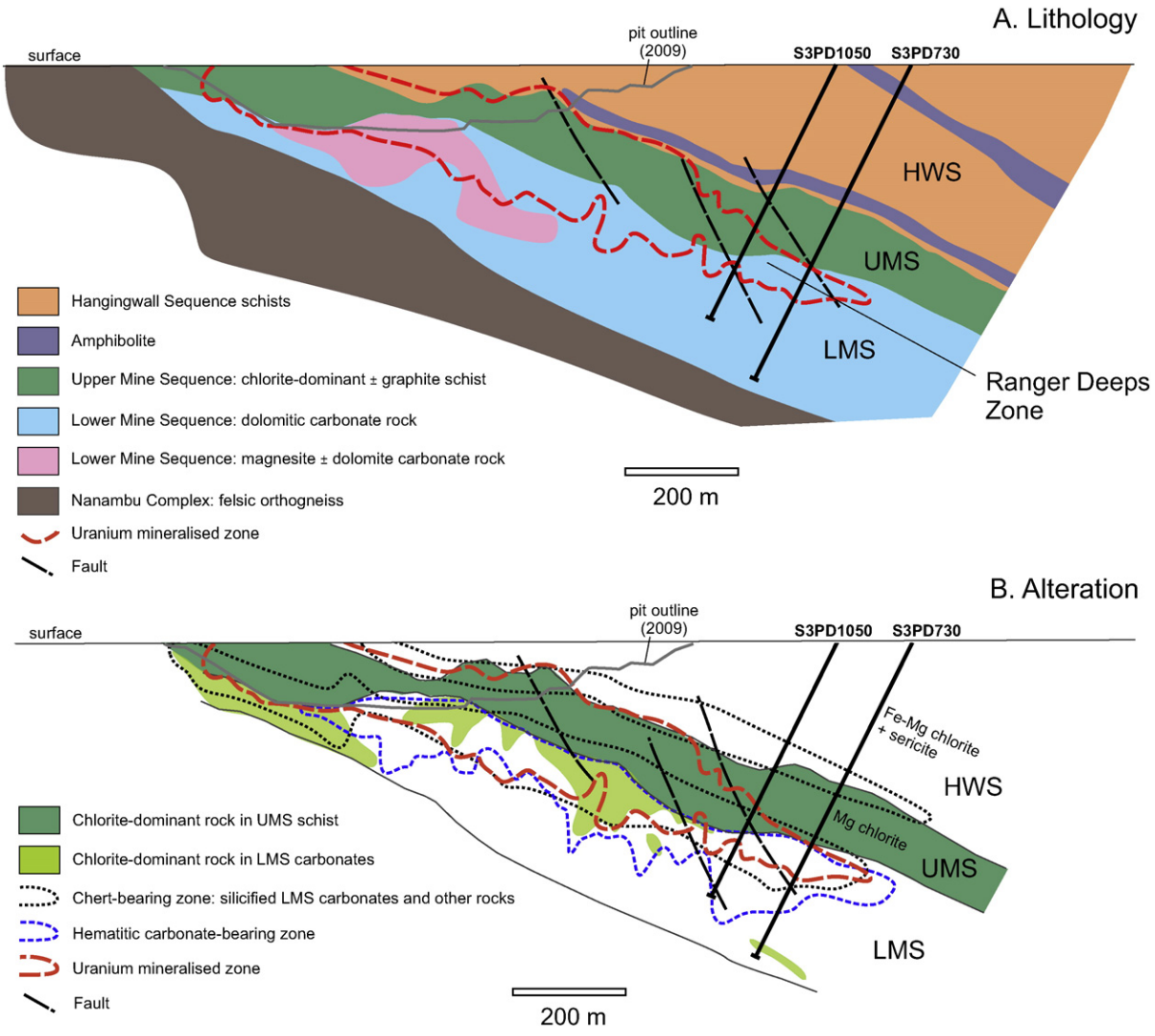

Fig. 5. Generalised east–west cross sections of lithology and alteration, and location of two of the drill holes investigated, at the Ranger 1 Number 3 orebody. A. Lithology, and location of the Ranger 3 Deeps zone. Boundaries between the Hangingwall Sequence (HWS), Upper Mine Sequence (UMS), Lower Mine Sequence (LMS) and Nanambu Complex are from Potma et al. (2012; Fig. 27) at 11666 N, based on ERA company data. Outline of uranium mineralisation is based on a 2D projection of 3D drill hole assay data shown by Potma et al. (2012, Fig. 125). The zone of magnesite within the LMS is generalised from the projected 3D data in Figure 134 of Potma et al. (2012). B. Alteration. Uranium mineralisation and HWS, UMS and LMS boundaries as per Fig. 5A. Outlines of chert-bearing rock and hematitic carbonate-bearing rock are generalised from projections of 3D drillhole data in Figs. 11 and 5, respectively, of Potma et al. (2012).

provide the geological context for the geochronology undertaken in this study. The results are summarised in Fig. 6.

5.2. Medium-grade metamorphism, deformation and pegmatites — Nimbuwah event

Sedimentary rocks of the Cahill Formation at the Ranger 1 deposit were transformed into banded gneisses, schists and banded marble during medium-grade metamorphism and deformation corresponding to the regional Nimbuwah event, designated D1 in this study. Pelitic and psammo-pelitic rocks developed peak metamorphic assemblages that include biotite, amphibole, garnet, graphite and muscovite as well as quartz and feldspar (Fig. 7A). Although there is no evidence of melt generation, millimetre-width compositional banding is well developed in much of the UMS and lower part of the HWS and is characterised by abundant quartz bands with dark ferromagnesian-rich aureoles (Figs. 7A, C, 8D). In places the quartz bands merge with cross-cutting quartz veins, and therefore the quartz bands are interpreted to represent highly deformed quartz vein networks that developed within a broad ductile-brittle shear zone centred on the UMS. The strong tectonic fabric is also defined by alignment of biotite, amphibole, and graphite, and given the intensity of shearing which has the appearance of mylonite in places, is probably sub-parallel to original bedding. Within the banded marble of the LMS, stylolites indicate dissolution of carbonate during and/or after the main medium-grade D1 tectonism.

The timing of this intense shearing has been constrained by dating of pegmatites at Ranger (see Geochronology Results). A range of pegmatite types occur mainly in the HWS and LMS but only relicts are preserved in the more intensely altered and deformed UMS. Highly strained, boudinaged pegmatites occur as lenses within the main medium-grade tectonic fabric (Fig. 8A, B, C), and are strongly recrystallised and highly altered to sericite and chlorite (Fig. 8C). In addition, much less deformed, yet also sericitised and chloritised massive pegmatites cross-cut the main tectonic fabric, and are composed of quartz, feldspar, muscovite, tourmaline, apatite and zircon (Fig. 8A-E). Annesley et al. (2002) also reported the presence of very U-rich monazite and uraninite in pegmatites at the Ranger 1 deposit. These pre-or syn-deformation and late- or post-deformation pegmatite variants therefore bracket the timing of the medium-grade tectonothermal D1 event at Ranger.

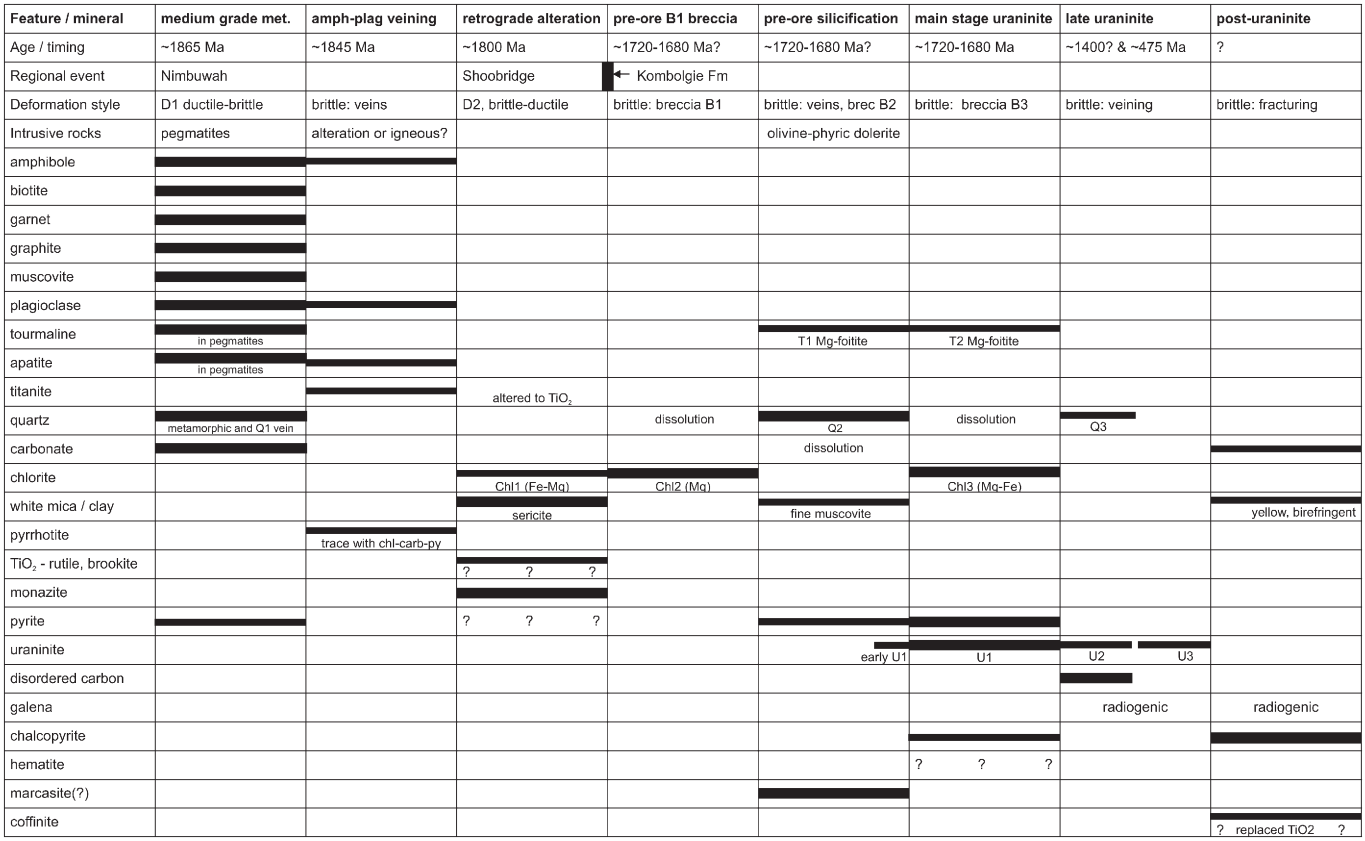

Fig. 6. Paragenetic sequence of minerals and events at the Ranger 1 Number 3 orebody, based on drill hole observations of mainly the Ranger 3 Deeps zone.

5.3. Amphibole-plagioclase-titanite veining

Distinctive dark green massive to banded chloritic intervals of a few centimetres to metres width are common throughout the UMS and LMS (at least 1–2% by volume), and contain abundant rutile or brookite pseudomorphs of titanite euhedra up to 3 mm length (Fig. 9A). Narrow white mica-rich aureoles occur within the host rocks in some places, and there is sparse evidence for local replacement of host rocks. A rare occurrence in drill hole S3PD730 at a depth of 371.2 m contains a vein of coarse-grained amphibole, plagioclase, titanite and apatite with traces of pyrrhotite (Fig. 9B, C), and is interpreted as a less altered equivalent of the chloritic rock with TiO_2 replacements of titanite. Fresh titanite was dated from this interval (see Geochronology Results). Elsewhere, the chloritised veins are observed to cross-cut the medium-grade tectonic fabric, consistent with the geochronology results, but are themselves cut by quartz veins (Fig. 9A) and in places exhibit a weak tectonic foliation ascribed to D2 (see below). Altered fragments of the amphibole-plagioclase-titanite veins are incorporated within mineralised breccias. The amphibole-plagioclase-titanite veins are interpreted to be of hydrothermal origin (Ca-Na-Ti-P metasomatism), based on the presence of sericitic alteration selvages adjacent to the veins, although other origins cannot be ruled out.

5.4. Retrograde alteration and deformation — Shoobridge event

The gneissic banding, foliation and quartz veins that developed during D1 are folded at deposit- to meso- and micro-scales, with associated faulting, during a hydrothermal-deformation event designated D2 in this study. A second foliation is locally developed, particularly in micaceous intervals. Amphibole-plagioclase-titanite veins were probably chloritised initially during D2, when they developed a weak foliation. Amphibolite in the HWS also contains aligned chlorite that replaced biotite and amphibole, probably during the D2 event. The widely varying attitudes of foliation directions reported by Potma et al. (2012) at the Ranger 1 No. 3 deposit are most likely the result of deformation during D2. Hein (2002) also described NE to NNW trending shears with easterly dips and associated folds and C-S2 shear fabrics, which she ascribed to a local D2 event, consistent with the results of this study.

In outer/upper zones tens of metres distal from the intensely chloritised UMS, D2 brittle-ductile fault/shear zones are characterised by 'bleaching' of the dark grey-green biotite- ± amphibole-bearing host rocks where they are intensely altered to sericite, chlorite and accessory very fine-grained monazite (Fig. 8D). Based on composition and texture, the monazite has been interpreted as hydrothermal in origin and yielded an in-situ U–Pb SHRIMP age of 1800 ± 9 Ma (Mercadier et al., 2013b). We therefore correlate the local D2 event with the regional Shoobridge tectonothermal event (Stuart-Smith et al., 1993; Mercadier et al., 2013b). Biotite is replaced by Fe-rich chlorite (Chl1) in these alteration zones associated with D2 deformation, at least in the outer parts of the alteration system at Ranger. This is consistent with the reporting of Fe-chlorite replacing metamorphic biotite in the outer zones at all of the studied unconformity-related uranium deposits in the ARUF (Ewers and Ferguson, 1980; Binns et al., 1980; Wilde and Wall, 1987; Polito et al., 2004, 2005; Beaufort et al., 2005). Within the LMS, later events intensely overprinted and largely obscured the effects of D2.

5.5. Pre-ore B1 breccia and initial Mg-metasomatism

In the Ranger 1 No. 3 deposit, breccia zones are hosted by the UMS. The initial stage of brecciation (B1) was the locus of Mg-rich chloritisation of the host rocks, and infilling of the breccia matrix by highly magnesian chlorite (Chl2; Fig. 10A). Although no major uranium mineralisation has been unambiguously identified with B1 stage brecciation and chloritisation, detailed observations have revealed uraninite replacing

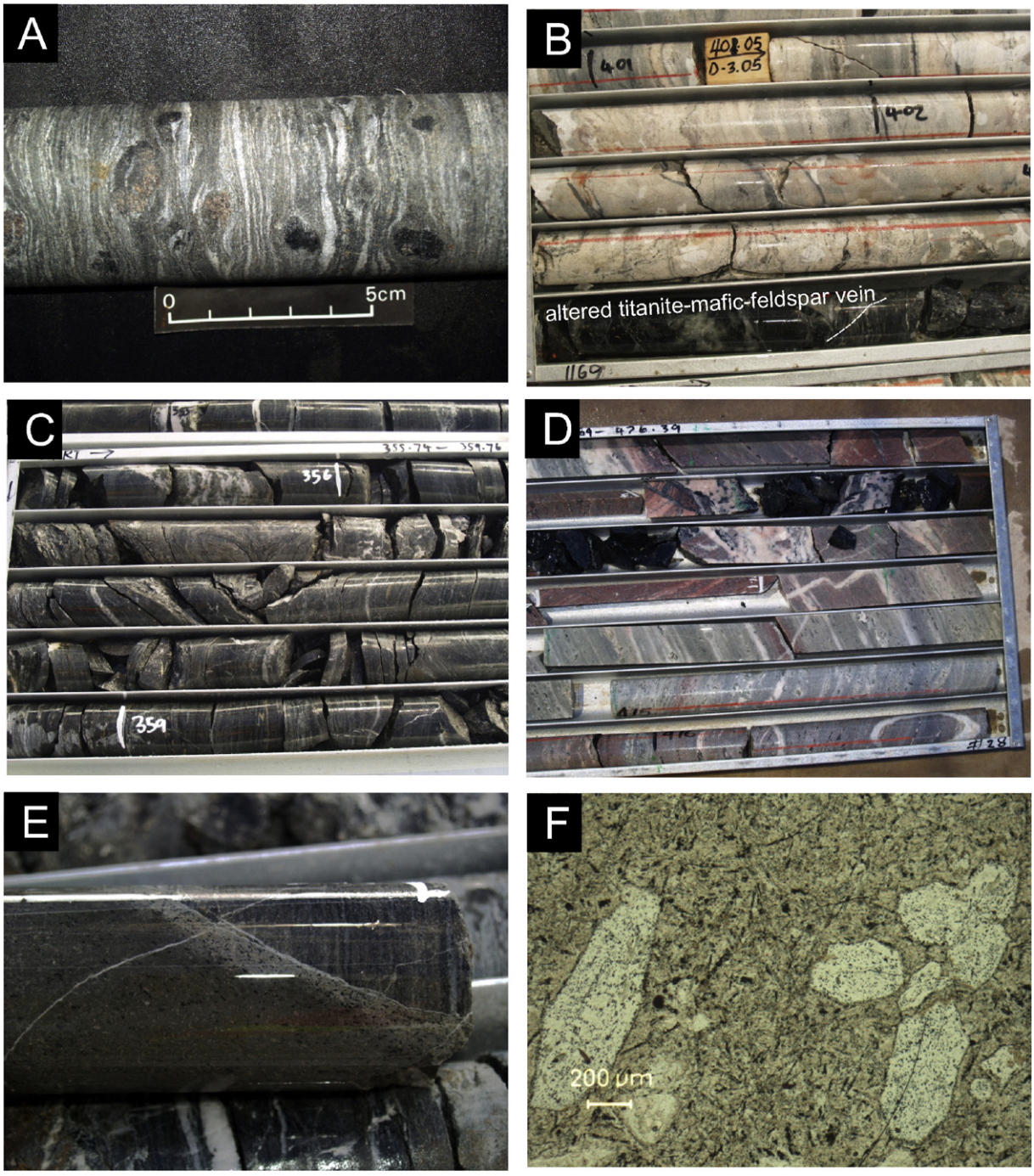

Fig. 7. Host rocks at the Ranger 1 Number 3 orebody. A. Banded (sheared) gneiss with altered garnet porphyroblasts, from LMS near contact with Nanambu Complex. Drillhole S3PD730 611.8 m. B. LMS least altered carbonate rocks with stylolites, and banded gneiss, cut by vein/dyke of amphibole-plagioclase-titanite that is altered to chlorite and Ti oxides. Diameter of core ~4.5 cm. C. HWS banded biotite–quartz–amphibole–feldspar schist with syn-D2 folding accompanied by sericitisation (and chlorite?). Diameter of core ~4.5 cm. D. Sheared LMS, partly hematite (pink) and chlorite (green) altered, and black chlorite-rich rock. Diameter of core ~4.5 cm. E. Olivine–phyric dolerite dyke with narrow chilled and/or altered margin. Diameter of core ~4.5 cm. F. Photomicrograph of chloritised olivine phenocrysts in dolerite dyke. Plane polarised light.

laths of rutile(?) in clasts of B1 breccia, and coffinite (after uraninite?) replacing Ti oxides also in clasts of B1 breccia. Chloritisation was accompanied by dissolution of quartz, resulting in chloritic breccias with only minor relict quartz. The breccias are heteorolithic with Mg-chloritised clasts of laminated and quartz (Q1)-veined metasedimentary gneiss and schist (some with relict graphite), pegmatite, amphibolite, and amphibole-plagioclase-titanite vein rock.

The timing of B1 brecciation in relation to the local D2 (and regional Shoobridge) event, and to the deposition of the Kombolgie Formation, is unclear. Some clasts display evidence of weak brittle-ductile deformation of the D1 fabrics (e.g., folding of medium metamorphic grade tectonic fabric, and quartz veining along fold hinges). This deformation in the clasts is consistent with the brittle-ductile conditions during the D2 Shoobridge event. However, the chloritic matrix of B1 breccias shows no evidence of a tectonic foliation, as expected if brecciation occurred during D2, and so we favour post-D2 timing of B1 brecciation. Shoobridge event D2 deformation also is distinguished from B1 brecciation by quartz deposition in the former and quartz dissolution in the

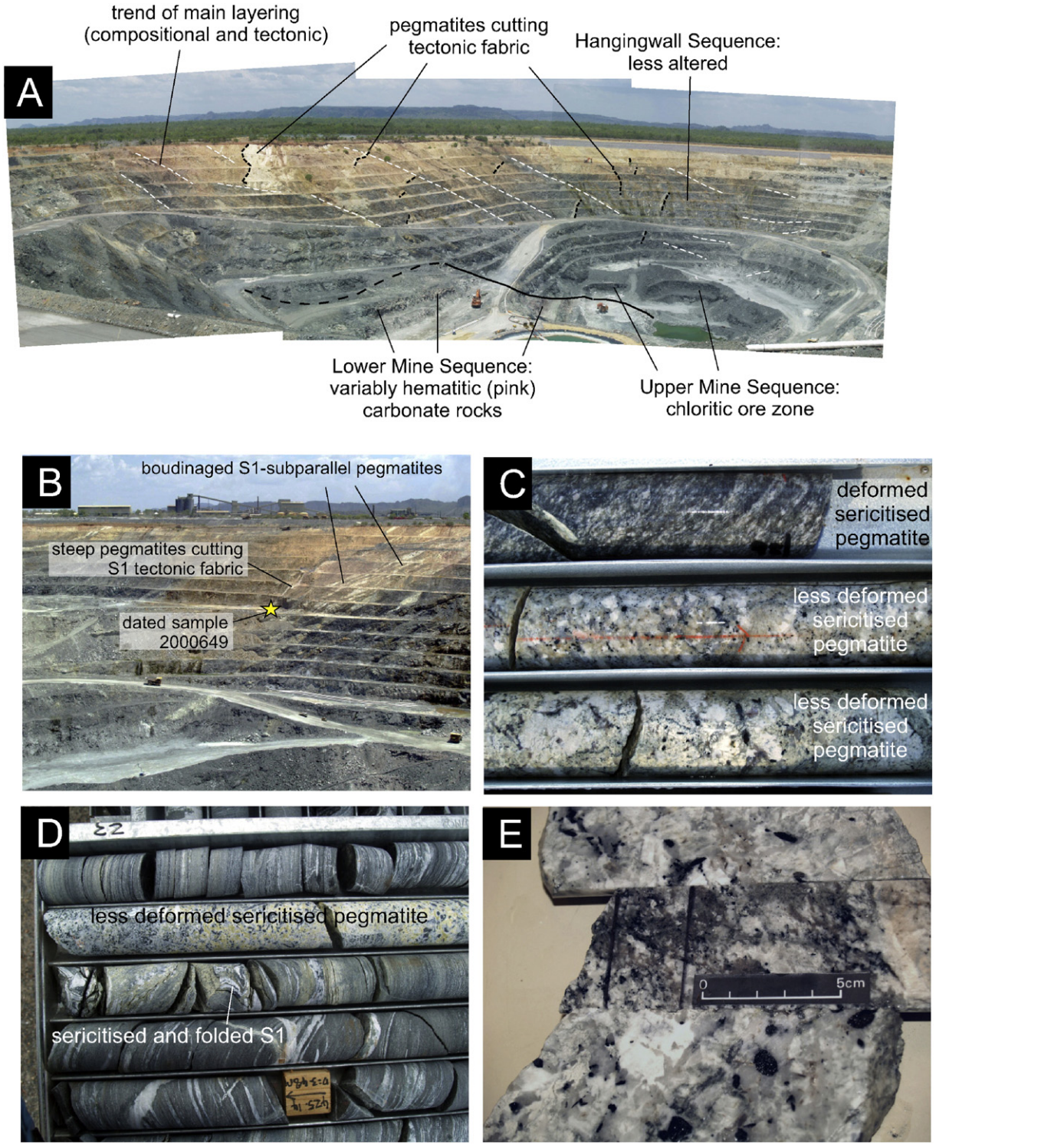

Fig. 8. A. Relative timing of deformation and pegmatite emplacement, Ranger 1 Number 3 orebody. A. Ranger pit, view to the north (on left) and east (on right), illustrating steeply dipping pegmatites cutting the main S1 tectonic fabric. Kombolgie Subgroup outcrops on horizon. B. View to southeast, showing S1-subparallel pegmatites and steeply dipping pegmatites cutting the S1 tectonic fabric. Location shown for dated pegmatite sample from one of the massive, late- to post-D1, pegmatites. C. Sheared, sericitised and chloritised pegmatite and less deformed equivalents within 1–2 m. Core diameter ~ 4.5 cm. D. Less deformed sericitised and chloritised pegmatite cutting strongly sheared and quartz veined schists of the HWS. Note narrow interval with folded S1 tectonic fabric and spatially associated sericitisation (pale greenish yellow zone), interpreted to have developed during the D2 Shoobridge event. Core diameter ~ 4.5 cm. E. Dated pegmatite sample 2000646, drillhole S3PD708 337.6–339.4 m, comprising quartz, K-feldspar, muscovite, tourmaline (black crystals), apatite, zircon (U–Pb dated) and sericite alteration.

latter. Although extensive brecciation of B1 type does not appear to be present within the Kombolgie Subgroup, this unit is locally chloritised (e.g., immediately to the west of the Ranger 1 No. 3 pit; and immediately above the Jabiluka deposit, Polito et al., 2005), and was subjected to reverse faulting at some deposits (e.g., Jabiluka: Polito et al., 2005; Koongarra: Snelling, 1990). Overall, these observations are most consistent with a post-D2, post-Kombolgie origin for the B1 brecciation and associated initial Mg-metasomatism at the Ranger 1 No. 3 orebody.

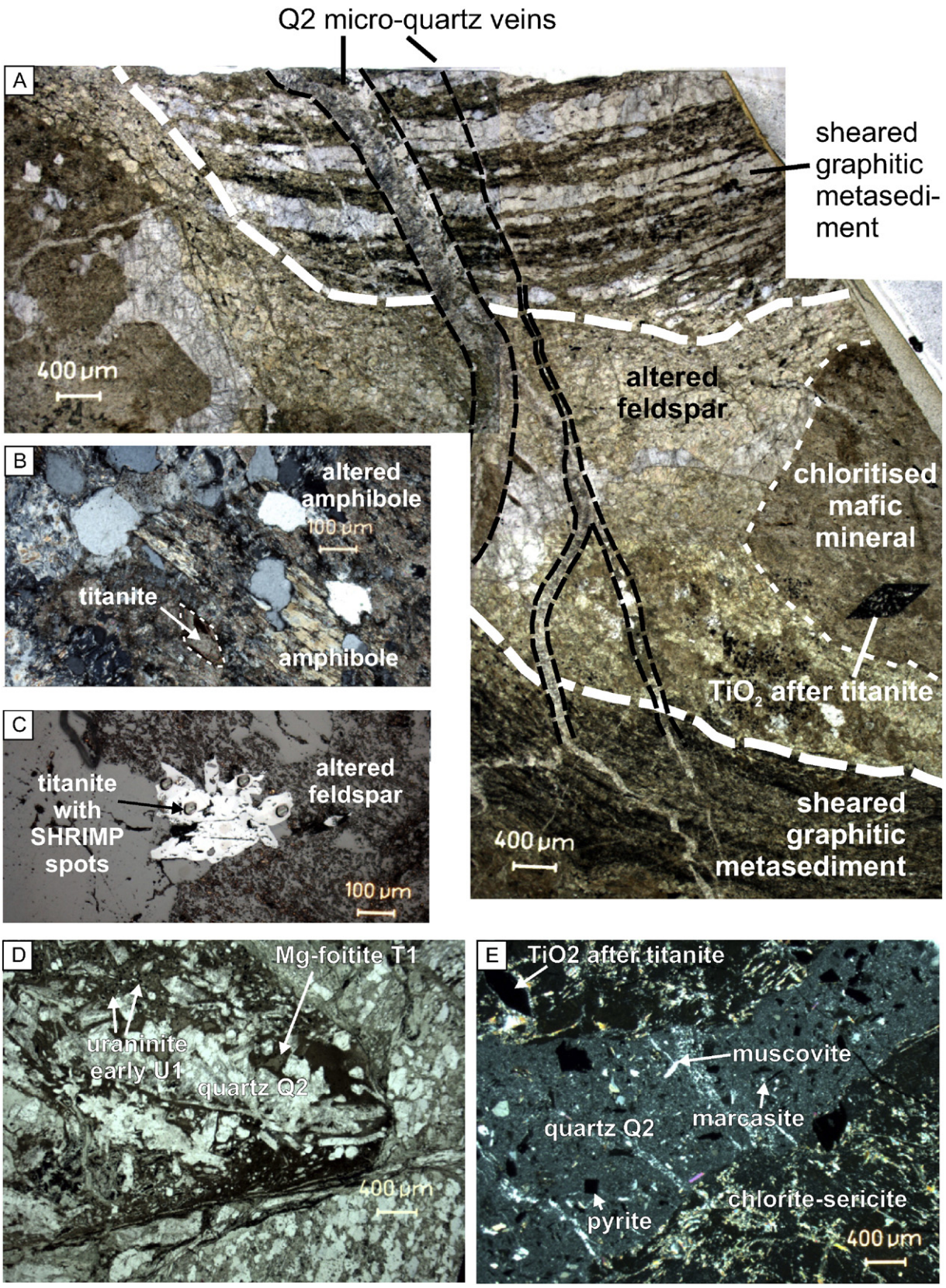

Fig. 9. Microphotographs of titanite-bearing amphibole-plagioclase-apatite veins, and silicification. A. Altered vein with TiO_2 pseudomorphs of titanite, cutting sheared graphitic metasedimentary rock of the HWS, both cut by veinlets of microcrystalline quartz. Transmitted light. B. Vein containing fresh titanite, dated by SHRIMP, and preserved amphibole and plagioclase. Sample from drillhole S3PD730 371.2 m, transmitted light. C. Titanite with SHRIMP dating spots. Sample from drillhole S3PD730 371.2 m, reflected light. D. Clast in breccia containing intergrowths of euhedral quartz Q2, brownish very fine grained tourmaline (Mg-foitite T1), and sparse very fine grained disseminated uraninite U1. Clast is surrounded by comminuted fragments of quartz–chlorite rock. Sample from drillhole S3PD759 395.3 m, transmitted light, plane polarised light. E. Veins of microcrystalline quartz Q2, pyrite, marcasite and fine muscovite cutting massive chlorite–sericite–TiO_2 altered rock (possibly replacing amphibole-plagioclase-titanite veins). Sample from drillhole S3PD730 456.1A m, transmitted light, crossed polars.

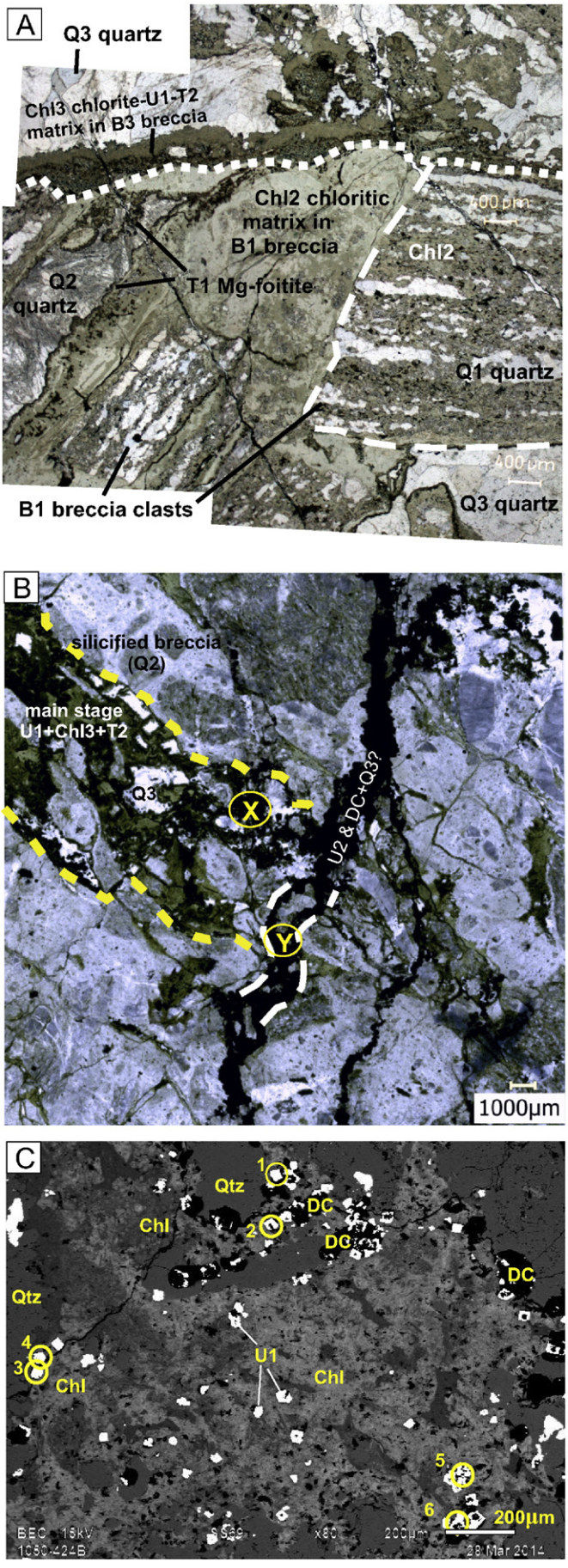

5.6. Pre-ore silicification, and olivine–phyric dolerite

Parts of the LMS and UMS, generally near the contact, were intensely silicified. Careful paragenetic study has shown that this silicification post-dated the B1 breccias and associated Mg-metasomatised rocks but pre-dated the main stage of uranium mineralisation (Fig. 10). This stage of hydrothermal alteration is characterised by vein networks, cavity infills and replacements composed of quartz ± Mg-foitite (tourmaline T1) ± marcasite ± pyrite ± fine muscovite. Rare examples contain very fine-grained uraninite (termed early U1) within the Mg-foitite and quartz assemblage (Fig. 9D). The breccia fabrics of B1 breccias are preserved in some pervasively silicified zones (Fig. 10B). Much of the quartz in this event is microcrystalline (Fig. 9E), whereas other quartz is coarser and euhedral (Fig. 9D) or bladed with radial extinction and numerous fluid inclusions (Fig. 10A), suggesting initial precipitation as chalcedony. The pre-ore silicification cuts previously chloritised amphibole-plagioclase-titanite veins (Fig. 9E) but is cut by the main ore-stage uraninite (Fig. 10A, B).

Some of this silicification has been previously logged as 'chert' in company descriptions of drill holes. Silicification is significant because some of the major uranium ore zones at both Ranger 1 No. 1 and No. 3 orebodies occur above or spatially associated with the 'chert' zones. The 'chert' was interpreted to have replaced carbonate rocks of the LMS (Kendall, 1990; Potma et al., 2012). Our study shows that although the silicification pre-dated the main stage of mineralisation, it partly spatially controlled the location of uranium mineralisation. Recent work by Energy Resources Australia Limited has shown a spatial association in the Ranger 3 Deeps zone between silicification, brecciation, mineralisation, and faults with components of reverse movement in east–west cross sections (Energy Resources Australia, ASX Announcement, November 2014, and Draft Environmental Impact Statement, October 2014, www.energyres.com.au).

Olivine–phyric fine-grained dolerite or basalt occurs as an undeformed thin dyke in drill hole S3PD708 at 504 m depth, where it shows intrusive contacts with banded gneiss host rocks (Fig. 7E). It is pervasively chloritised (Fig. 7F), and fresh olivine is only rarely preserved (Fig. 11D). No silicification of the dyke rock has been observed in this study at the No. 3 orebody. Importantly, clasts of olivine dolerite are also present in breccias in S3PD759 near the contact between the LMS and UMS, where they are overprinted by uraninite mineralisation (Fig. 11A-D). Hence the age of the mafic intrusive rock provides a maximum age constraint on uranium mineralisation.

5.7. Main stage uraninite (U1) mineralisation and alteration

Uranium mineralisation in the Ranger 1 No. 3 orebody is dominantly of very fine grained (10–50 µm diameter) euhedral uraninite (U1) disseminated within chlorite (Chl2) and intergrown with Mg-foitite

Fig. 10. A. microphotograph montage of pre-ore B1 breccia, pre-ore silicification, and main U1 ore stage, sample S3PD759 402.9 m, plane polarised light. B1 breccia is composed of lithic clasts of banded Q1 quartz and chlorite in a matrix of very magnesian Chl2 chlorite (Mg/(Mg + Fe) = ~89–92) and later Mg-Fe chlorite with Mg/(Mg + Fe) = ~77–81 that corrodes quartz. Some voids in B1 breccia were by lined by very fine grained rosettes of tourmaline (Mg-foitite) and filled by Q2 quartz with distinctive bladed texture (after chalcedony?), corresponding to the pre-ore silicification stage. Both the B1 breccia and Q2-T1 assemblages were cut by ore-stage B3 breccia, with infill by Chl3 chlorite, T2 Mg-foitite and U1 urananite. Chl3 with uraninite has variable Mg/(Mg + Fe) between ~92 and 85, overgrown by chlorite without uraninite with Mg/(Mg + Fe) of ~71. Voids in the B3 breccia matrix were filled by Q3 quartz.B. Microphotograph montage of pre-ore silicification (Q2) cut by vein/breccia of main stage U1 uraninite, Chl3 chlorite and T2 Mg-foitite (partly outlined in yellow short-dash line), all cut by late stage vein of U2 uraninite and graphitic disordered carbon (DC) and possibly quartz Q3 (partly outlined in white long-dash line). Silicified domain is either a silicified B1 breccia, or a B2 breccia formed during silicification. The ellipse area labelled 'X' contains uraninite interpreted as U1 dated by Cameca ion probe, and the area containing dated U2 is labelled 'Y'. Sample S3PD1050 424.0 m.C. SEM image of part of area X in Fig. 10B showing uraninite (white, interpreted as U1), grains dated by Cameca ion probe (numbered circles), chlorite (Chl), disordered carbon (DC, black), and quartz (Qtz). Scale bar is 200 µm. Sample S3PD1050 424.0 m.

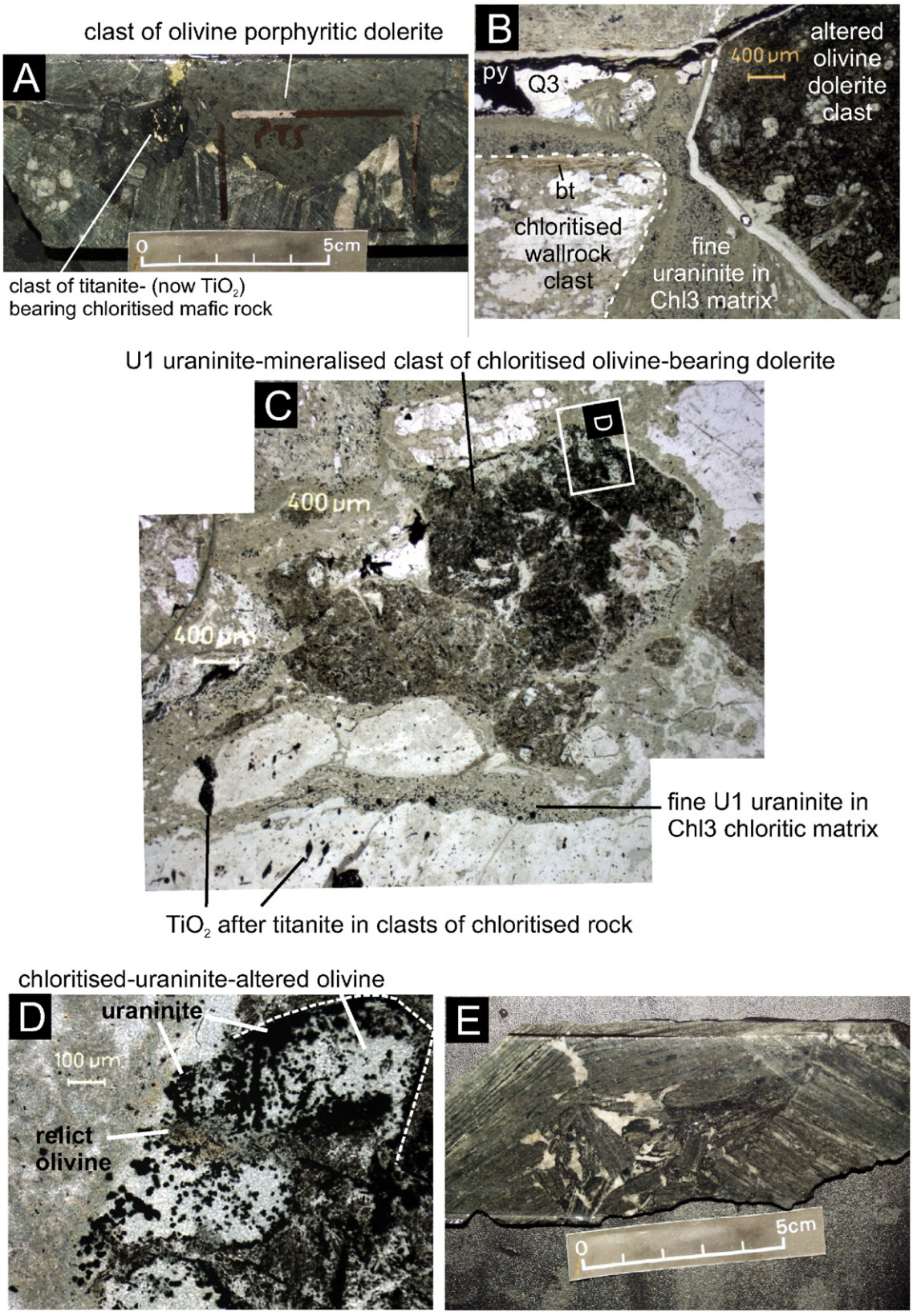

Fig. 11. Olivine–phyric dolerite, B3 breccia, and U1 uraninite mineralisation. A. Main ore stage (B3) heterolithic breccia with clasts of chloritised and uraninite-mineralised olivine–phyric dolerite, chloritised mafic rock with titanite (cream spots, now TiO_2), and banded schist (now chlorite-quartz). Sample S3PD759 434.0 m. B. Microphotograph of B3 breccia in (A), showing chlorite- and uraninite-bearing olivine–phyric dolerite clast in a matrix of Chl3 and fine grained disseminated uraninite. Relict biotite (bt) in chloritised banded schist wallrock clast, and late-stage fill of voids in matrix by Q3 quartz and pyrite (py). C. Microphotograph of B3 breccia with chlorite- and uraninite-bearing olivine–phyric dolerite clast, ex-titanite-bearing altered mafic rock, and other clasts in a matrix of Chl3 and fine grained disseminated uraninite. D. Inset area in (C) showing relict olivine and chloritised olivine with uraninite in clast of dolerite. E. Typical mineralised breccia from Ranger 3 Deeps zone, with clasts of banded schist (some mylonitic; altered to chlorite–quartz) in a matrix of Chl3 chlorite and uraninite (dark grey-green), and late-stage Q3 quartz infill of voids in the breccia matrix.

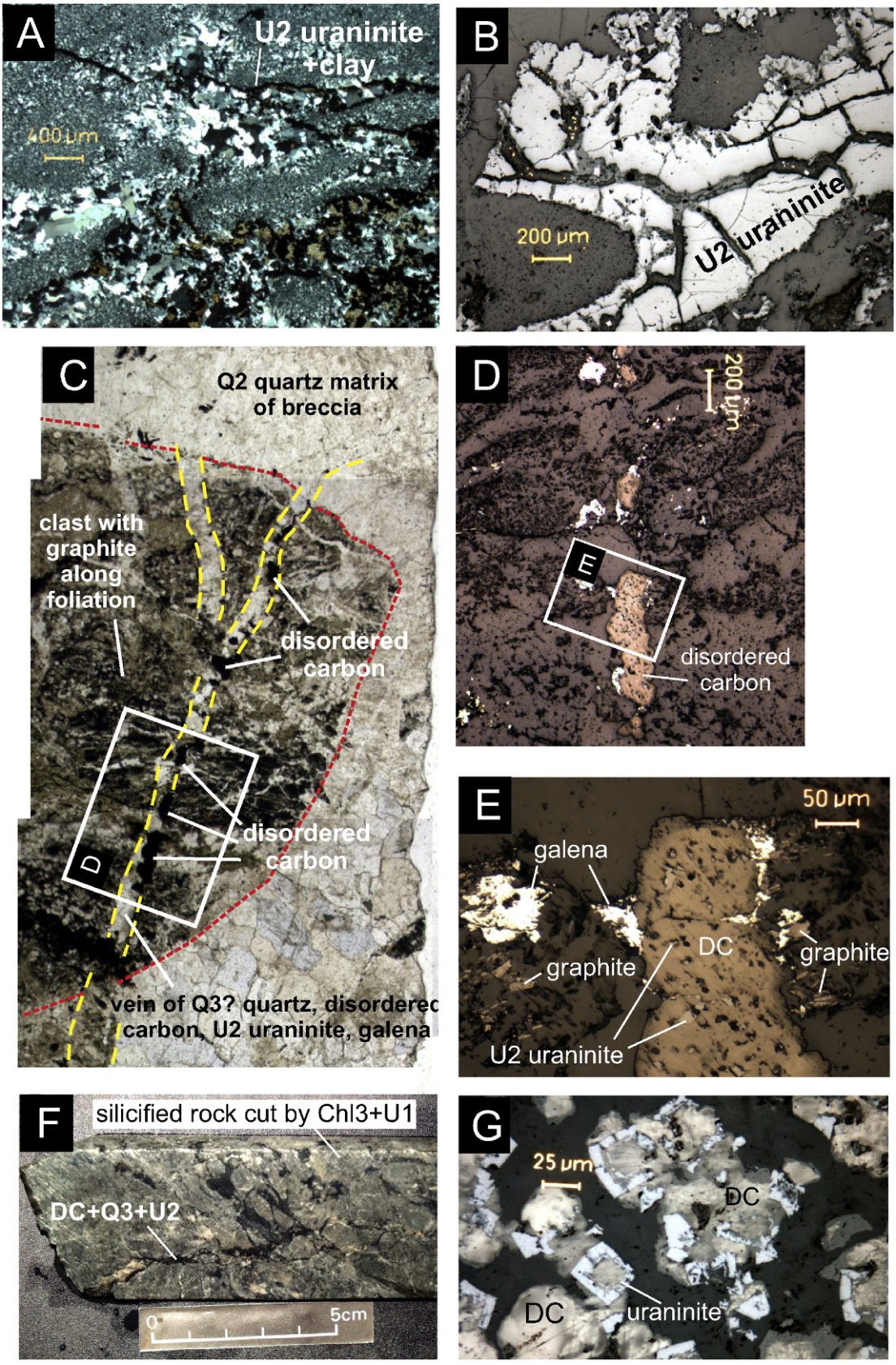

Fig. 12. Microphotographs and drill core image of late-stage uraninite and disordered carbon. A. Veinlets of massive uraninite U3 and yellowish clay cutting silicified rock ('chert'). Cross polarised light, sample S3PD730 459.7 m. B. Massive uraninite U3 veinlet, dated by ion microprobe. Reflected light, sample S3PD730 459.7 m. C. Photomontage of silicified rock breccia (Q2 quartz matrix) with clasts of graphite-bearing schist, cut by veins of quartz (Q3?), disordered carbon and uraninite U2. D. Inset area shown in (C) with disordered carbon, galena (white) and quartz in veinlet. Reflected light, sample S3PD730 457.4 m. E. Detail of inset in (D) showing very fine disseminated uraninite U2 within disordered carbon, and galena, adjacent to aligned metamorphic graphite in host rock. Reflected light, sample S3PD730 457.4 m. F. Drill core of silicified rock cut by vein network of chlorite Chl3 and uraninite U1, cut by veins of disordered carbon, uraninite U2 and quartz Q3. Figs. 10B and 10C from same sample, S3PD1050 424.0 m. G. Disordered carbon (DC) intergrown with atoll-textured uraninite (U2) from DC + U2 + Q3 vein shown in Fig. 12 G and 10B. Reflected light, sample S3PD1050 424.0 m.

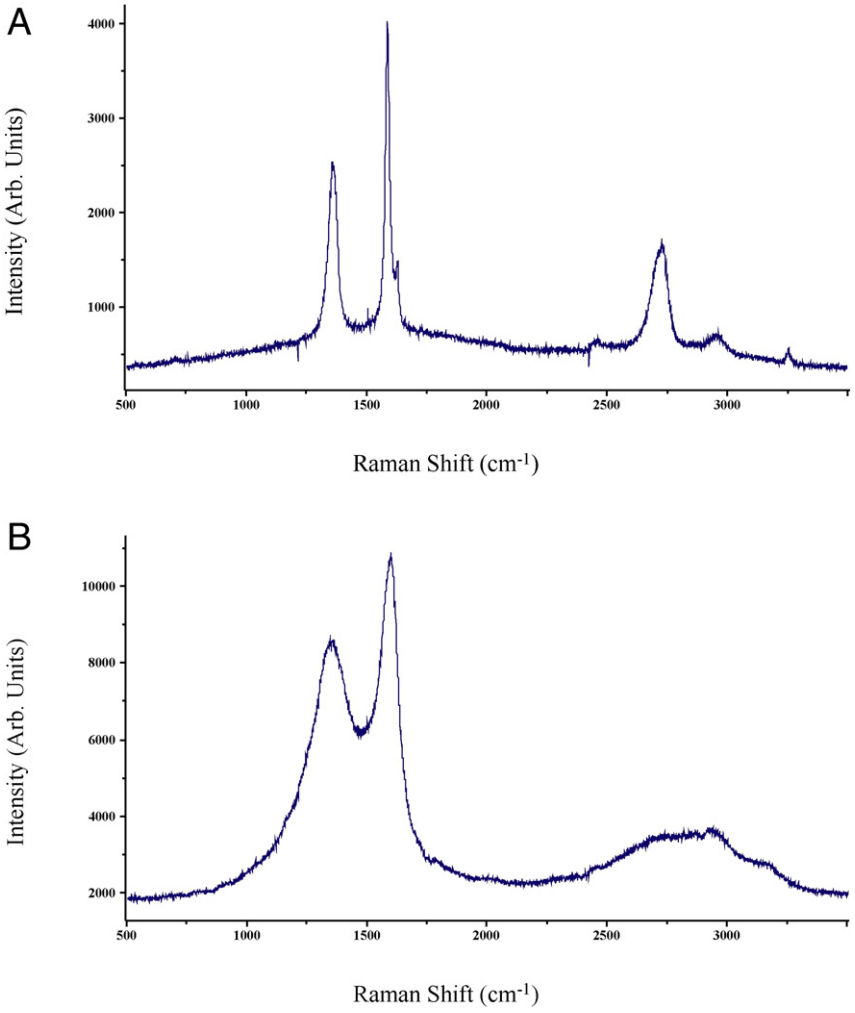

Fig. 13. A. Representative laser Raman spectrum of fine graphite laths of interpreted metamorphic origin, aligned within the S1 tectonic fabric within schist. Sample S3PD759 395.2 m. B. Representative laser Raman spectrum of veins and disseminated patches of disordered carbon. Sample S3PD759 334.5 m.

(tourmaline T2) that overprints the pre-ore B1 and B2 breccias (Fig. 10A, B). Uraninite U1 commonly exhibits 'atoll' texture where the cores of the grains are occupied by chlorite, brown oxide minerals, or rarely by disordered graphitic carbon (Fig. 10C). Almost all of the U1 uraninite contains minute inclusions of galena of presumed radiogenic origin. Very fine grained pyrite and traces of chalcopyrite are present with the uraninite U1 and chlorite Chl2, and are interpreted to have precipitated synchronously with main-stage uranium mineralisation.

Most of this style of mineralisation is confined to the UMS, but examples occur in the upper parts of the LMS where the U1 assemblage cross-cuts previously silicified breccias (B1/B2; Fig. 10B). Although uraninite U1 and chlorite Chl2 occur as infill of re-activated B1 and B2 breccias and as veins, it is evident that new breccias (B3) also developed at this stage. Such B3 breccias have matrix composed entirely of chlorite Chl3, uraninite U1 and co-genetic minerals including fine grained Mg-foitite which imparts a brown colouration in this type of B3 matrix (Fig. 11A, E). As noted above, this mineralisation assemblage overprints olivine–phyric dolerite clasts in B3 breccias (Fig. 11B, C, 11D). The structural setting and kinematics of deformation during B3 breccia formation were not investigated in detail in this study. Energy Resources Australia cross sections of the Ranger 3 Deeps zone show a complex network of steep-east dipping reverse faults and shallow-east-dipping faults, with some of the higher grade uranium zones associated spatially with these faults (Energy Resources Australia, 2014: www.energyres.com.au, Draft Environmental Impact Statement).

Although the main phase of uraninite mineralisation post-dates the development of B1 breccias and initial Mg-metasomatism in the Ranger 1 No. 3 orebody, it is evident from the spatial coincidence of B1 breccias and uranium mineralisation that the B1 breccias were crucial in controlling the location of uranium mineralisation. We also do not rule out the presence of syn-B1 uranium mineralisation elsewhere within the hydrothermal system, which has not yet been identified.

Uraninite U1 and chlorite Chl2 in the matrix of B3 breccias is disrupted in places by a final phase of quartz infilling of voids, termed quartz Q3.

5.8. Second-stage uraninite U2 with disordered carbon

A second stage of uraninite mineralisation has been identified in this study, represented by veinlets of distinctive disordered graphitic carbon with inclusions of fine-grained U2 uraninite (Figs. 10B, C, 12A-E). Quartz is present in some veins (possibly Q3; Fig. 12A, C), making this assemblage very different to the earlier U1-chlorite stage. Laser Raman spectra show the disordered carbon to have distinctly broader peaks than metamorphic graphite in the same samples (Fig. 13). This carbon forms veins up to 1 mm wide and rounded masses up to 0.5 mm diameter (Figs. 10B, 12F). In detail the disordered carbon commonly rims the uraninite U2 grains or occupies the cores of 'atoll' textured uraninite euhedra (Figs. 10C, 12G). Although this type of uranium mineralisation is volumetrically small in the three drill holes studied in detail, four samples

across all three holes contained the late-stage disordered carbon-uraninite assemblage. In three of the four samples it occurs within previously silicified rocks, close to the LMS/UMS contact or within the UMS (Fig. 12F). Sample S3PD730 457.4 contains clusters of disordered carbon with uraninite U2 inclusions that appear to have nucleated where the vein traverses bands of metamorphic graphite in an unmineralised clast within B2 silicified breccia (Fig. 12C, D, E).

5.9. Late-stage uraninite U3 veins

The final stage of uranium mineralisation is represented by veinlets of massive uraninite U3 up to a few millimetres wide; only a few examples of this style of mineralisation were observed in the drill holes studied, hosted by silicified rock (Fig. 12A, B). This uraninite lacks the submicron sized inclusions of galena that characterise most U1 and U2 uraninite. Although cross-cutting relationships with U1 and U2 were not observed, geochronology results (see below) strongly support the proposal of post-U1 and post-U2 timing.

5.10. Post-uraninite alteration

A late stage of fracturing, veining and infilling is characterised by veinlets of yellow clay and fine-grained chalcopyrite cutting, although apparently spatially associated with, the U3 uraninite (Fig. 12B). The timing of coffinite has not been constrained but may have replaced U1 uraninite. Voids within the late-stage quartz Q3 are filled by chalcopyrite and carbonate.

6. Whole-rock geochemistry

Whole-rock geochemical analyses were acquired for (a) 14 samples from drill hole S3PD730 intersecting the Ranger 3 Deeps zone, to examine metasomatic effects associated with uranium mineralisation, and (b) one sample of olivine–phyric dolerite from drill hole S3PD708 to test whether this rock is compositionally similar to the Oenpelli Dolerite or other mafic rocks in the region. The analyses were carried out at Geoscience Australia by XRF for major elements and ICPMS for trace elements (Table 3; method described in Appendix A). The uppermost four samples from S3PD730 (at depths of 306 m, 339 m, 352 m, 370 m) represent least altered Hangingwall Sequence quartzo-felspathic schist containing metamorphic biotite and amphibole and are only very weakly chloritised and/or sericitised. Sample 376.2 m is from a zone containing abundant sericite and chlorite alteration and hydrothermal monazite with a U–Pb age of 1800 ± 9 Ma (Mercadier et al., 2013b). The next four samples (381 m, 391 m, 400 m, 457.8 m) represent very strongly sheared schist of the Hangingwall Sequence and Upper Mine Sequence in which the intensity of chloritisation generally increases with depth, whereas sericitisation generally decreases with depth.

Elemental gains and losses were investigated using the method of Grant (1986). Compared with least altered schists of the Hangingwall Sequence a strongly chloritised and weakly mineralised graphitic schist with 181 ppm U (sample 2167042, Table 3) experienced large gains in Mg, S, As, Mo, Ni, Co, V, Pb, Cu and Cl, and lesser gains in total Fe and Cr (Fig. 14A). The Fe_2O_3/FeO ratio also increased dramatically in this mineralised interval, reflecting oxidation during metasomatism despite the presence of abundant new pyrite and relict metamorphic graphite. The strongly chloritised schist recorded very extensive losses of Na, Ca, Ba, Sr, REE, Y, K and Rb. The light REE (La, Ce, Pr, Nd) show greater relative losses than the middle and heavy REE (Sm, Tb, Dy, Ho, Er, Yb, Lu; Fig. 14A). The depletion of Si during chloritisation is noteworthy as it implies that reacted fluids would have contained higher Si as well as Na–Ca–K–LREE during chloritisation reactions. Similar gains and losses occurred during chloritisation of pegmatite in the LMS, with the important exception of the REE. The light REE were evidently enriched along with U, Mg, Ni, V, Mo and Co whereas the middle and heavy REE were mostly immobile (Fig. 14B). These results for drill hole S3PD730 largely confirm the broader patterns of metasomatism reported by Fisher et al. (2013) for alteration at the Ranger 1 No. 3 orebody. In particular, the light REE are strongly depleted in the most intensely Mg-metasomatised and mineralised zones whereas the heavy REE are un-depleted or less depleted in this zone relative to least altered Hangingwall Sequence rocks (Fisher et al., 2013). This spatial pattern is consistent with the lack of observed monazite or other light REE-bearing minerals in strongly chloritised and U mineralised rocks and also with the preservation of pre-ore monazite in outer alteration zones (Fisher et al., 2013; Mercadier et al., 2013b).

A sample of chloritised and mineralised olivine–phyric dolerite (2944 ppm U, sample 2169196, Table 3) is compositionally within or close to the ranges of the Oenpelli Dolerite and Nungbalgarri Volcanics on plots utilising elements that appear to be relatively immobile during chloritisation (Fig. 15). The dolerite at the Nabarlek deposit with a U–Pb baddeleyite age of 1723 ± 6 Ma, referred to as Oenpelli Dolerite (Page, 1996b), also plots within these compositional ranges (sample 1463499, Table 3; Fig. 15). Overall, these data are consistent with the proposal that the olivine–phyric dolerite at Ranger is either a part of the Oenpelli Dolerite or is a feeder to the Nungbalgarri Volcanics. In the latter case, if the Nungbalgarri Volcanics are correlated with the 1780–1760 Ma Siegel Volcanics (Scott et al., 2000; Polito et al., 2011) then the maximum age of uranium mineralisation would be ~1780 Ma. In the former case, the maximum age of mineralisation would be ~1723 Ma.

7. Geochronology samples and results — Ranger 1 number 3 orebody

Methods of analysis are presented in the Appendix A. Results of SHRIMP[1] and Cameca ion microprobe U–Pb and EPMA chemical dating are summarised in Table 4.

7.1. Zircon U–Pb ion microprobe dating — samples and results, pegmatites

7.1.1. Samples

Zircon mineral separations were attempted on four samples of strongly foliated and unfoliated to weakly foliated pegmatites, with two yielding sufficient zircons for geochronology. Sample 2000649 is from a steeply dipping unfoliated pegmatite on the south wall of the Ranger 1 Number 3 orebody pit which cuts the main shallow-dipping tectonic foliation and subparallel lithological layering in the metasedimentary host rock (Fig. 8B). Sample 2000646 is a massive to weakly foliated pegmatite from the Ranger 3 Deeps zone (Table 4; Fig. 8E). Both samples comprise igneous quartz, K-feldspar, sodic plagioclase, tourmaline, muscovite and zircon. Feldspars are partly altered to very fine grained randomly oriented white mica. Muscovite in sample 2000646 is weakly aligned, K-feldspar is fractured, and coarse igneous quartz is recrystallised to finer grained mosaics in both samples, indicating that both pegmatites were deformed. Samples of the strongly deformed and intensely chloritised and sericitised pegmatites were not dated due to lack of zircons.

Zircons from samples 2000646 and 2000649 are generally prismatic with cathodoluminescence (CL) images recording oscillatory zoning in many grains. The CL imaging also shows thin bright overgrowths on most grains, which were too narrow to be analysed by SHRIMP.

7.1.2. Results

Fourty-nine analyses were completed on sample 2000646 which are presented in Appendix Table 1 and Fig. 16A. Uranium concentrations range from 46 ppm to 1172 ppm and Th/U ratios range from 0.38 to 1.04. Twenty-four analyses with >1% common lead or >5% discordancy were excluded from further consideration, and the remaining 25 analyses yielded an age of 1867.0 ± 3.5 Ma (2σ). This is interpreted to represent the magmatic crystallisation age of the weakly foliated pegmatite from the Ranger 3 Deeps zone.

[1] Sensitive High-Resolution Ion Microprobe

Table 3
Whole-rock geochemistry, Ranger 1 No. 3 orebody and Oenpelli Dolerite. Lithology detailed below table. See Appendix A for analytical method.

Drill hole	S3PD730	S3PD730	S3PD730	S3PD730	S3PD730	S3PD730	S3PD730	S3PD730	S3PD730	S3PD730	S3PD730	S3PD730	S3PD730	S3PD730	S3PD708	DDH98
Depth, m	306	339	352	370	376.2	381	391	400	457.8	547.6	569	611.8	646.4	647	504	46–47
Sample No	2167035	2167036	2167037	2169197	2167038	2167039	2167040	2167041	2167042	2167043	2167044	2167045	2167046	2167047	2169196	1463499
Unit	HWS	HWS	HWS	HWS	HWS	UMS	UMS	UMS	UMS	LMS	LMS	LMS	LMS	LMS		Oenpelli
Lithology	schist	schist	schist	schist	schist	schist	schist	schist	schist	carbonate	carbonate	gneiss	pegmatite	pegmatite	dolerite	dolerite
SiO_2 wt %	65.44	64.74	64.34	66.9	65.59	66.05	64.01	65.52	46.79	7.84	11.34	59.33	69.16	79.04	47.04	55.12
TiO_2	0.53	0.57	0.57	0.52	0.54	0.53	0.52	0.54	0.64	0.05	0.08	0.87	0.02	0.01	1.27	2.11
Al_2O_3	15.52	16.18	16.09	15.25	15.72	15.48	15.28	15.45	14.45	1.18	2.13	19.23	13.48	12.01	16.96	11.46
Fe_2O_3 tot	4.64	5.15	5.11	4.73	3.81	4.36	5.4	4.39	9.18	0.81	1.45	3.3	2.48	0.99	3.82	14.62
Fe_2O_3 calc	0.59	0.63	0.91	0.63	0.54	0.48	0.48	0.57	4.69	0.04	0.26	1.18	0.76	0.28	0.98	2.54
FeO	3.64	4.07	3.78	3.69	2.95	3.49	4.43	3.44	4.04	0.69	1.07	1.91	1.54	0.65	2.56	10.87
MnO	0.05	0.09	0.09	0.06	0.05	0.05	0.09	0.07	0.03	0.04	0.04	0.01	0.02	0.02	0.02	0.15
MgO	2.42	2.52	2.52	2.41	4.01	3.91	4.46	5.16	10.93	22.78	20.3	7.73	8.46	2.28	14.22	2.24
CaO	3.85	3.45	3.43	2.78	1.94	1.1	1.15	1.08	0.22	30.72	25.28	0.41	0.39	0.35	1.47	8.43
Na_2O	2.89	2.52	2.51	2.67	0.14	1.52	0.79	0.13	0.13	0.09	0.05	0.25	0.17	0.14	0.17	2.82
K_2O	3.75	4.48	4.46	3.88	3.93	5.03	5	3.99	1.37	0.02	0.17	3.97	0.83	2.9	0.34	0.99
P_2O_5	0.12	0.12	0.12	0.12	0.12	0.12	0.11	0.12	0.12	0.1	0.11	0.05	0.2	0.21	0.99	0.48
REST	0.24	0.26	0.25	0.24	0.14	0.23	0.23	0.15	0.2	0.04	0.05	0.17	0.08	0.05	0.89	0.2
MLOI	1.92	1.15	1.78	1.74	5.45	2.67	3.78	4.6	11.99	38.84	38.05	5.5	5.61	2.76	9.76	2.74
S	0.008	0.02	0.02	0.056	0.016	0.02	0.008	0.008	3.092	0.012		0.056	0.008	0.008	0.06	
O = S		0.01	0.01	0.03	0.01	0.01			1.55	0.01		0.03	0.00	0.00	0.03	
Total	100.97	100.79	100.86	100.92	101.13	100.67	100.34	100.83	97.15	102.44	98.93	100.64	100.72	100.70	96.70	100.15
As* ppm	2	1	<1	<1	11	2	<1	1	25	3	3	1	3	<1	59	1.5
Ba	821	983	954	848	90.1	1012	1034	201	60.1	2.13	11.2	307	11.1	38.2	61.2	135
Be	2.58	2.58	2.53	2.26	3.92	2.89	2.94	4.83	4.44	1.03	1.08	3.54	8.29	7.56	6.57	1
Bi	0.097	0.041	0.06	0.086	0.174	0.068	0.064	0.16	5.2	0.021	<0.02	0.114	0.874	1.15	0.647	<2
Ce	89.8	96.6	93.5	88.7	108	84.9	94.1	78	2.18	4.65	9.81	9.68	3.55	0.732	65.2	84
Cl*	<100	<100	<100	104	<100	<100	<100	125	208	207	203	<100	328	<100	323	
Co*	12	12	12	11	8	13	13	9	46	4	4	15	13	3	23	47
Cr*	74	77	80	77	72	80	74	76	152	13	23	185	19	29	1098	177
Cs	3.91	5.63	5.27	3.98	8.41	6.68	5.6	9.48	3.62	0.103	0.501	3.78	7.85	12.8	3.43	<6
Cu*	6	6	6	7	7	8	6	8	18	6	4	6	4	4	60	66
Dy	4.34	4.7	4.62	4.41	4.33	3.92	4.82	3.92	1.43	0.556	0.731	2.1	0.58	0.281	15	
Er	2.4	2.6	2.64	2.45	2.15	2.13	2.63	2.23	0.914	0.274	0.389	1.24	0.149	0.081	6.9	
Eu	1.2	1.28	1.27	1.21	1.38	0.911	1.19	1.02	0.097	0.103	0.162	0.265	0.074	0.028	3.11	
F*	475	582	469	556	627	532	518	866	<100	<100	<100	410	209	258	493	
Ga	17.2	19.7	19.2	18.6	19.3	17.8	17.4	17.7	34.9	1.43	2.81	38.1	25.2	22	66.7	28
Gd	4.92	5.12	5.18	4.94	5.74	4.25	5.17	4.18	0.588	0.423	0.669	1.21	0.493	0.155	11.1	
Ge	1.41	1.78	1.54	1.5	1.07	1.41	1.07	1.17	1.54	0.217	0.227	2.71	2.58	2.79	1.48	2.5
Hf	5.8	5.99	5.99	5.51	6.04	6.15	5.62	5.73	3.5	0.269	0.647	4.42	0.204	0.15	13.7	9
Ho	0.876	0.937	0.96	0.912	0.814	0.779	1.01	0.868	0.308	0.097	0.126	0.44	0.075	0.026	2.86	
La	48.8	52.5	51.4	49.2	62	45.4	52.5	41.7	1.02	2.68	5.57	5.47	3.45	0.448	27.6	40
Lu	0.321	0.364	0.346	0.338	0.334	0.328	0.372	0.293	0.137	0.03	0.05	0.193	0.017	0.011	0.746	
Mo	1.75	1.94	1.56	2.04	0.928	1.18	1.14	1.04	7.89	0.569	<0.3	0.557	1.41	1.35	3.43	3

Nb	10.4	11.6	11.5	10.3	10.9	10.7	9.87	10.9	11.4	0.772	1.7	18.6	8.85	15.3	18.6	25
Nd	35.5	38.2	37.4	35.5	42.8	33.8	36.6	31.2	1.21	2.38	4.4	4.23	1.34	0.41	37	51
Ni*	10	12	12	11	10	10	12	11	145	3	2	68	55	1	215	57
Pb	19.6	19.6	19.2	14.2	4.28	11.7	10.4	3.61	65.6	1.42	0.888	41	8.33	2.47	291	10
Pr	9.86	10.6	10.4	9.9	12.1	9.51	10.4	8.78	0.27	0.626	1.19	1.26	0.374	0.102	8.79	9
Rb	136	168	168	134	266	157	175	163	81	1.08	7.13	108	82.9	196	16.7	13
Sb	<0.8	<0.8	<0.8	<0.8	1.39	<0.8	<0.8	<0.8	1.26	<0.8	<0.8	<0.8	0.826	<0.8	<0.8	
Sc*	12	13	13	14	14	14	13	12	17	11	13	16	2	<1	42	30
Sm	6.2	6.61	6.89	6.28	7.13	5.62	6.31	5.43	−0.5	−0.5	0.767	0.928	−0.5	−0.5	9.32	
Sn	2.38	2.35	2.64	1.44	3.22	2.49	2.33	1.95	3.4	0.241	0.285	3.73	6.58	11.2	3.56	4
Sr	325	300	298	294	16.1	167	111	26.4	7.97	55.3	48.2	12.6	7.59	5.44	53	93
Ta	0.927	0.983	0.961	0.865	0.941	0.953	0.847	0.935	0.997	−0.05	0.108	1.64	1.95	1.94	0.921	−2
Tb	0.745	0.836	0.827	0.736	0.792	0.632	0.809	0.675	0.154	0.062	0.102	0.262	0.079	0.025	2.31	
Th	17.6	20.5	20	19.7	22.3	21.3	19.1	17	11.3	1.19	2.63	13.6	0.152	0.124	21.7	5
U	3.84	4	3.89	3.85	3.82	3.93	3.67	3.72	181	1.75	1.02	152	36.2	1.3	2944	3
V*	51	56	57	53	55	54	51	54	205	5	8	120	12	1	392	110
W	<0.5	0.531	<0.5	<0.5	1.18	0.519	0.537	0.652	3.94	<0.5	<0.5	3.75	1.28	1.88	31.2	
Y	24.6	28.2	27.1	27.4	25.7	22.2	27.6	21.7	7.07	4.85	5.34	11	1.71	1.03	73.9	58
Yb	2.2	2.5	2.56	2.38	2.16	2.2	2.47	2.04	0.996	0.204	0.351	1.41	0.156	0.09	5.76	
Zn*	49	58	45	39	14	31	55	27	61	11	17	37	40	27	53	91
Zr	193	203	199	189	203	205	188	199	118	8.72	20.5	152	3.02	1.5	504	295

Sample number	Depth (m), S3PD730	Description
2167035	306	Less altered biotite–amphibole bearing schist
2167036	339	Least altered biotite–amphibole bearing schist
2167037	352	Less altered biotite–amphibole bearing schist; rare chlorite alteration, weak sericite alteration
2169197	370	Least altered biotite–amphibole bearing schist
2167038	376.2	Sericitised biotite schist, with quartz veining
2167039	381	Very strongly sheared (mylonitised) banded schist, 10% chloritisation of biotite, 90% sericite alteration of plagioclase, no amphibole
2167040	391	Very strongly sheared (mylonitised) schist with 50% chloritisation of biotite, 80–90% sericitisation of plag; all amphibole is chloritised
2167041	400	Strongly sheared (almost mylonite) schist, 30% chloritisation of biotite, 90% sericitisation of plag, no amphibole
2167042	457.8	Strongly sheared (tending to mylonitic) C-rich (graphitic) and sulfide-rich (mainly pyrite) schist. All biotite, plag and amphibole altered to chlorite and sericite
2167043	547.6	Massive grey carbonate; weak sericitization
2167044	569	Massive carbonate; weak chlorite alteration ± sericite
2167045	611.8	Banded garnet schist within LMS or Nanambu Complex
2167046	646.4	Pegmatite; intensely chloritised with relict muscovite, quartz, tourmaline
2167047	647	Sericitised pegmatite
2169196		Olivine–phyric fine-grained dolerite dyke, massive, chloritised
1463499		Oenpelli Dolerite, Nabarlek deposit, drillhole DDH98, depth 46–47 m (same sample with dated baddeleyite), from latitude −12.306579 longitude 133.322072 (Page, 1996b)

All major elements analysed by XRF.
*Analysed by XRF; all other trace elements analysed by ICPMS.
FeO analysed by titration.
Sample 2167042 (with low total) contains several percent graphite and pyrite.

Table 4
Summary of geochronology results, Ranger 1 Number 3 orebody.

Location/drillhole	Depth (m), sample	Lithology	Mineral	Method	Age, Ma	Interpretation
S3PD708	337.6–339.4, 2000646	Pegmatite	Zircon	SHRIMP U–Pb	1867.0 ± 3.5[a]	Igneous crystallisation
Ranger pit	2000649	Pegmatite	Zircon	SHRIMP U–Pb	1862.8 ± 3.4[a]	Igneous crystallisation
S3PD730	371.2	Mafic vein	Titanite	SHRIMP U–Pb	1845.4 ± 4.2[a]	Hydrothermal or magmatic age
S3PD730	376.9	Schist, HWS	Monazite	SHRIMP U–Pb	1800 ± 9[b]	Hydrothermal/retrograde metamorphic age
S3PD759	408.8	ore breccia, UMS	Uraninite U1	Cameca U–Pb	1688 ± 46[c]	U1 uraninite formation age
S3PD1050	424.0	Ore breccia, LMS	Uraninite U1 + U2	Cameca U–Pb	1421 ± 68[c]	Age of U2? Reset age of U1?
S3PD730	459.6–459.7	Veins in LMS	Uraninite U3	Cameca U–Pb	474 ± 6[c]	U3 uraninite formation age
S3PD759	408.8	Ore breccia, UMS	Uraninite U1	EPMA	1646 oldest; 1443 yougest	Reset/disturbed hydrothermal ages
S3PD1050	424.0	Ore breccia, LMS	Uraninite U1 + U2	EPMA	842 oldest; 612 youngest	Not geologically meaningful; lead loss
S3PD730	459.6–459.7	Veins in LMS	Uraninite U3	EPMA	515 oldest 385 youngest	Late-stage uranium ore formation

HWS = Hangingwall Schist.
UMS = Upper Mine Sequence.
LMS = Lower Mine Sequence.
EPMA = electron microprobe analysis.
[a] Weighted mean ^{207}Pb–^{206}Pb age.
[b] $^{206}Pb/^{238}U$–$^{207}Pb/^{235}U$ upper intercept age.
[c] Mercadier et al. (2013b).

The results for fourty-five analyses of zircons in sample 2000649 are presented in Appendix Table 2 and Fig. 16B. Uranium concentrations range from 118 ppm to 495 ppm (an outlier has 3748 ppm U), and Th/U ratios range from 0.25 to 1.12. Fourteen analyses with >1% common lead or >5% discordancy were excluded from further consideration, and the remaining 31 analyses yielded an age of 1862.8 ± 3.4 Ma (2σ). This is interpreted to represent the magmatic crystallisation age of the massive pegmatite from the Ranger pit.

7.2. Titanite U–Pb ion microprobe dating — samples and results, titanite–amphibole–plagioclase veins

7.2.1. Samples

Fresh titanite is very rare in the samples studied and is generally replaced by TiO_2 minerals, as noted above. Drill hole sample S3PD730 371.2 m contains a thin vein of amphibole–plagioclase–titanite–apatite hosted by quartz–feldspar–biotite banded schist (Fig. 9B, C). Disseminated titanite is euhedral and shows no evidence of alteration by TiO_2 minerals.

7.2.2. Results

Twenty spots were analysed across 6 different titanite grains in the thin section, covering all the variations in colour and other characteristics observed in the SEM and microphotography (Appendix Table 3). Excluding the three highly discordant data — shown in Fig. 17 as light grey error ellipses — the remaining spots cluster below concordia with variable discordance (2–13%), giving a weighted mean $^{207}Pb/^{206}Pb$ age of 1845.4 ± 4.2 Ma. Inclusion of all the data yields an upper intercept age of 1848.4 ± 5.4 Ma, with apparently recent Pb-loss dominant.

7.3. Uraninite U–Pb ion microprobe dating — samples and results

7.3.1. Samples

Sample S3PD759 408.0 m is representative of the main breccia-hosted U1 uraninite mineralisation, and contains fine-grained uraninite euhedra, some of which have cores replaced by unidentified minerals. Although most U1 uraninite euhedra contain extremely fine inclusions of galena, a few are almost inclusion-free.

Sample S3PD1050 424.0 m contains both uraninite U1 and U2. Silicified breccias corresponding to the pre-ore silicification stage are cross-cut by B2 stage breccia veins containing fine-grained uraninite U1 euhedra within the chloritic matrix of the breccia veins. The U1 uraninite commonly contains extremely fine-grained inclusions of galena. Both the silicified breccia and B2 breccia veins are cut by veins of disordered carbon which encloses very fine-grained euhedra of disseminated uraninite U2. Many of the U2 as well as some U1 grains have cores occupied by disordered carbon but the relative timing relationships are cryptic (e.g., Fig. 12B).

Samples S3PD730 459.6 m and 459.7 m are representative of the late-stage veins of massive uraninite U3, and comprise 1–3 mm wide veins and veinlet networks of uraninite cutting silicified breccia. Fine-grained galena inclusions are not present within this U3 uraninite but the periphery of some uraninite masses is altered to unidentified minerals.

7.3.2. Results

Ion probe spots were targeted on areas of U1 uraninite without galena inclusions, and the spots were re-inspected after analysis to check for the absence of galena, although it is possible that sub-microscopic (<1 μm) inclusions could have been present. The lack of data points above Concordia is, however, consistent with an absence of galena inclusions in the analysed spots of U1 uraninite.

Analytical results are presented in Appendix Table 4.

Ten analyses were obtained for U1 uraninite in sample S3PD759 408.8 m, yielding a discordia array with a $^{206}Pb/^{238}U$-$^{207}Pb/^{235}U$ upper intercept age of 1688 ± 46 Ma and individual ^{207}Pb–^{206}Pb ages as old as 1684 ± 7 Ma (Fig. 18A). Significant discordance of the data indicates one or more episodes of lead loss.

Fifteen analyses of uraninite were undertaken on sample S3PD1050 424.0 m, targeting both U1 and U2 uraninite. The extremely small grain size of the uraninites resulted in difficulties analysing pure uraninite and three low-precision analyses were excluded from further consideration. The remaining data yield an array of highly discordant points with an upper intercept of 1421 ± 68 Ma (Fig. 18B), obtained with high MSWD (66). The seven analyses of U1 and five analyses of U2 uraninite (Fig. 18B) cannot be statistically separated to calculate ages for each generation of uraninite. This is confirmed by the similar $^{207}Pb/^{206}Pb$

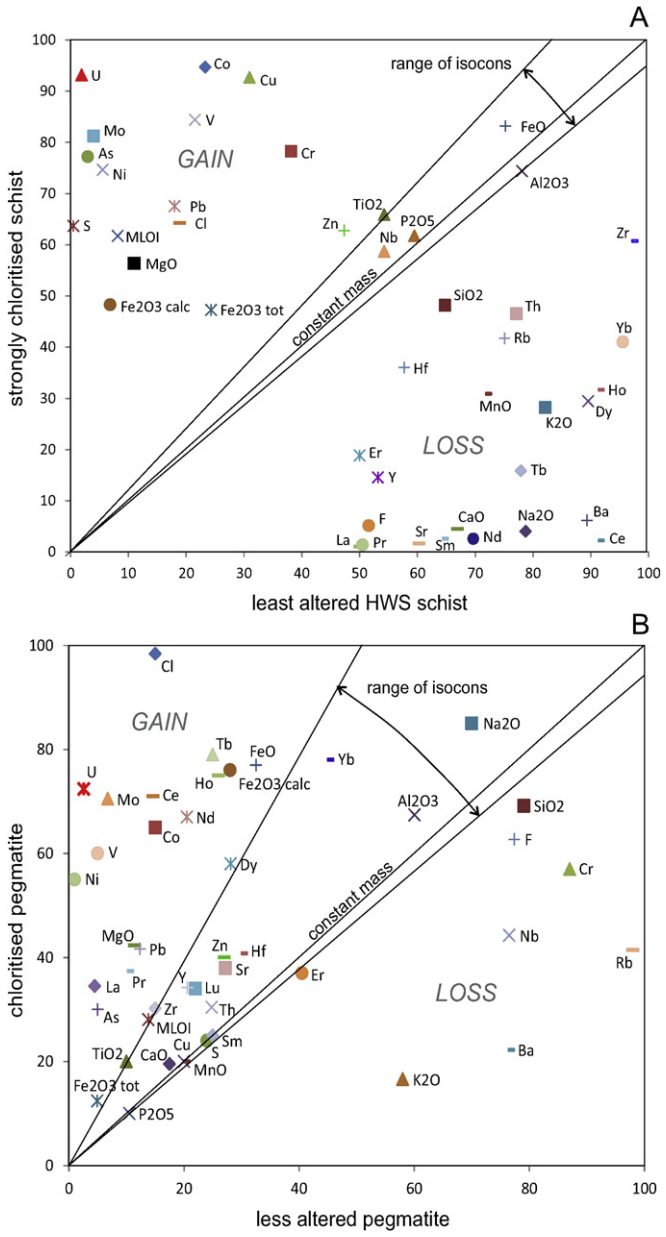

Fig. 14. Diagram of gains and losses of chemical components (Grant, 1986) during metasomatism at the Ranger 1 Number 3 orebody. Weight percent and ppm concentrations scaled to arbitrary values below 100 on abscissa and ordinate axes. We have selected the least mobile elements such as Ti, Nb and Al to define a field of little or no mass transfer, labelled 'range of isocons'. Elements plotting below this field were lost from the rock during alteration, whereas those above the 'range of isocons' field were gained. A. Least altered HWS metasedimentary schist (average of 4 samples, 2167035, 2167036, 2167037, 2169197, Table 3) compared with strongly chloritised, intensely sheared, weakly mineralised graphitic and pyritic schist from the UMS (sample 2167042, Table 3). B. Weakly sericitised pegmatite (sample 2167047, Table 3) cutting the LMS compared with chloritised equivalent pegmatite from ~1 m away (sample 2167046, Table 3).

ages calculated for the two generations of uraninite, which range from 1228 ± 17 Ma to 1388 ± 7 Ma for U1 and 1045 ± 14 to 1329 ± 6 Ma for U2 uraninite. Similarly, electron microprobe analyses suggest the U1 and U2 have similar compositions (Appendix Table 5) yet both these are different in Pb, U and Ca contents to U1 in sample S3PD759 408 m and U3 uraninite in sample S3PD730 459.7 m. A possible interpretation of the data is that fluids active between ~950 Ma and ~1390 Ma resulted in hydrothermal carbon formation along with deposition of uraninite U2, whereas the U–Pb isotopic and chemical composition of pre-existing uraninite U1 was reset during this period. Alternatively, all of the uraninite dated in sample S3PD1050 424.0 m represents U2. The geological significance of any such hydrothermal activity during this period is presently unknown.

The results for the texturally late-stage U3 uraninite in samples S3PD730 459.6 mand 459.7 m are, however, far more coherent with most analyses close to concordant. Based on the textural similarity of U3 uraninite analysed in the two closely spaced samples and their equivalent chemical composition (Appendix Table 5), U–Pb data were only acquired for sample S3PD730 459.7 m (Appendix Table 4), considering that the age would be similar for sample S3PD730 459.6 m. Although a range of $^{207}Pb/^{206}Pb$ ages were recorded, a subgroup of near-concordant analyses yielded an upper intercept age of 474 ± 6 Ma (Fig. 18B). This is interpreted to represent a discrete uraninite crystallisation event.

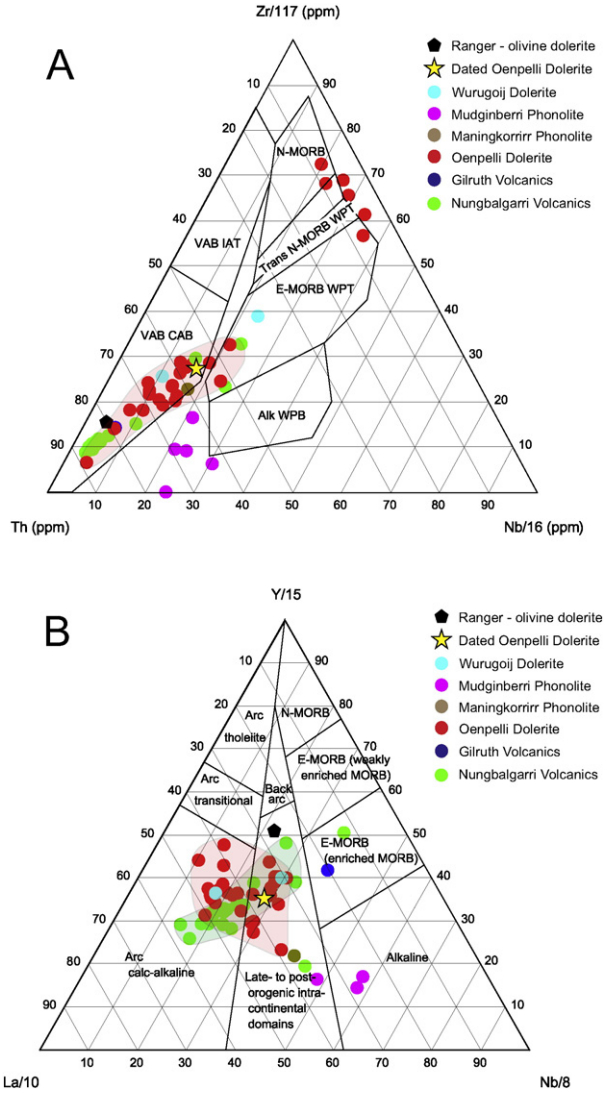

Fig. 15. A. Geochemical discriminant diagram (Zr/117–Th–Nb) after Wood (1980). B. Geochemical discriminant diagram (Y/15–La/10–Nb/8) after Cabanis and Lecolle (1989). Each diagram shows the composition of the olivine–phyric dolerite at the Ranger 1 No. 3 orebody (Table 3) compared with the dated Oenpelli Dolerite at the Nabarlek deposit (Page, 1996b; Table 3) and other mafic igneous units from the region. Data sources: Ranger dolerite — this study; Oenpelli Dolerite — Geoscience Australia, unpublished data, reproduced in Table 3; other data — Geoscience Australia OZCHEM whole-rock geochemical database.

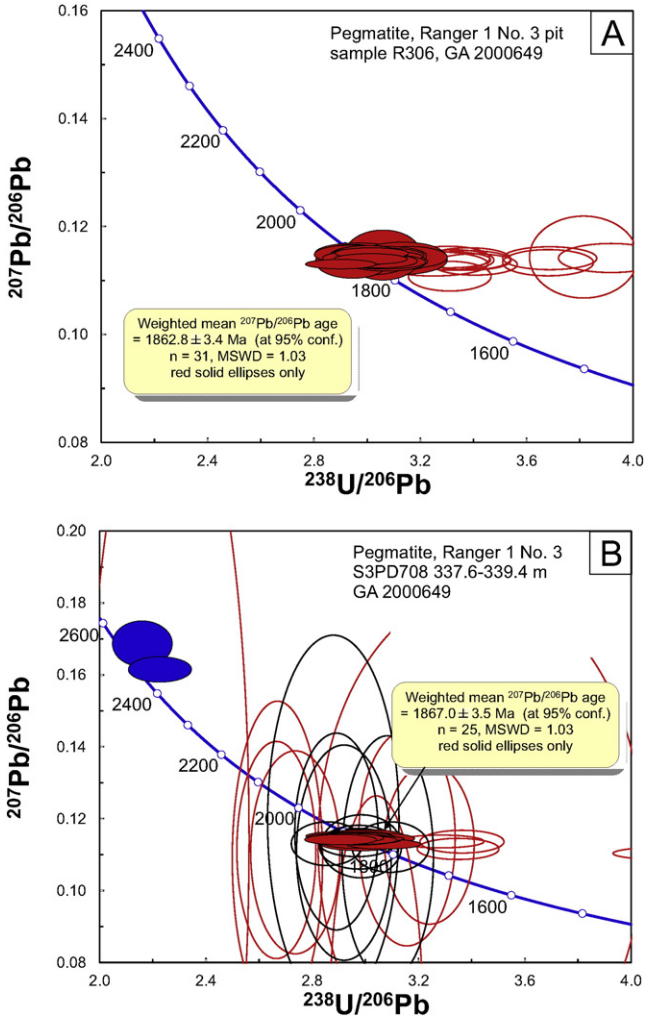

Fig. 16. SHRIMP ion microprobe U–Pb zircon dating results for pegmatites, Ranger 1 No. 3 orebody. A. Sample 2000649, massive pegmatite from the Ranger 1 Number 3 orebody pit. Age based on red solid ellipses; unfilled red ellipses represent analyses with >5% discordance; unfilled black ellipses represent analyses with >1% common lead. B. Sample 2000646, weakly foliated pegmatite from the Ranger 1 Number 3 orebody, drill hole S3PD708 337.6–339.4 m depth. Age based on red solid ellipses; unfilled red ellipses represent analyses with >5% discordance; unfilled black ellipses represent analyses with >1% common lead.

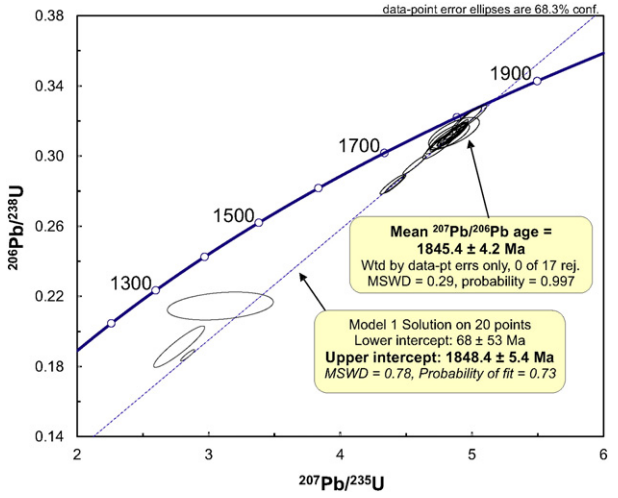

Fig. 17. SHRIMP ion microprobe U–Pb dating results for titanite in veins with amphibole-plagioclase-apatite, drillhole sample S3PD730 371.2 m.

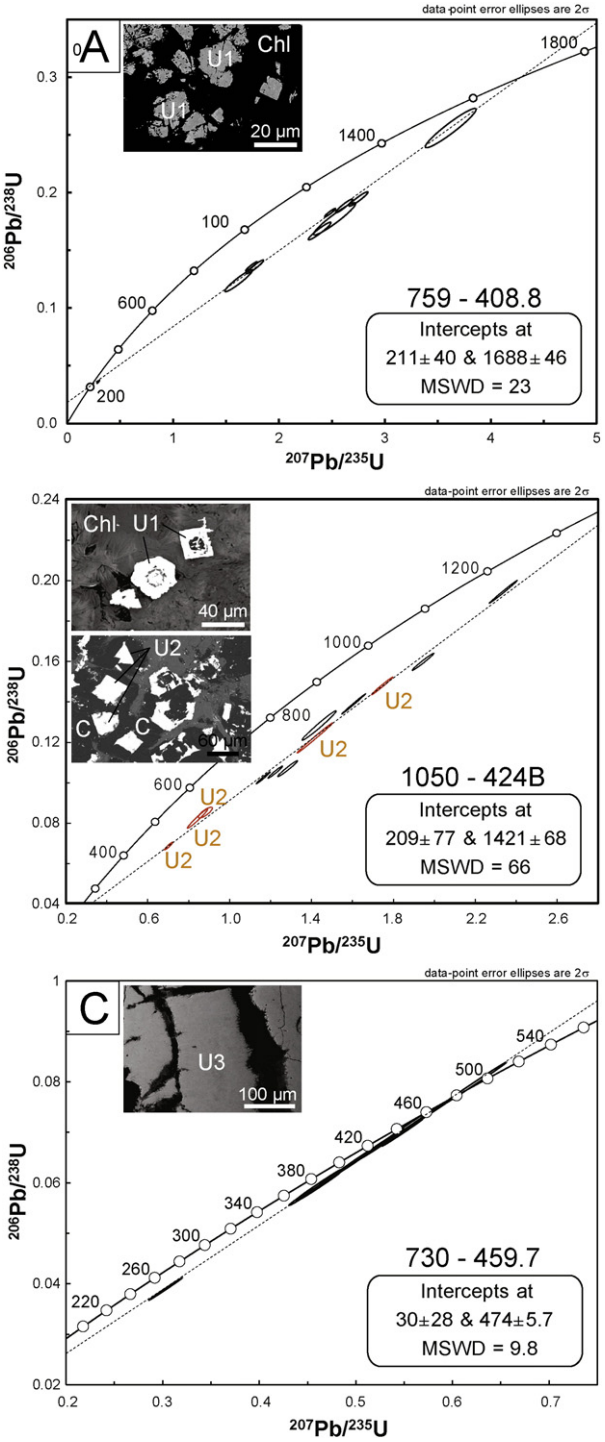

Fig. 18. Cameca ion microprobe U–Pb uraninite dating results. A. Very fine-grained disseminated U1 uraninite. Inset SEM image shows uraninite U1 within chlorite (chl). Dillhole sample S3PD759 408.8 m. B. Very fine-grained disseminated U1 and U2 uraninite. Inset SEM images show U1 in chlorite (chl) from area X in Fig. 10B, and U2 surrounded by disordered carbon (C) within cross-cutting vein in area Y in Fig. 10B. The analyses of U2 are labelled on the plot; unlabelled data represent analyses of U1. Drillhole sample S3PD1050 424.0 m. C. Massive vein of uraninite U3 and inset SEM image of U3. Drillhole sample S3PD730 459.7 m.

7.4. Uraninite EPMA chemical compositions and dating — samples and results

7.4.1. Samples

The same samples were analysed as for the Cameca ion microprobe analyses, described above (S3PD759 408.8 m, S3PD1050 424.0 m, S3PD730 459.6 m and 459.7 m).

7.4.2. Results

Electron microprobe analyses of uraninite U1 in sample S3PD759 408.8 m indicate that this generation is primary and fresh, with high Pb (mean: 18.78 wt.% PbO; Appendix Table 5) and low Si and Fe (mean: 0.14 wt.% SiO_2 and 0.58 wt.% FeO) contents, relatively elevated concentrations of these two latter elements being a good indicator of post-crystallisation alteration (Alexandre and Kyser, 2005). Thorium concentrations are below detection limit, clearly indicating that the uranium oxides are of hydrothermal rather than magmatic or metamorphic origin (Mercadier et al., 2013b). The electron microprobe results for this sample are in agreement with the U–Pb isotopic data which indicate relatively fresh uranium oxides and a U–Pb system only slightly perturbed by post-crystallisation events.

For sample S3PD1050 424 m electron microprobe analyses of uraninite U1 (within Mg-chlorite matrix) and U2 (associated with disordered carbon) indicate that these two generations have equivalent chemical composition for all the elements tested. The mean U and Pb contents for the two types are 84.94 wt.% UO_2 and 8.57 wt.% PbO, with small standard deviations of 0.88 and 1.04 respectively, clearly indicating that the two generations have indistinguishable U and Pb contents. The concentrations for these two elements are significantly different than those for uraninite U1 in S3PD759 408.8 m, especially the Pb contents. The Si concentration for U1 and U2 is higher than for U1 in S3PD759 408.8 m with a mean value of 0.60 wt.% SiO_2. This concentration is low, however, and indicates that the uranium oxides were only weakly altered.

Uraninite U3 in samples 730–459.6 m and 730–459.7 m exhibits chemical compositions which differ from the two previous samples, with high U contents (mean: 87.8–87.9 wt.% UO_2) but low Pb (mean: 5.32–5.46 wt% PbO), Ca (1.69 wt.% CaO) and Fe (mean: 0.13–0.14 wt.% FeO) contents. The concentrations of the other elements analysed are similar to those observed for U1 and U2 in both samples. The relatively constant concentrations of the different elements measured in different locations for the samples 730–459.6 m and 730–459.7 m, demonstrated by the small standard deviations, indicate that uraninite U3 did not suffer from significant post-crystallisation alteration. This confirms the results obtained for the ion probe U–Pb isotopic measurements which indicated an essentially closed isotopic system since the time of uraninite crystallisation (Fig. 18C).

Electron microprobe analyses of uraninite U1 in sample S3PD759 408.8 m yielded calculated ages as old as 1646 Ma, and a mean age of 1586 ± 87 Ma (n = 5, Appendix Table 5). This age is similar to the $^{207}Pb/^{206}Pb$ ages and a $^{206}Pb/^{238}U$-$^{207}Pb/^{235}U$ upper intercept age of 1688 ± 46 Ma obtained by ion probe, indicating that the uranium oxides are relatively fresh. Much younger chemical ages of ~700 Ma were recorded in sample S3PD1050 424.0 m for both generations of uraninite U1 and U2, with equivalent ages for the two generations; however, the Cameca ion microprobe analyses for this sample give older $^{207}Pb/^{206}Pb$ ages, from 1045 ± 14 Ma to 1388 ± 7 Ma, and a $^{206}Pb/^{238}U$-$^{207}Pb/^{235}U$ upper intercept age of 1421 ± 68 Ma. The isotopic data are all discordant and the discrepancy between the isotopic and chemical ages show that lead loss has severely disturbed the U–Pb isotopic system, which is not the case for uraninite U1 in sample S3PD749 408.8 m and U3 in sample S3PD1050 424 m. The chemical age of ~700 Ma for both generations of uraninite in the latter sample is probably geologically meaningless.

Analyses of uraninite U3 in samples S3PD730 459.6 m and 459.7 m yielded calculated ages ranging from 515 Ma to 385 Ma. These results are broadly consistent with the Cameca ion microprobe age determined for the same samples (474 ± 6 Ma), supporting the proposal of new uraninite crystallisation during the Ordovician to Silurian. This result represents the first identification of a uranium mineralising event of lower Paleozoic age in the Pine Creek Orogen, although previous studies have reported Pb-loss and isotopic resetting events in the Paleozoic (e.g., Hills and Richards, 1976; Ludwig et al., 1987; Polito et al., 2004, 2005, 2011; Chipley et al., 2007).

8. Discussion

8.1. Introduction — key observations

The new observations reported in this study provide fresh insights on the spatial, temporal and genetic controls on uranium mineralisation at the Ranger 1 deposit, with implications for unconformity-related uranium deposits in general. The new paragenetic framework and geochronology results form the basis of an integrated model of the evolution of the Ranger mineral system that is significantly different to previous models yet are consistent with key results of earlier studies. Observations from previous and current work on unconformity-related uranium mineral systems of the ARUF, including the Ranger 1 deposit, that need to be explained by any model are summarised below.

- Higher grade uranium mineralisation at the major Ranger, Jabiluka and Koongarra deposits is hosted by metasedimentary rocks of the Paleoproterozoic Cahill Formation. The small but high grade Nabarlek deposit is hosted in different Paleoproterozoic units that lack carbonate rocks at least locally.
- At the Ranger deposit these host rocks were intensely sheared at medium metamorphic grade during the Nimbuwah event, then subjected to a retrograde shearing event (Shoobridge event), followed by initial chloritisation and brecciation.
- Pre-ore silicification and/or quartz veining/infilling is present at most if not all of the major uranium deposits in the ARUF, as replacements of carbonate rocks (Ranger, Jabiluka), or near the Oenpelli Dolerite (Nabarlek), or as silicified fault zones (Koongarra). At the Ranger deposit minor uraninite commenced deposition during the silicificaition event, accompanied by magnesian tourmaline (Mg-foitite), fine muscovite and Fe-sulfides. At the Jabiluka deposit rare examples of quartz–uraninite veins are present (Polito et al., 2005), and at the King River prospect these are common (Polito et al., 2011).
- Uranium ore at the Ranger deposit most commonly occurs in the Mg-chlorite-rich matrix of breccias within the Upper Mine Sequence and also occurs as veinlets and disseminations within the partly silicified carbonate rocks of the Lower Mine Sequence.
- At Ranger Mg-rich chlorite which became more Fe-rich later in the main uraninite mineralisation event; a second generation of tourmaline (Mg-foitite) also was deposited with uraninite, whereas quartz was corroded by chlorite.
- White mica (sericite, illite) alteration generally occurs peripheral to inner chloritized alteration zones (Ranger, Jabiluka, Koongarra) but this zoning is reversed at the Nabarlek deposit (Wilde and Wall, 1987; Polito et al., 2004).
- Alteration is zoned at the Ranger 1 Number 3 orebody from inner Mg-chlorite-rich U-mineralised zones through silicified zones to hematitic and finally outer, sericite and Fe-Mg-chlorite alteration.
- Intensely chloritised and uranium-mineralised Cahill Formation rocks at Ranger are strongly enriched in Mg, Co, Cu, Cl, Mo, V, Ni and S; very depleted in Na, Ca, Sr, LREE, Y and K; and moderately depleted in Si (Fisher et al., 2013; this study). The LREE may have been enriched in some outer alteration zones (Fisher et al., 2013), potentially in APS minerals, whereas MREE and HREE from the dissolution of accessory minerals (monazite for example) may have been incorporated in uraninite.
- The ore-hosting breccias at Ranger post-date the D1 and D2 shearing events and the intrusion of olivine–phyric dolerite that is chemically similar to the 1723 ± 6 Ma Oenpelli Dolerite.
- The oldest individual uraninite U–Pb or EPMA chemical ages in the ARUF are ~1685–1690 Ma (Polito et al., 2011); the oldest radiometric age for uraninite-rich samples in the ARUF is proposed at 1737 ± 20 Ma at the Ranger 1 deposit (Ludwig et al., 1987).
- Mineralisation at the Ranger 1 Number 1 and Number 3 orebodies was controlled by post-Oenpelli Dolerite normal faults according to Hein (2002) but recent work by Energy Resources Australia at the Ranger 3

Deeps zone (Ranger 1 Number 3 orebody) shows a spatial association of higher grade mineralisation with breccias in faults with reverse components of movement on east–west cross sections. Faults with inferred reverse displacements are also present at the Koongarra, Jabiluka and Nabarlek deposits.

- Only rare, presently subeconomic, uranium mineralisation is known to be hosted by the Kombolgie Subgroup (e.g., above the unconformity with metamorphic basement at the Jabiluka deposit; Gustafson and Curtis, 1983), which has a maximum depositional age of between ~1820 Ma and ~1720 Ma (Hollis and Wygralak, 2012).
- The Kombolgie Subgroup contains disseminated hematite with an oldest paleomagnetic age of ~1710 Ma (Giddings and Idnurm, 1993), corresponding to a major bend on the Australian Polar Wander Path of Idnurm (2000); hematite was in places removed during intense chloritisation (Gustafson and Curtis, 1983).
- Basement rocks including Archean granitic gneisses in the ARUF have been regionally altered beneath the unconformity to depths of several tens of metres to hematite–illite ± kaolinite–diaspore-bearing assemblages and possibly have been chloritised at greater depths. Approximately half of the uranium has been leached from the hematite–illite zones along with Na, Sr, Pb, Ba and possibly some Mg (Miller et al., 1992).
- Alumino-phosphate-sulfate (APS) light REE-bearing minerals are present within the sub-unconformity alteration and in the lower Kombolgie Subgroup of the ARUF where they replaced U-bearing monazite (Beaufort et al., 2005; Gaboreau et al., 2005; this study). The APS minerals vary systematically in composition from distal Sr- and SO_4-rich types to REE- and P-rich compositions closer to uranium mineralisation (Gaboreau et al., 2005).
- Fluid inclusion data for the ARUF indicate the involvement of brines of widely varying Na:Ca:Mg ratios, salinities and temperatures, consistent with the presence of three fluids of differing properties during the formation of post-ore and/or syn-ore quartz in the uranium deposits of the ARUF and in the Kombolgie Subgroup (Wilde et al., 1989; Derome et al., 2003, 2007; Polito et al., 2004, 2005, 2011). Although most stable and radiogenic isotope data point to basinal brines from the McArthur Basin as the dominant source of the ore fluids (Maas, 1989; Polito et al., 2004, 2005, 2011), a subset of the data indicate extensive interaction of some fluids with Archean and Paleoproterozoic basement rocks. Interestingly, a low-salinity fluid has been observed along with brines in fluid inclusions in all the deposits studied in ARUF, while such fluid has not been described for the Athabasca deposits.
- Two later generations of uraninite mineralisation have been identified at the Ranger 1 deposit, one with a poorly constrained age of ~1420 Ma to ~1040 Ma, and a third event dated at 474 ± 6 Ma (uraninite U–Pb ion probe ages). The importance of these events for the uranium endowment of the ARUF is not yet understood, although such mineralisation potentially could yield high grades.

A summary of event timing for the ARUF, including new geochronology results from this study, is presented in Fig. 19. These data and observations may be reconciled in a multi-stage model for the Ranger unconformity-related uranium mineral system, as shown in Fig. 20 and described below.

8.2. Nimbuwah event (~1865–1855 Ma) and amphibole-plagioclase-titanite veining (~1845 Ma)

The structural and lithological architecture of the ARUF was largely established during the regional tectonothermal and intrusive Nimbuwah event at ~1865–1855 Ma (Fig. 20A), and was fundamental in controlling the location of subsequent uranium mineralisation. At the Ranger deposit this D1 event involved the formation of shallow east-dipping high strain (shear) zones subparallel to compositional layering within the Cahill Formation near its contact with the underlying Nanambu Complex, and the emplacement of pegmatites during and after the shearing. The steep orientations of the later pegmatites (Fig. 8A, B) may indicate a component of local extensional movement although regional thrusting also occurred during the Nimbuwah event (Hollis et al., 2011). Plastic deformation of feldspars in the most deformed pegmatites is compatible with the medium grade metamorphic conditions under which the host metasedimentary rocks were deformed during the Nimbuwah event. The zircon U–Pb ages obtained in this study for two syn- to post-tectonic pegmatites from the Ranger 1 Number 3 orebody constrain the minimum age of the D1 shearing to ~1863–1867 Ma. This result suggests that the monazite U–Pb age of 1847 ± 1 Ma from a pegmatite at the Ranger 1 deposit by Annesley et al. (2002) either represents a later stage of pegmatite that post-dates the Nimbuwah event (Hollis and Wygralak, 2012) or it does not represent the crystallisation age of the pegmatite. In the latter case the 1847 ± 1 Ma age may not record the end of the Nimbuwah event as others have reported (e.g., Worden et al., 2008). The monazite age is, however, within error of the titanite U–Pb of 1845.4 ± 4.2 Ma determined in this study. Our interpretation is that both of the monazite and titanite ages record a post-Nimbuwah thermal event during which monazite grew within pegmatites, and when veins of amphibole–plagioclase–titanite–apatite were emplaced.

8.3. Shoobridge event (~1800 Ma) and deposition of the Kombolgie Subgroup

Based on current, albeit sparse, evidence the D1 shear zone at Ranger was reactivated (D2) under retrograde greenschist facies conditions when relatively Fe-rich chlorite replaced biotite, sericite replaced feldspars, and monazite grew at 1800 ± 9 Ma (Figs. 19, 20B; Mercadier et al., 2013b). It is also possible that gold and sulphur (pyrite) were introduced at this time in Shoobridge-aged shear zones in the region, given the ~1800 Ma ages of some gold deposits in the PCO (Mercadier et al., 2013b). At the Ranger 1 deposit local mylonitic and S–C shear fabrics overprinting the D1 shear fabrics are attributed to this D2 event. The apparent low abundance of pegmatitic material within the Upper Mine Sequence as compared with the Hangingwall Sequence may be a consequence of intense alteration and deformation within the Upper Mine Sequence during D2. Many of the reverse faults, thrusts, folds of D1 shear fabrics, and large-scale S–C structures at the Ranger 1 deposit reported by Hein (2002) as 'local D3' structures, and also reported by Potma et al. (2012), probably developed during this D2 event at brittle-ductile conditions and at low metamorphic grade. It is possible that the reverse fault architecture shown in Energy Resources Australia cross sections of the Ranger 3 Deeps zone initially developed during the Shoobridge event at ~1800 Ma and was reactivated during later hydrothermal and uranium mineralising events.

Following the Shoobridge event, exhumation and erosion of the Archean and Paleoproterozoic rocks formed an unconformity surface upon which the Kombolgie Subgroup of the McArthur Basin was deposited, most likely soon after ~1800 Ma. It is unclear whether a paleosol developed at this time, (cf. Needham, 1988; Miller et al., 1992). The age of mafic volcanic units within the Kombolgie Subgroup is presently unknown but if these volcanic rocks are correlatives of the Siegel Volcanics in the southern McArthur Basin (Scott et al., 2000; Polito et al., 2011) then the age of this part of the Kombolgie Subgroup would be constrained to ~1780–1760 Ma. Diagenesis may have commenced as early as 1798 ± 13 Ma and continued over an extended period, as recorded in Ar–Ar ages for illite in the Kombolgie Subgroup (Fig. 19; Polito et al., 2011). The resultant diagenetic aquifers and aquicludes within units of differing detrital mineralogy and composition were important controls on fluid flow and fluid chemistry within the basin (Polito et al., 2005; Hiatt et al., 2007). The McArthur Basin including the Kombolgie Subgroup was subjected to the Mid-Tawallah Compression at ~1750–1730 (Bull and Rogers, 1996), when it is possible that reverse faults developed and/or were reactivated in the ARUF, including those hosting later uranium mineralisation.

8.4. Oenpelli Dolerite (~1723 Ma)

Kendall (1990) described dolerite dykes at the Ranger 1 No. 1 orebody as steeply dipping bodies up to 70 m thick in the LMS, and as blocks and veins up to 40 cm thick in the UMS, "intruded along fault lines which are associated with primary uranium emplacement". Potma et al. (2012) showed the 3-dimensional distribution of "mafic dykes" at the No. 1 orebody, where they are most abundant within the LMS below and down-dip from zones of chert and uranium mineralisation. Hein (2002) described the mafic dykes at both the No. 1 and No. 3 orebodies as massive, generally chloritised, olivine–phyric dolerite and noted their cross-cutting relationships with the main tectonic fabric in host rocks. Both Kendall (1990) and Hein (2002) correlated the olivine–phyric dolerite with the Oenpelli Dolerite. We concur with this interpretation, based on its mineralogy and chemical composition (see Whole-rock Geochemistry); alternatively the Ranger dolerite may be affiliated with mafic volcanic units within the Kombolgie Subgroup. At the Nabarlek deposit Polito et al. (2004) suggested that silicification was spatially and temporally associated with emplacement of the Oenpelli Dolerite. Our observations of drill hole Na83 at Nabarlek, which intersected silicified host rocks beneath (and spatially separate from) the Oenpelli Dolerite, indicate a mineral assemblage of quartz with minor pyrite and white mica/clay 'bleaching'. It is interesting to note the similarity of this assemblage to that of silicification at the Ranger 1 deposit.

8.5. Uranium mobilisation and ore formation (~1720–1680 Ma)

The model illustrated in Fig. 20C and D shows an early, convective, stage of hydrothermal activity in the Ranger mineral system (Fig. 20C), and an ore-forming stage during extensional or strike-slip tectonism involving lateral and downwards fluid flow (Fig. 20D). Both of these stages are inferred to have occurred after intrusion of the Oenpelli Dolerite and during the period ~1720–1680 Ma which also included intermittent regional tectonism (Scott et al., 2000; 'local D4' normal faulting of Hein, 2002) and magmatism represented by the mafic West Branch Volcanics (~1712–1705 Ma) and the felsic Jimbu Microgranite (~1720 Ma) (Fig. 19). Based on fluid flow modelling by Oliver et al. (2006) and Cui et al. (2012) the convective systems are likely to have been disrupted temporarily during extensional or strike-slip tectonism, with circulating fluids diverted into active fault zones. This sequence of processes may have been repeated during the ~1720–1680 Ma period.

The convective hydrothermal systems involved fluid down-draw, lateral flow, and upflow as well as fluid mixing above upflow zones (Fig. 20C). These processes could explain many of the features in the regional sub-unconformity alteration zones, the silicification observed at the Ranger deposit, and the wide variations in Na:Ca:Mg ratios and salinities of fluids trapped in basin and basement rocks (e.g., Wilde et al., 1989; Derome et al., 2003; Polito et al., 2004, 2005). During convection Na ± Mg-bearing brines derived from the McArthur Basin are envisaged to have been drawn down through the Kombolgie Subgroup and into the sub-unconformity alteration zone, with flow controlled partly by topographic highs in the unconformity surface, diagenetic aquicludes/aquifers, and cross-stratal faults. We interpret the regional sub-unconformity zones of hematite–illite–chlorite as alteration zones rather than paleo-regolith zones (cf. Miller et al., 1992), and contend they were produced by the reaction of oxidised basin-derived hydrothermal fluids and/or diagenetic fluids with basement rocks at temperatures of ~180–200 °C (Gaboreau et al., 2005). Although permeabilities of the metamorphic basement rocks generally would have been much lower than those of diagenetic aquifers in the overlying Kombolgie Subgroup, the fact that sub-unconformity alteration extends to depths of more than 50 m and uranium mineralisation extends to depths of more than 300 m beneath the unconformity demonstrates that permeabilities were (at times) sufficient for basinal fluids to penetrate deeply into the basement rocks. Basement permeabilities would have been enhanced during active deformation particularly within fault zones.

As noted above, approximately half of the uranium in the sub-unconformity hematite–illite alteration zones was removed, and we propose that this alteration zone constitutes part of the source of the uranium presently located in the deposits of the ARUF. The diagenetic/hydrothermal fluids also leached Na and to a lesser extent Mg from the hematite–illite alteration zone (Fig. 4) and locally precipitated uraninite in deeper (chloritic) and reduced parts of the alteration profile (Fig. 3C, D). Where these fluids encountered more permeable basement such as pre-existing fault/shear zones deeper convective circulation resulted in extensive fluid-rock exchange and chloritic alteration (dark green zones in Fig. 20C). Magnesium metasomatism is well known in sub-seafloor hydrothermal systems where Mg-rich seawater reacts with basalt or sediment (Seyfried and Mottl, 1982; Seewald et al., 1990; Weis, 2014). Uranium appears to be almost quantitively removed from seawater in such systems (James et al., 2003). Consequences of Mg-metasomatism in sub-seafloor systems include the formation of Mg-rich minerals, increased H^+ and Si contents of the fluids, and leaching of a range of metals from the altered rock (Seyfried and Mottl, 1982). We suggest that analogous processes may have operated near the basin-basement interface in the ARUF involving basinal brines. In particular, intense Mg-chloritisation within the basement may have been due to heating of Mg-rich evolved basinal brines in down-flow zones, resulting in acidic fluids with elevated contents of Si and other metals. Magnesium metasomatism would be strongly favoured by high concentrations of magnesium in the initial basinal brines, where these were derived via surface evaporation of seawater and reached epsomite saturation (Derome et al., 2003). In such environments, the initial Mg content in the brines could attain concentrations of >2 $mol.L^{-1}$ (Fontes and Matray, 1993). Minor dispersed low-grade uranium mineralisation is likely to have formed at this time (Fig. 20C, "+U"). Zones of convective upflow of such fluids may have been the sites of silica deposition accompanied by white mica and Fe sulfide minerals, as observed in the silicification stage at the Ranger 1 deposit. In this model, localised mixing of the deeply-circulated silica-bearing fluid with uranium- and Mg-bearing fluids from the sub-unconformity alteration zone led to minor uraninite deposition with silica and Mg-foitite, as present in some silicified zones at the Ranger 1 deposit. This mixing model predicts that uranium mineralisation could be present at and above the unconformity ("U + ?" in Fig. 20C), and may explain the spatial zoning of the APS mineral compositions (Beaufort et al., 2005; Gaboreau et al., 2005) representing relatively reduced conditions ("redAPS" in Fig. 20C) near and above fluid upflow zones to relatively oxidised conditions ("oxAPS", Fig. 20C) more distally within the hydrothermal systems. Hints that a fluid mixing process operated in the ARUF are offered by the rare presence of uranium mineralisation in chloritised Kombolgie Subgroup rocks above the Jabiluka deposit (Gustafson and Curtis, 1983). This mixing model also explains the very wide range of Na:Ca:Mg ratios of brines trapped in hydrothermal quartz in the Kombolgie Subgroup (Derome et al., 2003, 2007). We further propose that silicification of carbonate rocks in the LMS at Ranger and at the Jabiluka deposit may have been in response to neutralisation of acidic silica-bearing fluids, a process which generates CO_2 and may induce silica saturation (Fournier, 1985).

Transient regional extensional and strike-slip tectonism (Fig. 20D) caused a reversal of fluid flow in the zones of previous upflow. Oxidised Na–Mg–Ca–U brines from the basin were drawn laterally through the sub-unconformity alteration zones, leaching U at progressively deeper levels, and transporting U and Mg into highly permeable normal- and strike-slip fault breccia zones in reactivated D1/D2 shear zones within the reduced Cahill Formation. Uranium was deposited via reduction ± pH or other chemical changes during fluid-rock reaction, although fluid mixing also may have been locally

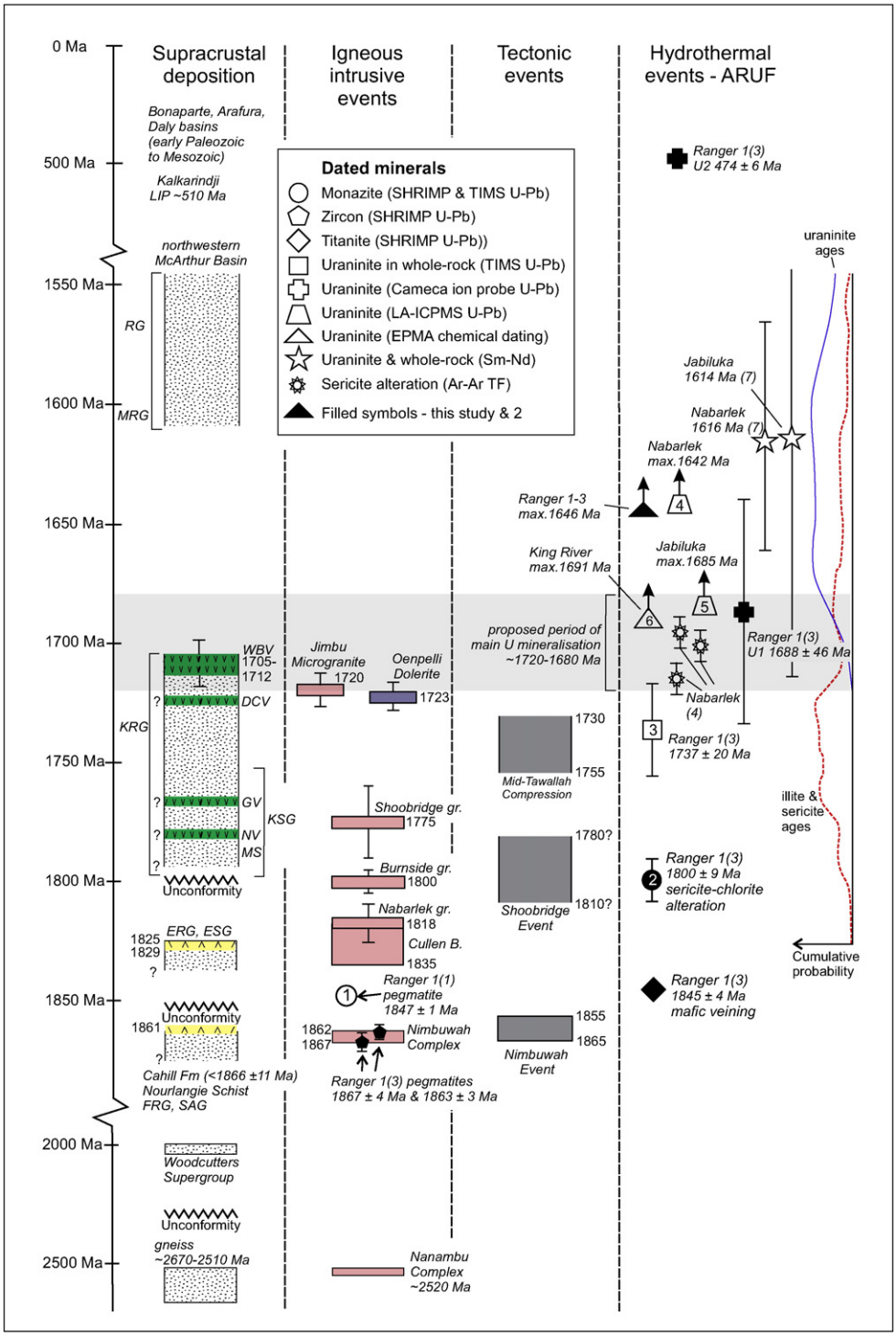

Fig. 19. Event diagram with new geochronology results for the ARUF (Nimbuwah Domain, Pine Creek Orogen) and for the northern McArthur Basin. Sources of age data for supracrustal depositional units, igneous intrusive events and tectonic events from compilations of Hollis et al. (2011); Hollis and Wygralak (2012) and Ahmad and Munson (2013). Error bars shown for selected key units and ages. Age of the Shoobridge event based on Stuart-Smith et al. (1993) and Mercadier et al. (2013b), with peak most likely at ~1800 Ma (dark grey band) and associated tectonothermal activity from ~1810 Ma to ~1780 Ma. Mid-Tawallah Compressional Event from Bull and Rogers (1996). Traces at right are cumulative probability plots, in red: sericite and illite ^{40}Ar-^{39}Ar individual step ages, representing diagenetic and hydrothermal events, and in blue: uraninite $^{207}Pb/^{206}Pb$ individual LA-ICPMS analysis ages, from Polito et al. (2011). Sources of numbered ages: 1 — Annesley et al. (2002); 2 — Mercadier et al. (2013b); 3 — Ludwig et al. (1987); 4 — Polito et al. (2004); 5 — Polito et al. (2005); 6 — Polito et al. (2011); 7 — Maas (1989). Arrows indicate these data are the oldest individual point analysis ages (laser-ICPMS, EPMA). Abbreviations: DCV — Diamond Creek Volcanics; ERG — Edith River Group; ESG — El Sherana Group; Frg — Finnis River Group; GV — Gilruth Volcanics; KRG — Katherine River Group; KSG — Kombolgie Subgroup; MRG — Mount Rigg Group; MS — Mamadewerre Sandstone; NV — Nungbalgarri Volcanics; RG — Roper Group; SAG — South Alligator Group; WBV — West Branch Volcanics.

important. Indeed, mixing could have occurred at the interface between the decaying (reduced-fluid) upflow regime and the newly established (oxidised-fluid) downflow regime (Oliver et al., 2006). The deposition of Mg-foitite and uraninite during both the silicification event and during the later main ore-forming event associated with chloritisation could be indicative of the simultaneous presence of the two fluids. Although involvement of fluids in ore formation that have extensively reacted with basement remains

unclear, stable and radiogenic isotope data do support such a proposition. The relatively 'heavy' oxygen isotopic compositions of some chlorites, quartz and of some uraninite in the ARUF (Polito et al., 2004, 2005, 2011) may record extensive reaction of fluids with basement rocks. Moreover, if uranium ore formation occurred at ~1720–1680 Ma, as suggested herein, then the Sm-Nd isotopic signatures reported by Maas (1989) for uranium ores in the Ranger deposit are consistent with a contribution of Nd (and by implication other metals) from the Archean and Cahill Formation basement rocks.

As noted earlier, some uranium mineralisation at the Ranger 1 Numbers 1 and 3 orebodies occurs above and within zones of thinned and silicified carbonate rocks of the LMS (Fig. 5B). Carbonate dissolution during silicification may have created relatively permeable zones that were utilised by fluids during the later main ore-forming event. At detailed scale, higher grade uranium mineralisation in the Ranger 3 Deeps zone is hosted in breccias within trough-like zones in the UMS-LMS contact which appear to be the result of displacement on east-northeast dipping, north–northwest trending steep faults with a reverse component of displacement on east–west cross sections. The timing of this faulting is presently unclear in relation to the regional geological and local hydrothermal events described above, and requires further investigations. Nevertheless, this geometry is consistent with regional north–northwest–south–southeast extension and localised strike-slip displacement in suitably oriented transfer zones. More broadly in the ARUF, occurrences of Kombolgie Subgroup at the Ranger 1, Jabiluka and Koongarra deposits at structural levels below that of the regional unconformity could be due to combinations of normal and strike-slip faulting including negative flower structures. This interpretation differs from previous suggestions of simple reverse faulting.

8.6. Hydrothermal disordered graphitic carbon and second-stage uraninite U2

An unexpected result of the present study was the identification of quartz veinlets with disordered graphitic carbon enclosing disseminated U2 uraninite, within the Ranger 3 Deeps zone. This style of mineralisation has not been described previously in the ARUF. Although apparently of

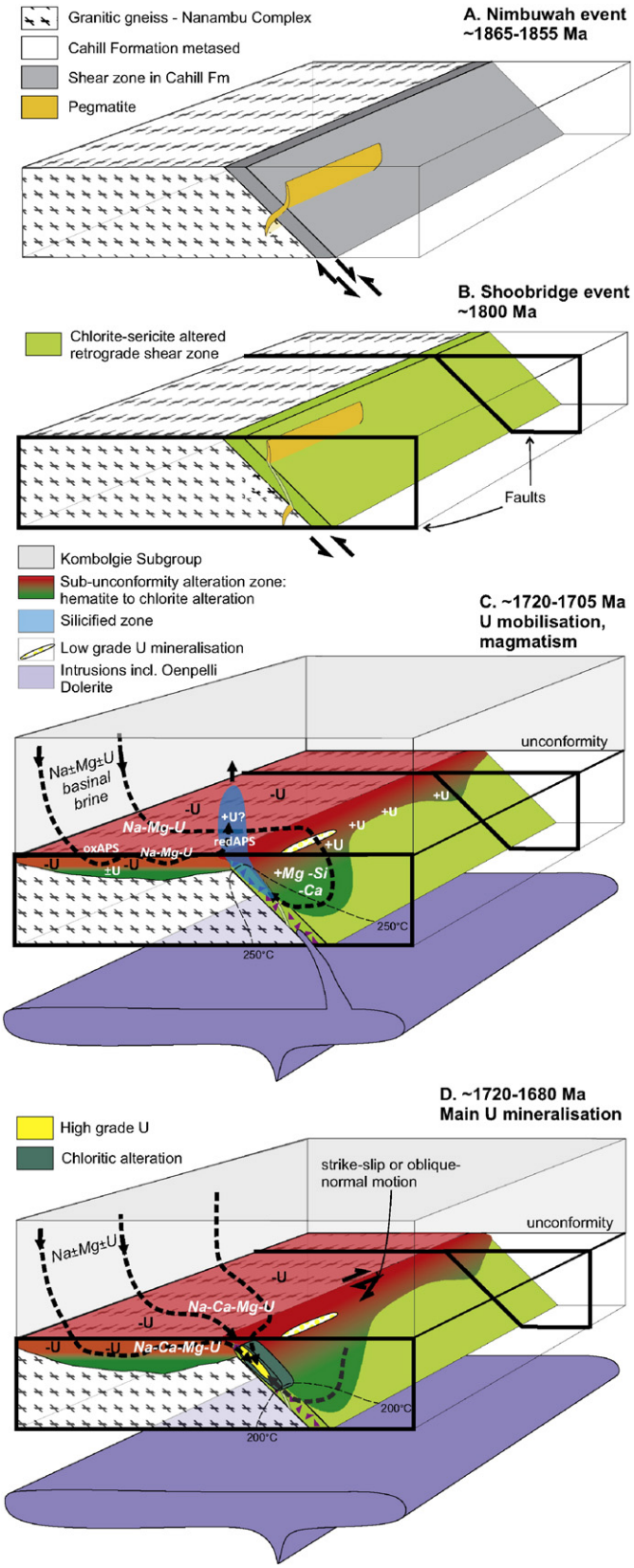

Fig. 20. Model of the evolution of unconformity-related uranium mineral systems in the ARUF, based on constraints from the Ranger 1 and other deposits in the ARUF and from regional geology (see text).
A: Nimbuwah event and development of D1 shear zones at medium metamorphic grade, with late- to post-shearing pegmatite intrusion.
B: Shoobridge event, reactivating the D1 shear zones and resulting in retrograde Fe-chlorite with sericite–monazite (±Au?) alteration in D2 shear zones.
C: Model of convective stages of fluid flow and hydrothermal alteration (post-Kombolgie Subgroup), driven by regional magmatism (e.g., sills of the Oenpelli Dolerite). Convective periods may have alternated with strike-slip or trans-tensional faulting episodes (see D). Leaching of uranium (symbol: -U) occurred within the hematitic (red) upper parts of sub-unconformity regional alteration zones, mainly on paleo-topographic highs, by Na ± Mg ± U basinal brines. Some uranium may have been locally re-precipitated (symbol: ±U) within chloritic lower parts of the sub-unconformity alteration. These brines evolved to Na–Ca–Mg–U-rich compositions during reaction within the sub-unconformity alteration zones. Lateral migration of the evolved brines into, and convective circulation within, the D1/D2 shear zones resulted in low grade uranium mineralisation (e.g., anomalies between Ranger 1 and Jabiluka), deeper chloritisation (green), and modification of the brines at depth to Si- and Ca-rich compositions. Silicification is envisaged as occurring in upflow zones of convective systems (blue). Mixing of the Si-bearing evolved brines with U-bearing Na–Mg–Ca brines may have occurred close to the unconformity, with the possibility of uranium mineralisation hosted by the McArthur Basin (symbol: +U?). Conductive heating of wall rocks by the ascending fluid (Weis, 2014) is shown schematically with a 250°C contour. Compositions of APS minerals are spatially zoned within the mineral system from those stable at oxidised conditions (symbol: oxAPS) in distal areas to those stable at reduced conditions (symbol: redAPS) proximal to upflow zones of reduced fluids.
D: High grade uranium mineralisation during stages of strike-slip or oblique-normal faulting, which temporarily disrupted convective systems and resulted in generalised fluid downflow (Oliver et al., 2006; Cui et al., 2012) and deeper leaching of uranium from sub-unconformity alteration zones. Magnesium metasomatism and uranium mineralisation in the basement occurred in response to heating and reduction of the down-drawn, oxidised, U-bearing Na–Ca–Mg brines. An alteration aureole (including chloritisation and hematisation) migrated downwards and possibly laterally along the D1/D2 shear zone, with fluid flow controlled by high permeabilities within fault-jog breccia zones. Processes represented in (C) and (D) may have been repeated during the period ~1720 Ma to ~1680 Ma.

limited volume, such veinlets may result in locally high grade uranium intersections within mainly the Lower Mine Sequence, particularly in silicified zones. The origin of the disordered carbon veinlets with U2 uraninite is unknown, although ion probe dating suggests emplacement between ~1420 Ma and ~1040 Ma. Furthermore, laser Raman data indicate crystallinities typical of temperatures during low grade metamorphic conditions, which must be considered in any explanation of origin. Based on uraninite U–Pb isotope data, events have been previously recorded at ~1360 Ma by Polito et al. (2004, 2005) at the Nabarlek deposit ($^{206}Pb/^{238}U$–$^{207}Pb/^{235}U$ upper intercept age at 1393 ± 76 Ma) and at the Jabiluka deposit ($^{206}Pb/^{238}U$–$^{207}Pb/^{235}U$ upper intercept age at 1358 ± 87 Ma). Collectively, these results point to a regional and thus potentially significant event around 1400 Ma for the uranium endowment of the region.

Oxidation of dissolved or gaseous CH_4 to solid carbon, or reduction of CO_2 to carbon, are possible chemical processes that may be linked to deposition of the U2 uraninite that is intimately associated with the disordered carbon. Notwithstanding possible kinetic limitations, some theoretically viable reactions include:

$$CO_2 + 2H_2 = C + 2H_2O$$

$$CO_2 = C + O_2$$

$$CH_4 + O_2 = C + 2H_2O$$

$$CH_4 = C + 2H_2$$

$$CH_4 + CO_2 = 2C + 2H_2O$$

Similar processes have been proposed for the formation of hydrothermal graphite in other geological settings including gold deposits (e.g., Craw, 2002).

Alternatively, if migrating hydrocarbons (e.g., from overlying basins) had been trapped in these veins, then any record of a lower temperature origin must have been lost during thermal maturation. The discordered carbon at the Ranger deposit differs in composition and crystallinity from the bituminous nodules reported from several uranium deposits in the Athabasca Basin. These have been interpreted to have formed by trapping of migrating hydrocarbons where radiation-induced radiolysis of water occurred in proximity to uranium minerals (Kyser et al., 1989). It is interesting to note that similar disordered carbon with uraninite inclusions has been reported in the Browns U-bearing Cu–Pb–Co–Ni deposit and in granites in the Rum Jungle mineral field in the western Pine Creek Orogen (McCready et al., 2003, 2004).

8.7. Late-stage uraninite U3 mineralisation

A further unexpected result of the present study was the identification of veinlets of uraninite U3 within the Ranger 3 Deeps zone. As for the uraninite U2-bearing veins, the U3 veinlets appear to be sparse but may result in locally high grades of uranium. Ion microprobe U–Pb dating of massive uraninite U3 veinlets yielded an age of 474 ± 6 Ma, supported by chemical ages of the uraninite which are within error of the ion microprobe age. The results imply that fluids capable of transporting and depositing uranium were present at relatively deep levels (>300 m) within basement rocks during the Ordovician and/or Silurian, at a time when the Daly Basin and age equivalents may have covered parts of the PCO including the ARUF. This is the first reported uranium mineralisation of Paleozoic age in the PCO, which we believe is distinct from the various lead-loss events including some of Paleozoic age proposed by other workers (Hills and Richards, 1976; Ludwig et al., 1987; Polito et al., 2004, 2005, 2011; Chipley et al., 2007). Whether the new mineralisation involved redistribution of existing uranium in the Ranger deposit or introduction of uranium from outside the orebodies is unknown.

9. Mineral system components and exploration for unconformity-related uranium deposits

New insights from the present study of the Ranger mineral system that may be significant for exploration strategies in the ARUF are as follows, presented in terms of the four essential components of unconformity-related uranium mineral systems.

9.1. Architecture of fluid flow paths

Architecture of fluid flow paths. The D1 shear zones that formed during the ~1865–1855 Ma Nimbuwah event were a fundamental control on later uranium mineralisation at the Ranger deposit. The D1 shear zones were important because (a) they were the locus of later deformation (e.g., Shoobridge event, D2, and post-Shoobridge brecciation) and hence permeability creation in the basement, and (b) they were chemically different to surrounding basement rocks, with greater abundances of graphite and Fe^{2+}-bearing minerals. The reduced-iron minerals were introduced during the ~1845 Ma mafic veining event; the ~1800 Ma Shoobridge event (e.g., pyrite and Fe-rich chlorite, Mercadier et al., 2013b); and in the olivine–phyric Oenpelli Dolerite. Electrical geophysical methods have long been used to target conductive graphitic zones associated with unconformity-related uranium deposits. Additionally, rheological contrasts such as that between the Archean granitic gneisses or nimbuwah granitoids and metasedimentary rocks of the Cahill formation or Nourlangie Schist also may have been the locus of major D1 shear zones. Gravity and magnetic geophysical data may be useful in identifying such breaks at regional to deposit scales

The permeability architecture within the Kombolgie Subgroup is the second key part of the fluid flow system. Previous work shows the importance of diagenetic aquifers and diagenetic aquicludes in controlling basinal fluid flow (e.g., Hiatt and Kyser, 2000; Hiatt et al., 2007). Based on this understanding, the intersections of diagenetic aquifers with reduced basement rocks along the slopes of paleo-topographic basement highs were proposed to be favourable sites of uranium mineralisation in the ARUF (Polito et al., 2004, 2005, 2011). Paleocurrent directions in the Kombolgie Subgroup (Ojakangas, 1979; Needham, 1988; Sweet et al., 1999; Polito et al., 2011) suggest such paleo-highs existed near the Nabarlek deposit (Myra High) in a region where Archean rocks have been identified (Hollis et al., 2009), and in the area of the Archean Nanambu Complex to the west and northwest of the Ranger and Jabiluka deposits. The Ranger deposit therefore may be situated either on the southwestern flank of the Myra High (Polito et al., 2011) or on the eastern to southeastern flank of the Nanambu Complex paleo-high. In any case, the topography of the unconformity may have been an important control on the geometry of fluid flow within diagenetic aquifers of the Kombolgie Subgroup.

As described above, we propose that a third and critical part of the ore-forming fluid flow system in the ARUF was the regional sub-unconformity alteration zone, previously interpreted to have formed during paleo-weathering (Needham, 1988; Miller et al., 1992). The sub-unconformity alteration is easily recognised in mineralogical and geochemical datasets: hematite–illite ± kaolinite ± diaspore alteration zones immediately beneath the unconformity to depths of up to 50 m are oxidised and depleted in Na, Sr, Pb, U, Ba and possibly Mg. Exploration vectoring within unconformity-related uranium hydrothermal systems may be possible utilising the spatial variations in the compositions of REE-bearing APS minerals in the sub-unconformity alteration zones and lower parts of the Kombolgie Subgroup (Beaufort et al., 2005; Gaboreau et al., 2005). These spatial relationships are also present in the Athabasca Basin (Gaboreau et al., 2007; Adlakha and

Hattori, 2015). Sub-unconformity alteration zones may be detectable in electrical and electromagnetic data. A regional airborne electromagnetic (AEM) survey of the eastern PCO and west Arnhem Land mapped a relatively thin conductive zone at the base of, or beneath, the Kombolgie Subgroup across large areas of the survey including parts of the ARUF (Craig, 2011). This conductivity feature may be due to a combination of sub-unconformity alteration minerals (e.g., clays) and fluids at the unconformity surface, according to Craig (2011). This is consistent with the relatively high electrical conductivities of weathered (i.e., clay-rich) rocks (Palacky, 1987), which the illite ± kaolinite-rich regional sub-unconformity alteration zone resemble mineralogically if not in origin.

9.2. Sources of uranium

Sources of uranium. Identification of uranium-depleted rocks in principle can provide a spatial guide to the source of uranium in an ore-forming mineral system, and hence yield insights on the 'fertility' of a region for uranium mineralisation. In practice it is generally difficult to genetically link such metal depleted zones with the ore deposits. There has been ongoing debate on the sources of uranium in unconformity-related deposits (Section 1), with both basin and basement sources proposed (Kyser and Cuney, 2009). The current study of the Ranger mineral system contributes to this debate by proposing that the basement-hosted sub-unconformity alteration zones were important sources of uranium. Regional alteration to depths of up to ~50 m beneath the unconformity in the ARUF (Needham, 1988; Miller et al., 1992) indicates that significant volumes of basement rocks in addition to fault zones had at least transiently elevated permeabilities (cf. Kyser and Cuney, 2009). Simple mass-balance calculations indicate that a volume of basement 50 m thick and measuring approximately 8 × 8 km could supply the uranium in the Ranger 1 deposit, assuming 5 ppm was removed and 100% efficiency in transport and deposition of this uranium to the deposit. This model does not rule out basinal rocks as additional sources of uranium but does imply that basement rocks with anomalously high uranium contents are a favourable component in fertile unconformity-related uranium ore-forming mineral systems. We suggest that a key factor in the formation of world-class uranium deposits in the ARUF as compared with other parts of the PCO may be the presence of paleo-topographic highs dominated by (formerly) uranium-rich Archean granitic gneisses or Paleoproterozoic Nimbuwah granites. Similar conclusions have been drawn by previous workers although for different reasons that generally involve the granitic rocks as sources of uranium-rich sedimentary detritus (e.g., Hollis et al., 2009) rather than as a direct source of uranium from leached sub-unconformity alteration zones as proposed herein.

9.3. Drivers of fluid flow, and timing of uranium mineralisation

Fluids in unconformity-related uranium mineral systems of the ARUF including the Ranger system were driven through the Kombolgie Subgroup and into the underlying basement at the sites of mineralisation, according to most previous models. We would add the sub-unconformity alteration zones to the fluid flow systems. Identification of the energy sources driving paleo-fluid flow is problematic, and is critically dependant on an understanding of the timing of uranium mineralisation in relation to regional, sedimentary, diagenetic, thermal and tectonic events. As argued above, uranium mineralisation at the Ranger 1 deposit and elsewhere in the ARUF most likely formed between ~1720 Ma and ~1680 Ma. This proposal is consistent with the ~1710 Ma paleomagnetic age for disseminated hematite in the Kombolgie Subgroup, the oldest magnetisation event recognised in this unit (Giddings and Idnurm, 1993). The McArthur Basin was affected by the Mid-Tawallah Compression event at 1755–1730 Ma (Bull and Rogers, 1996; Jackson et al., 2000), followed by sedimentation and bimodal magmatism of the Calvert Superbasin, and development of northwest trending trans-tensional fault systems, commencing at ~1730 Ma (Jackson et al., 2000; Scott et al., 2000). Igneous activity including volcanism over ~20–30 m.y. is likely to have resulted in elevated geothermal gradients capable of driving convective hydrothermal systems where the permeability structure was favourable. Convection involving basin and substantial volumes of basement requires differences in permeability of less than ~2 orders of magnitude, a condition likely to have occurred in the McArthur Basin after diagenesis reduced the permeability of some basin rocks (Oliver et al., 2006). In the ARUF we suggest that convection across the basin-basement boundary would have been enhanced as diagenesis proceeded in the McArthur Basin and convecting fluids migrated downwards along cross-stratal faults and laterally within diagenetic aquifers, the unconformity, and the sub-unconformity alteration zone. Modelling of sub-seafloor mid-ocean ridge hydrothermal systems demonstrates that penetration of fluids into seafloor rocks is enhanced when seawater is heated due to decreased fluid densities, to the extent that at 200°C the decrease in density compared to cold water is equivalent to an increase in permeability of one order of magnitude (Weis, 2014). It is plausible that this effect is also a trigger in unconformity-related uranium systems for effective penetration of basinal fluids into basement rocks and consequent leaching of uranium, potentially to deep levels through the utilisation of fault networks. Such phenomena of deep percolation of basinal brines (>-several hundreds of metres to kilometres) into underlying basement rock have been widely observed and described worldwide for a variety of metals and geological settings (e.g., Cathelineau and Boiron (2009); Mercadier et al., 2010; Bons et al. 2014). Interestingly, Oliver et al. (2006) predict fluid mixing zones beneath the major unconformity in their model when convection is interrupted by extensional deformation events and basement-reacted fluids are drawn into fault dilational zones. As proposed above, the major uranium ore-forming events in the ARUF potentially are the result of interruption of regional convective hydrothermal systems during extensional or strike-slip tectonism. Conversely, the numerical modelling shows that compressional deformation leads to generalised fluid upflow (Oliver et al., 2006; Cui et al., 2012). Silicification at the Ranger 1 deposit, and chloritisation and quartz veining observed within the Kombolgie Subgroup (e.g., Gustafson and Curtis, 1983; Polito et al., 2005; Derome et al., 2007), all may be the result of fluid upflow either during convection or during tectonic compression (Polito et al., 2005). We prefer the former explanation on account of the regional extensional and strike-slip kinematics that appear to have existed during the period ~1720–1680 Ma (Jackson et al., 2000; Scott et al., 2000). Moreover, coupled fluid flow and chemical modelling by Raffensperger and Garven (1995) showed that convective systems could result in both distal sub-unconformity alteration zones with hematite + white mica + chlorite in downflow/lateral flow zones close to the unconformity, and chloritisation of basin rocks in upflow/outflow zones. The numerical model prediction of regional sub-unconformity alteration supports our contention of the importance of such regional alteration in unconformity-related uranium systems of the ARUF.

If thermally-driven convection and extensional deformation were the principal drivers of fluid flow in the formation of unconformity-related uranium mineralisation in the ARUF, the identification of causative igneous bodies and basin-controlling extensional faults (active at ~1725–1705 Ma) may assist in regional exploration and area selection. The Oenpelli Dolerite and West Branch Volcanics, for example, may be symptoms of the thermal drivers of fluid flow with the major uranium deposits situated within the 'footprints' of these igneous suites.

9.4. Ore depositional processes and physico-chemical gradients

Uranium deposition in unconformity-related deposits is conventionally interpreted to have occurred via the reduction of U^{6+} dissolved in oxidised fluids to U^{4+} in minerals such as uraninite (UO_2) or coffinite ($USiO_4$) (Kyser and Cuney, 2009; Bastrakov et al., 2010). Proposed reducing agents in unconformity-related uranium deposits include: graphite, Fe^{2+}-bearing minerals such as Fe-chlorite and pyrite, and

mobile reductants such as CH_4. At the Ranger 1 deposit graphite and Fe-bearing minerals including chlorite, biotite, amphibole and pyrite are all present in the host rocks and may have contributed as local reductants. Although lack of graphite in some ore zones in the ARUF has been attributed to oxidation by ore fluids (e.g., Nabarlek, Wilde and Wall, 1987; Polito et al., 2004), graphite appears to have been preserved within ore zones at Ranger (Fisher et al., 2013; this study), suggesting it may not have been an efficient reductant (Kyser and Cuney, 2009). The D1 shear zones at Ranger 1 orebody 3 were initially biotite–amphibole bearing and then veined by amphibole-bearing veins prior to retrograde alteration to Fe-chlorite and white mica ± pyrite at ~1800 Ma (Mercadier et al., 2013b). These D1/D2 shear zones were also invaded by olivine–phyric dolerite dykes (Oenpelli Dolerite). This chemical architecture of a graphitic shear zone rich in Fe^{2+}-bearing minerals may have been favourable for later localisation of uranium mineralisation. Shear zones occupied by mafic dykes may be recognisable in geophysical datasets as subtle gravity anomalies. Dykes of Oenpelli Dolerite may also mark extensional fault structures which were favourable for fluid flow. Another mobile reductant, hydrogen, has been recently proposed for the reduction of uranium in the context of unconformity-related U deposits (Dargent et al., 2015). The hydrothermal alteration of Fe(II)-bearing minerals may result in H_2 production, which is a widespread process in subseafloor alteration zones. This process also may occur in unconformity-related uranium deposit settings where Fe(II)-bearing minerals are destroyed within intensely altered zones. The authors experimentally tested the potential of CH_4, C-graphite, dissolved Fe(II) and H_2 for the precipitation of uraninite from U-rich acidic chloride brines, in conditions similar to those determined in natural deposits. Their results demonstrate that the gaseous reductants (H_2, CH_4), as mobile electron donors, are the most efficient reducing agents in such deposits and may explain the large volume and high concentrations of uranium encountered in these deposits.

Deposition of U2 uraninite during the Proterozoic appears to have been intimately associated with precipitation of disordered carbon at the Ranger deposit. This process may have involved a mobile reduced-carbon reductant mixing with an oxidised uranium-bearing fluid within the previously-formed Ranger deposit, or alternatively the deposition of one then the other mineral. The significance of this style of uranium mineralisation and of the disordered carbon is yet to be understood in detail.

10. Summary and conclusions

New results of this study of the Ranger 1 unconformity-related uranium deposit and its ore-forming mineral system together with a synthesis of previous work provide the basis for the following proposed sequence of tectonothermal and hydrothermal events.

(1) D1 shear zones developed at medium grade metamorphic conditions, subparallel to compositional layering and at the contact between the Paleoproterozoic Cahill Formation metasedimentary sequence and underlying Archean granitic gneisses of the Nanambu Complex. These shear zones were fundamental to the localisation of later uranium mineralisation, during reactivation events.

(2) Pegmatite dykes were emplaced late within, and post-dating, the intense D1 shearing. Ion microprobe dating of igneous zircons in weakly foliated and massive pegmatite dykes at the Ranger 1 Number 3 orebody yielded U–Pb ages of 1867.0 ± 3.5 Ma and 1862.8 ± 3.4 Ma, respectively. We interpret both the shearing and pegmatites to be part of the regional Nimbuwah event and propose that this tectonothermal event terminated by ~1863 Ma in the Ranger area at least, rather than by ~1847 Ma as previously suggested (e.g., Worden et al., 2008). This prior constraint was based on a monazite U–Pb age of 1847 ± 1 Ma from a pegmatite at the Ranger deposit (Annesley et al., 2002), which we suggest correlates with event (3), a hydrothermal rather than pegmatite emplacement event.

(3) Amphibole–plagioclase–titanite–apatite veining occurred within the D1 shear zone at 1845.4 ± 4.2 Ma, as constrained by ion microprobe U–Pb dating of titanite. This represents a previously unrecognised, relatively high temperature, hydrothermal event in the ARUF. The veins were subsequently intensely altered to massive chlorite and titanium oxides, a common although volumetrically minor feature in the Ranger 1 deposit.

(4) Reactivation of D1 shear zones occurred at ~1800 Ma during the regional Shoobridge event. This deformation occurred at low grade metamorphic conditions and resulted in chlorite–sericite–monazite hydrothermal alteration of peak metamorphic biotite–amphibole-bearing mineral assemblages at the Ranger deposit. Uranium-lead ion microprobe dating of this hydrothermal monazite by Mercadier et al. (2013b) yielded an age of 1800 ± 9 Ma which was proposed to represent an early stage of the Shoobridge event. Uplift and erosion were likely consequences of the Shoobridge event.

(5) New ion microprobe U–Pb analyses of uraninite U1 samples yielded a discordia with an upper intercept age of 1688 ± 46 Ma with a high MSWD value due to lead loss. The oldest EPMA chemical age determined for U1 uraninite in this study of the Ranger 1 deposit is ~1646 Ma. This ion probe determination agrees with previously determined oldest ages of uraninite in the ARUF (U–Pb, ^{207}Pb–^{206}Pb and EPMA chemical ages up to ~1690 Ma; Polito et al., 2004, 2005, 2011).

(6) Unconformity-related uranium mineralisation at the Ranger 1 (Number 3 orebody) initially formed after the Oenpelli Dolerite, based on new observations and geochemical data that confirm the inferences of Hein (2002). The main uranium mineralisation event at the Ranger 1 deposit and elsewhere in the ARUF is inferred to have occurred between ~1720 Ma and ~1680 Ma, just overlapping with the U–Pb age of 1737 ± 20 Ma reported by Ludwig et al. (1987) for uraninite-rich samples from the Ranger 1 deposit.

(7) We suggest that the previously described 'paleoregolith' zone in the basement is a sub-unconformity regional alteration zone, and constituted an important part of the fluid flow system and rock volume from which uranium was leached to form the unconformity-related deposits in the ARUF.

(8) A multi-stage model is proposed for uranium deposits of the ARUF in which McArthur Basin-derived, oxidised, diagenetic brines penetrated uranium-rich Archean and other basement rocks over wide areas and leached uranium, transporting it laterally through the sub-unconformity alteration zone and downwards via fault networks, within a regional convective hydrothermal system driven by regional magmatism. Upflow zones were characterised by silicification at the Ranger 1 deposit and possibly elsewhere. Changes in tectonics are suggested to have caused reversals of fluid flow so that silicified zones were overprinted by the main ore stage of uraninite mineralisation, chloritisation and brecciation.

(9) Two other younger uranium mineralisation events were dated at 1421 ± 68 Ma ($^{206}Pb/^{238}U$-$^{207}Pb/^{235}U$ upper intercept age) and at 474 ± 6 Ma ($^{206}Pb/^{238}U$-$^{207}Pb/^{235}U$ upper intercept age). Uraninite of similar age to the former was previously known but the paragenetic association between the uraninite U2, hydrothermal disordered carbon and quartz had not been recognised. The younger uraninite U3 represents the first identification of uranium mineralisation of lower Paleozoic age in the Pine Creek Orogen, and raises the possibility of uranium remobilisation into younger rocks than previously considered prospective.

Acknowledgements

Sampling at the Ranger 1 deposit was undertaken with support and permission of Energy Resources Australia, with assistance from Andrew Wygralak of the Northern Territory Geological Survey and by Andy

Browne, all of whom are gratefully acknowledged. Laboratory staff at Geoscience Australia are thanked for preparation of zircon mineral separates for SHRIMP dating. We thank Chris Carson for SHRIMP analysis of the two pegmatite zircon samples. The assistance of David Di Bugnara (SEM analysis), Terry Mernagh (laser Raman analysis of carbonaceous matter), and Bill Pappas (whole-rock geochemical analysis) at Geoscience Australia is greatly appreciated. David Champion (Geoscience Australia) helped compile geochemical data for Fig. 15 and in the completion of whole-rock geochemical data in Table 3. Olivier Rouer and Sandrine Mathieu from the GeoRessources Laboratory at the University de Lorraine (Nancy, France) provided valuable assistance in analysing uraninite by EPMA and SEM. Reviewers Kim Hein, Andy Wilde and an anonymous reviewer, along with two reviewers from Geoscience Australia, are thanked for valuable comments on the manuscript which led to significant improvements. Published with permission of the Chief Executive Officer, Geoscience Australia.

Appendix A Analytical methods

A.1. SHRIMP ion microprobe U–Pb dating — zircon

Uranium-lead isotopic analyses of the zircons for pegmatite samples 2000646 and 2000649 were conducted on the Sensitive High-Resolution Ion Microprobe (SHRIMP) 2e ion microprobe at Geoscience Australia over a single analytical session during 28–31 January 2010 (Appendix Tables 1, 2). Ionized oxygen is accelerated through a potential of 10 kV, O^- ions are selected via Wein filtering, focused and directed at a Kohler aperture of 100 μm resulting in an ion beam at the target zircon of ca. 20 μm diameter. A beam current of ca. 2–3 nA was routinely achieved. The operating mass resolution (measured at mass ^{208}Pb on Broken Hill Pb–feldspar), was greater than 4700 (M/□M) at 1% peak height. Ten elemental and molecular species were analyzed, in increasing mass order (with typical count-times): $^{196}Zr_2O$ (2 s); ^{204}Pb (20 s); background (+0.05 amu from ^{204}Pb; 20 s); ^{206}Pb (15 s); ^{207}Pb (40 s); ^{208}Pb (5 s); ^{238}U (5 s); ^{248}ThO (2 s); ^{254}UO (2 s) and $^{270}UO_2$ (2 s). Six scans were conducted through these mass stations for each spot analysis. Subsequent data reduction was performed via SQUID v1.10 and ISOPLOT v3.0 (Excel macros; Ludwig, 2001, 2003). Discrimination of $^{206}Pb/^{238}U$ was assessed using Temora-2 (Black et al., 2004), with U–Pb calibration protocols following that described by, for example, Claoué-Long et al. (1995); Stern (1997) and Williams (1998) and assume a power law relationship for analyses such that $Pb^+/U^+ = A\bullet(UO^+/U^+)^B$ where A is the session calibration constant (Appendix Tables 1, 2) for the standard and B is assumed to be 2. Unknowns were analysed concurrently and were assumed to obey the same power law function as the U–Pb standard. Corrections for the common Pb content (indicated by asterisk) of analyzed zircons were based on measured ^{204}Pb and assuming contemporary values for common Pb derived from Stacey and Kramers (1975). No corrections for ^{204}Pb over- or undercounting were applied (Appendix Tables 1, 2; Black, 2005). CZ3 is used as a U concentration standard and analyzed at the start of the session. All age uncertainties, including the figures, quoted in the text are at the 2 sigma level unless otherwise stated. All uncertainties in the data tables are quoted at the 1-sigma level unless otherwise stated. $^{207}Pb^*/^{206}Pb^*$ and $^{206}Pb^*/^{238}U$ ages are considered discordant if the difference between them exceeds ±5%.

A.2. SHRIMP ion microprobe U–Pb dating — titanite

Following petrographic examination and characterisation of the titanites, the thin section was cut to fit a "mega" (35 mm diameter) mount and was mounted onto double-sided tape together with grains of the titanite standard BLR-1 and cast into epoxy. The thin section and the standards were polished to a smooth, common surface with 2 μm and then 1 μm diamond paste. The whole mount was photographed to compile a merged map of the section and standards and transmitted and reflected microphotographic pairs were taken of the target titanites and the standards. Backscatter SEM images of the Ranger titanites were also taken prior to analysis.

The U–Pb analyses were made using the SHRIMP II ion microprobe at the Research School of Earth Sciences (RSES), The Australian National University (Appendix Table 3). The standard analytical protocols described by Williams (1998) were used. A mass-filtered primary O_2^- beam was focussed onto the titanites producing a spot size appropriate for the target — in the case of the current sample, this was ~25 μm in diameter. The surface was cleaned of any contamination by rastering the primary beam across the target spot for 2.5 min before analysis. Data acquisition was done by repeatedly stepping through the masses $^{40}CaTi_2^{16}O_4$ ("reference mass 200"), ^{204}Pb, background at mass 204.04, ^{206}Pb, ^{207}Pb, ^{208}Pb, ^{238}U, ^{232}Th and $^{238}U^{16}O$ (mass 254), for 6 scans.

The data were reduced in a manner similar to that described by Williams (1998, and references therein), using the SQUID I Excel Macro of Ludwig (2001). The reference titanite BLR-1 (1050.5 ± 0.9 Ma, 2 s; Aleinikoff et al., 2007) was the U–Pb geochronology calibration standard and the reference used to calibrate U/Th and Pb concentrations for the session (U concentration: 250 ppm; Aleinikoff et al., 2007). The decay constants recommended by the IUGS Subcommission on Geochronology (as given in Steiger and Jäger, 1977) were used in the age calculations.

Uncertainties given for individual U–Pb analyses (ratios and ages) are at the 1 sigma level, however uncertainties in the calculated weighted mean ages are reported as 95% confidence limits and include the uncertainties in the standard calibrations where appropriate. For the age calculations, corrections for common Pb were made using the measured ^{204}Pb and the relevant common Pb compositions from the Stacey and Kramers (1975) model. Concordia plots, regressions and any weighted mean age calculations were carried out using Isoplot/Ex 3.0 (Ludwig, 2003) and where relevant include the error in the standard calibration.

A.3. Cameca ion microprobe U–Pb dating — uraninite

U–Pb isotopic compositions of uranium oxides were determined using a CAMECA IMS1270 ion microprobe (CRPG-CNRS, Nancy; Appendix Table 4). The O_2^- primary ion beam was accelerated at 13 kV, with an intensity ranging between 5 and 10 nA. The aperture illumination mode (Kohler illumination) was used with a 100-μm mass aperture, the size of the spot on the uranium oxides was ~12 μm. Positive secondary ions were extracted with a 10 kV potential, and the spectrometer slits were set for a mass resolving power of ~5500 to separate isobaric interferences of rare earth element (REE) dioxides from Pb. The field aperture was set to 3000 μm, and the transfer optic magnification was adjusted to 300. Rectangular lenses were activated in the secondary ion optics to increase the transmission at high mass resolution. The energy window was opened at 30 eV, and its low energy side was positioned at 5 eV before the start of the energy distribution. A single collector was used in ion-counting mode and the spectrum scanned by peak jumping. Each analysis consisted of 8 successive cycles. Each cycle began with measurement of the mass 203.5 for background, followed by ^{204}Pb, ^{206}Pb, ^{207}Pb, ^{208}Pb, ^{238}U, ^{248}ThO, and ^{238}UO, with measurement times of 4, 10, 10, 30, 10, 4, 4, and 4 s, respectively (waiting time of 1 s). The mass and energy calibrations were checked before each measurement, after a 2 min presputtering that was completed in rastering the primary beam over a 40 × 40 μm area to clean the gold coating and avoid pollution. Several spot analyses (at least five) were measured on the Zambia reference uraninite (concordant age of 540 ± 4 Ma; Cathelineau et al., 1990) before and after each sample

Appendix Table 1
SHRIMP U–Pb analyses of zircons, pegmatite sample 2000646.

Grain spot	% $^{206}Pb_c$	ppm U	ppm Th	$^{232}Th/^{238}U$	ppm $^{206}Pb^*$	(1) $^{206}Pb^*/^{238}U$ Age	±	(1) $^{207}Pb^*/^{206}Pb^*$ Age	±
646.19.1.1	0.08	283.2	122.4	0.44661	80.0674	1874.8	57.41	834.77	756.5
646.40.1.1	30.20	272.6	101.5	0.38454	148.587	2306.1	196.5	1870.9	863
646.43.1.1	14.40	214.7	109.7	0.52763	80.7447	2044	53.81	1779.4	300.5
646.22.1.1	12.98	154.6	151.8	1.01481	57.2683	2092.8	48.96	1820.7	201.2
646.28.1.1	8.63	256.4	205.7	0.82899	88.0999	2034.8	49.65	1810.2	189.4
646.17.1.1	2.95	315.1	168.6	0.55296	95.5473	1902.6	44.49	1808.8	201.1
646.9.1.1	3.20	177.4	70.27	0.40921	55.1349	1930.7	34.92	1849.1	39.68
646.38.1.1	0.20	273.6	195.1	0.73665	81.0208	1905	34.46	1864.4	9.389
646.8.1.1	2.18	166.3	78.4	0.48701	49.0998	1868.5	35.58	1833.7	40.25
646.34.1.1	4.99	344.6	184	0.55169	101.023	1812.7	40.54	1784.3	232.1
646.24.1.1	−0.02	207.2	97.53	0.48633	61.0068	1898.1	33.26	1873	8.529
646.1.1.1	2.87	278.7	148.2	0.54926	82.5973	1863	36.68	1837.3	57.76
646.23.1.1	0.16	224.2	113.9	0.52487	64.74	1868.8	33.91	1842.3	11.26
646.5.1.1	0.05	212.3	147.2	0.71627	62.5491	1897.4	36.08	1879.3	8.64
646.3.1.1	0.11	266.5	139.3	0.54032	78.1274	1889.9	33.02	1870.8	8.083
646.27.1.1	0.06	146.5	62.69	0.44203	42.5282	1875.9	33.21	1856.4	11.02
646.37.1.1	1.13	101.4	66.88	0.68142	29.6901	1875.1	35.6	1854.3	25.57
646.36.1.1	0.04	195.8	149.7	0.78998	57.2755	1890.6	38.88	1872.4	9.234
646.41.1.1	0.10	157.9	83.88	0.54884	45.7263	1873.4	33.52	1857.9	13
646.35.1.1	3.77	296.1	219.1	0.76463	91.4387	1907.8	41.84	1902.2	172.5
646.49.1.1	0.37	301.7	151.8	0.51982	87.9542	1874.8	33.73	1873.6	11.4
646.48.1.1	0.08	337.9	182.5	0.55807	97.4736	1863.5	35.43	1863.3	7.963
646.31.1.1	0.04	173.3	79.26	0.4726	50.1752	1873.2	33.06	1870.5	15
646.10.1.1	0.06	213.8	91.23	0.44088	61.6711	1864.7	32.47	1864.4	9.053
646.6.1.1	0.17	323.3	210.9	0.67423	93.2491	1864.8	33.21	1862.8	7.85
646.11.1.1	0.01	393.5	292.9	0.76912	112.57	1850.5	39.61	1856	12.3
646.30.1.1	0.38	216.9	110.1	0.5243	62.7141	1860.4	33.21	1867.8	11.41
646.39.1.1	0.41	318.8	148.6	0.48146	91.6737	1853	34.4	1858.9	10.31
646.14.1.1	0.03	331.1	131.5	0.41035	95.0261	1856.6	31.78	1862.5	6.823
646.21.1.1	0.08	167.2	123.5	0.76284	48.0953	1858.6	34.76	1867.1	11.33
646.42.1.1	0.05	224.6	114.8	0.52834	64.5815	1860	36.6	1869	8.782
646.13.1.1	−0.03	233.2	103.5	0.45853	66.964	1856.6	33.42	1871.8	8.256
646.2.1.1	0.02	518.1	276.2	0.55072	147.968	1849	31.95	1868.5	5.335
646.25.1.1	0.01	438.5	289.6	0.68256	125.842	1857.2	35.25	1880.4	5.922
646.26.1.1	0.16	131.9	65.27	0.5114	37.8338	1852.9	35.19	1878.4	13.21
646.20.1.1	18.33	213.8	215.5	1.04147	78.083	1970.5	76.26	1946.3	316.5
646.18.1.1	0.23	344.5	169.9	0.50976	96.6519	1817.5	31.6	1845.1	8.878
646.32.1.1	3.40	244.8	136.1	0.57467	70.3479	1809.3	33.6	1834	46.3
646.16.1.1	0.04	187	84.57	0.4674	52.8128	1834.2	32.17	1868.9	9.431
646.45.1.1	0.09	46.48	69.72	1.54985	17.9528	2398.9	52.95	2470.3	14.98
646.47.1.1	2.03	60.69	30.39	0.51748	24.6404	2457.9	46.78	2543.4	25.67
646.7.1.1	16.45	396.2	263.4	0.68698	129.048	1787.7	42.95	1874.3	192.9
646.12.1.1	10.52	260.5	148.3	0.58812	77.1634	1728.9	36.99	1847.4	145.7
646.15.1.1	1.44	288.7	127.4	0.45587	75.1455	1680	29.91	1825.7	19.54
646.29.1.1	0.49	279.5	231.9	0.85726	73.4973	1728.3	34.29	1859.1	11.52
646.4.1.1	0.57	183.8	126.5	0.71144	47.211	1674.2	31.73	1858.2	20.6
646.33.1.1	2.73	1172	494.8	0.43605	301.577	1629	116.1	1845.6	464.4
646.46.1.1	0.16	250.4	126.2	0.52052	50.3222	1338.1	43.96	1805.3	14.81
646.44.1.1	19.55	543.5	373	0.70918	122.394	1225.5	43.35	1975.9	492.3

for sample bracketing. To define the relative sensitivity factor for Pb and U used for samples, an empirical linear relationship was defined between UO^+/U^+ and Pb^+/U^+ from all the measurements performed on the reference mineral (Zambia) and unknown samples. The error on the calibration curve is reported in the error given for each analysis. To achieve good reproducibility, each analysis was preceded by automated centering of the sample spot image in the field aperture (Schuhmacher et al., 2004) and of the magnetic field values in scanning the ^{206}Pb peak. Correction for common lead was made by measuring the ^{204}Pb amount; the common lead composition was calculated at the $^{207}Pb/^{206}Pb$ measured age, using the Pb isotopic composition calculated from Stacey and Kramers (1975) model at the age of uranium oxide. However, the high $^{206}Pb/^{204}Pb$ ratio (>10,000) obtained for all analyses suggests that there is negligible common lead. Ages and error correlations were calculated using the ISOPLOT flowsheet of Ludwig (1999). Uncertainties in the ages are reported at the 2σ level.

A.4. Uraninite EPMA chemical analysis and dating

Electron microprobe analyses (EPMA) of uranium oxides were done using a CAMECA SX100 microprobe at SCMEM (GeoRessources, Nancy, France; Appendix Table 5). Analyses were performed at 20 kV and a beam current of 20 nA (Si, Ca, Y, Th, U, Pb) or 100 nA (Sc, Ti, Mn, Fe, Eu, Yb, P, V, Ni, Zr, Mo, Ce, Dy, W). The calibration used natural and synthetic oxides, silicates, metals and alloys (albite, andradite, YPO_4, ThO_2, UO_2, $PbCrO_4$, Sc, $MnTiO_3$, $EuRu_2Ge_2$, monazite, apatite, V, NiO, zircon, Mo, Ce_2S_3, Dy_2O_3, W). The following rays were used: Kα (Si, Ca, Sc, Ti, Mn, Fe, P, V, Ni), Lα (Y, Eu, Yb, Zr, Mo, Ce, Dy, W) and Mα (Th, U, Pb). Counting times were 10 s for Si, Ca, Y, Th, U and Pb, and 40 s for Sc, Ti, Mn, Fe, Eu, Yb, P, V, Ni, Zr, Mo, Ce, Dy and W. Spot size was ~4 μm.

Chemical ages for uranium oxides and whole-rock geochemistry were calculated using and iterative calculation from the following

% Discordant	(1) $^{207}Pb^*/^{206}Pb^*$	± %	(1) $^{207}Pb^*/^{235}U$	± %	(1) $^{206}Pb^*/^{238}U$	± %	err corr	rejected
−54.5	0.0669	36.3	3.0334	36.38	0.3288	2.335	0.06417133	X
−20.8	0.1144	47.85	6.9863	48.16	0.4428	5.504	0.11426962	X
−13.3	0.1088	16.48	5.62	16.68	0.3746	2.603	0.15601604	X
−11.4	0.1113	11.09	5.7575	11.32	0.3752	2.281	0.20151586	X
−9.85	0.1107	10.42	5.5756	10.72	0.3655	2.505	0.23371623	X
−4.74	0.1106	11.06	5.2219	11.34	0.3425	2.5	0.22041377	X
−4.44	0.1131	2.194	5.4576	2.92	0.3501	1.927	0.65985853	X
−2.17	0.114	0.52	5.4079	1.968	0.344	1.898	0.96442917	
−1.83	0.1121	2.222	5.1949	3.005	0.3361	2.023	0.6732103	X
−1.44	0.1091	12.73	4.8767	12.94	0.3242	2.277	0.1760046	X
−1.42	0.1146	0.473	5.4142	1.961	0.3428	1.903	0.9704799	
−1.36	0.1123	3.19	5.1884	3.802	0.335	2.069	0.54412752	X
−1.24	0.1126	0.622	5.2115	2.052	0.3356	1.955	0.95294197	
−1.1	0.115	0.479	5.4339	2.053	0.3428	1.996	0.97234636	
−1.07	0.1144	0.448	5.3787	1.934	0.3409	1.882	0.97278686	
−1	0.1135	0.61	5.2844	2.026	0.3376	1.932	0.95358976	
−0.93	0.1134	1.415	5.2666	2.439	0.3369	1.987	0.8145297	X
−0.83	0.1145	0.512	5.3736	2.207	0.3403	2.147	0.97271491	
−0.69	0.1136	0.72	5.2744	2.056	0.3367	1.926	0.9367805	
−0.66	0.1164	9.601	5.5527	9.852	0.3459	2.213	0.22462931	X
−0.22	0.1146	0.632	5.3426	2.034	0.3381	1.933	0.95047821	
−0.1	0.1139	0.441	5.2716	2.084	0.3355	2.037	0.97735209	
−0.06	0.1144	0.832	5.3141	2.092	0.3369	1.919	0.91760036	
−0.05	0.114	0.502	5.2749	1.962	0.3355	1.897	0.96679319	
−0.03	0.1139	0.435	5.2642	1.922	0.3352	1.872	0.97408592	
0.179	0.1135	0.681	5.2099	2.325	0.333	2.223	0.95616045	
0.203	0.1142	0.632	5.2809	2.015	0.3353	1.913	0.94952636	
0.234	0.1137	0.571	5.2245	2.082	0.3333	2.003	0.9617301	
0.275	0.1139	0.378	5.2442	1.91	0.3339	1.872	0.98023088	
0.361	0.1142	0.628	5.267	2.039	0.3345	1.94	0.95139283	
0.451	0.1143	0.487	5.2732	2.174	0.3346	2.119	0.97461758	
0.68	0.1145	0.458	5.2769	2.008	0.3343	1.955	0.97366509	
1.012	0.1143	0.296	5.2366	1.878	0.3323	1.855	0.9875312	
1.202	0.115	0.329	5.2982	2.03	0.3341	2.003	0.98680036	
1.269	0.1149	0.733	5.2824	2.172	0.3334	2.045	0.94131861	
1.285	0.1193	17.71	5.7139	18.05	0.3473	3.511	0.19448275	X
1.477	0.1128	0.491	5.0681	1.931	0.3258	1.868	0.96717287	
1.601	0.1121	2.556	4.9953	3.191	0.3231	1.91	0.59873855	X
2.018	0.1143	0.523	5.1801	1.974	0.3287	1.904	0.96431445	
3.288	0.1614	0.887	9.9961	2.351	0.4492	2.177	0.92602081	X
3.689	0.1686	1.531	10.761	2.624	0.463	2.131	0.81211895	X
5.649	0.1146	10.7	5.0079	10.95	0.3168	2.351	0.21465824	X
6.571	0.1129	8.056	4.8049	8.331	0.3085	2.124	0.25490959	X
8.392	0.1116	1.077	4.5946	2.164	0.2986	1.877	0.86723701	X
8.469	0.1137	0.638	4.7741	2.13	0.3046	2.032	0.95414913	X
10.74	0.1136	1.14	4.6577	2.234	0.2973	1.921	0.85999984	X
12.01	0.1128	25.67	4.5309	26.68	0.2912	7.278	0.27280572	X
33.44	0.1104	0.814	3.5532	3.444	0.2335	3.346	0.97163689	X
60.17	0.1213	27.63	3.528	27.87	0.2109	3.633	0.13032711	X

equation of Bowles (1990) modified by Kister (2003):

$$Pb = Th * \frac{208}{232} * \left(e^{\lambda_{232} t} - 1\right) + U * \left(206 * \frac{0.9928}{238.04} * \left(e^{\lambda_{238} t} - 1\right) + 207 * \frac{0.0072}{235} * \left(e^{\lambda_{235} t} - 1\right)\right)$$

where t is the age of U deposition, λ_{232}, λ_{235} and λ_{238} are the decay constants of ^{232}Th ^{235}U and ^{238}U, respectively, and Pb, Th and U are the weight percent of these elements in the analyzed uranium oxides. The formula is based on the assumption that no U or Th have been re-introduced into or lost from the system and that no common lead was integrated during the crystallization.

A.5. Whole-rock geochemical analysis

Abundances of major and trace elements were determined at Geoscience Australia, Canberra (XRF & ICP-MS). Major and minor elements (Si, Ti, Al, Fe, Mn, Mg, Ca, Na, K, P & S) were determined by wavelength-dispersive XRF on fused disks using methods similar to those of Norrish and Hutton (1969). Precision for these elements is better than ±1% of the reported values. As, Cl, Co, Cr, Cu, F, Ni, Sc, V, and Zn were determined by pressed pellet on a wavelength-dispersive XRF using methods similar to those described by Norrish and Chappell (1977). Selected trace elements (Ba, Be, Bi, Cs, Ga, Ge, Hf, Mo, Nb, Pb, Rb, Sb, Sn, Sr, Ta, Th, U, W, Y, Zr) and the Rare Earth elements were analysed at Geoscience Australia by ICP-MS (Agilent 7500 with reaction cell) using methods similar to those of Eggins et al. (1997), but on solutions obtained by dissolution of fused glass disks (Pyke, 2000). Precisions are ±5% and ±10% at low levels (<20 ppm). Agreement between XRF and ICP-MS are within 10%. Loss on Ignition (LOI) was by gravimetry after combustion at 1100°C. FeO abundances were determined at Geoscience Australia by digestion and electrochemical titration using a modified methodology based on Shapiro and Brannock (1962).

Appendix Table 2
SHRIMP U–Pb analyses of zircons, pegmatite sample 2000649.

Grain spot	% $^{206}Pb_c$	ppm U	ppm Th	$^{232}Th/^{238}U$	ppm $^{206}Pb^*$	(1) $^{206}Pb^*/^{238}U$ Age	±	(1) $^{207}Pb^*/^{206}Pb^*$ Age	±
649.8.1.1	−0.02486	304	157.21	0.53494	86.4275	1845.3	32.49	1878.8	6.84
649.12.1.1	−0.01652	187	82.011	0.4532	52.6386	1827.7	32.27	1864.8	9.55
649.35.1.1	−0.00538	267	147.55	0.57126	76.0557	1847.8	32.62	1875.3	7.93
649.4.1.1	−0.00189	302	147.57	0.50461	84.6576	1818.9	31.61	1868.9	6.77
649.25.1.1	−0.00053	406	249.27	0.63508	120.145	1909.8	33.71	1847.3	5.7
649.24.1.1	0.01064	118	54.422	0.47674	34.4079	1882.5	34.73	1875.8	11
649.9.1.1	0.01271	343	244.64	0.73651	97.8536	1846.3	32.94	1862.6	6.47
649.7.1.1	0.01881	189	116.46	0.63672	52.714	1815	39.75	1860.6	14.2
649.11.1.1	0.02458	194	99.36	0.52903	54.078	1811.2	32.26	1855.1	8.74
649.13.1.1	0.03039	3748	13.522	0.00373	1093.93	1884.6	31.38	1855.6	20.5
649.45.1.1	0.03125	154	47.016	0.31456	44.7568	1873	37.89	1878.7	12.4
649.29.1.1	0.03849	253	189.23	0.77354	73.1645	1869.7	34.07	1864	8.51
649.43.1.1	0.04489	200	103.27	0.53325	54.9014	1786.2	34.31	1874.8	15.1
649.40.1.1	0.05118	258	141.59	0.56607	72.2991	1820.6	32.17	1848.9	8.94
649.26.1.1	0.06969	177	114.05	0.66482	50.2017	1836.5	33.1	1857.5	9.6
649.32.1.1	0.08099	155	87.651	0.5837	44.4361	1854.7	33.6	1872.5	11.9
649.28.1.1	0.08588	125	65.713	0.54274	35.8717	1855.1	35.96	1847.4	13.4
649.42.1.1	0.08665	292	126.48	0.44777	82.1298	1827.2	36.26	1862	8.71
649.37.1.1	0.08698	192	94.719	0.50855	53.9001	1811.1	32.29	1857.9	11.3
649.23.1.1	0.0969	203	90.258	0.45922	58.2381	1854.1	34.34	1864.7	11.2
649.22.1.1	0.10466	270	121.74	0.46537	76.2463	1828.8	31.71	1856.2	8.38
649.33.1.1	0.10578	231	101.01	0.45194	64.5633	1812.9	32.5	1858.5	10.2
649.18.1.1	0.15145	250	205.58	0.84905	70.0727	1813.6	33.36	1872.1	8.76
649.44.1.1	0.20282	176	72.175	0.42373	48.3379	1789.9	35.63	1859.7	17.7
649.34.1.1	0.22113	415	291.77	0.72629	116.534	1839.8	32.6	1855.9	8.69
649.3.1.1	0.2927	331	251.33	0.78489	86.1446	1694.8	32.1	1861.6	9.57
649.10.1.1	0.30426	222	117.45	0.54664	60.6091	1775.5	31.46	1867.9	13.1
649.41.1.1	0.31201	189	76.371	0.41692	48.2395	1662.1	29.94	1864.6	13.2
649.36.1.1	0.32734	236	143.97	0.63092	62.5565	1725.6	42.85	1849.6	14.7
649.17.1.1	0.34908	181	93.832	0.53672	45.7223	1656.5	29.98	1847.8	12.9
649.21.1.1	0.3497	374	269.05	0.74272	104.827	1812.7	32.5	1853.6	8.54
649.30.1.1	0.39274	285	152.19	0.55192	80.8821	1835.3	32.45	1860.9	11.5
649.19.1.1	0.42686	177	67.804	0.3959	41.4114	1535.6	28.66	1866.2	13.7
649.2.1.1	0.46111	308	154.83	0.51959	86.2033	1813.2	31.68	1872	11.2
649.39.1.1	0.50458	300	71.249	0.24503	76.6948	1673.1	29.14	1860	11.8
649.14.1.1	0.50865	381	213.06	0.57733	99.0084	1688.9	30.05	1860.9	12.3
649.38.1.1	0.52132	378	125.17	0.34246	98.5161	1701.1	30.15	1812.7	18.4
649.15.1.1	0.60886	299	135.39	0.46733	78.2759	1697.3	30.83	1866.7	14.2
649.16.1.1	0.62858	274	139.67	0.526	64.4484	1535	28.32	1853	15.9
649.31.1.1	0.71848	343	228.61	0.68867	98.8069	1850.2	33.24	1871.4	12.3
649.27.1.1	0.90169	383	217.5	0.58693	84.731	1445.9	29.77	1866.8	17.4
649.1.1.1	0.91161	197	90.844	0.47664	55.8188	1822.7	32.7	1874	30
649.20.1.1	2.00862	573	221.41	0.39929	131.704	1481.4	31.95	1869.6	48.9
649.6.1.1	2.64637	417	177.87	0.44028	79.4793	1234.3	38.37	1855.2	31.1
649.5.1.1	3.72615	495	312.19	0.65117	61.3927	861.82	17.88	1823.5	47

References

Adlakha, E.E., Hattori, K., 2015. Compositional variation and timing of aluminum phosphate-sulfate minerals in the basement rocks along the P2 fault and in association with the McArthur River uranium deposit, Athabasca Basin, Saskatchewan, Canada. Am. Mineral. 100 (7), 1386–1399.

Ahmad, M. and Munson, T.J. (compilers) 2013. Geology and mineral resources of the Northern Territory. Northern Territory Geological Survey Special Publication 5.

Aleinikoff, J.N., Witsch, R.P., Tollo, R.P., Unruh, D.H., Fanning, C.M., Schmitz, M.D., 2007. Ages and origins of the Killingworth Dome, south-central Connecticut: implications for the tectonic evolution of southern New England. Am. J. Sci. 307, 63–118.

Alexandre, P., Kyser, T.K., 2005. Effects of cationic substitutions and alteration in uraninite, and implications for the dating of uranium deposits. Can. Mineral. 43 (3), 1005–1017.

Annesley, I.R., Madore, C., Kwok, Y.Y., Kamo, S.L., Troy, A., Hughes, L., 2002. U–Pb geochronology and petrochemistry of late Barramundi pegmatites from the Ranger U deposit, Northern Territory, Australia. Uranium deposits. International workshop, Prague, September 2002, pp. 37–40.

Bastrakov, E., Jaireth, S., Mernagh, T.P., 2010. Solubility of uranium in hydrothermal fluids at 25° to 300°C. Geoscience Australia Record 2010/29.

Beaufort, D., Patrier, P., Laverret, E., 2005. Clay alteration associated with Proterozoic unconformity-type uranium deposits in the east Alligator Rivers Uranium Field, Northern Territory, Australia. Econ. Geol. 100, 515–536.

Binns, R.A., Ayres, D.E., Wilmshurst, J.R., Ramsden, A.R., 1980. Petrology and Geochemistry of Alteration Associated with Uranium Mineralization at Jabiluka, Northern Territory, Australia. In: Ferguson, J., Gobely, A.B. (Eds.), Uranium in the Pine Creek Geosyncline. International Atomic Energy Agency, Vienna, pp. 417–438.

Black, L.P., 2005. The use of multiple reference samples for the monitoring of ion microprobe performance during zircon 207Pb/206Pb age determinations. Geostand. Geoanal. Res. 29 (2), 169–182.

Black, L.P., Kamo, S.L., Allen, C.M., Davis, D.W., Aleinikoff, J.N., Valley, J.W., Mundil, R., Campbell, I.H., Korsch, R.J., Williams, I.S., Foudoulis, C., 2004. Improved $^{206}Pb/^{238}U$ microprobe geochronology by the monitoring of a trace-element-related matrix effect; SHRIMP, ID–TIMS, ELA–ICP–MS and oxygen isotope documentation for a series of zircon standards. Chem. Geol. 205 (1), 115–140.

Bons, P.D., Fusswinkel, T., Gomez-Rivas, E., Markl, G., Wagner, T., Walter, B., 2014. Fluid mixing from below in unconformity-related hydrothermal ore deposits. Geology 42 (12), 1035–1038.

Bowles, J.F.W., 1990. Age dating of individual grains of uraninite in rocks from electron microprobe analyses. Chem. Geol. 83, 47–53.

Bull, S.W., Rogers, J.R., 1996. Recognition and significance of an early compressional deformation event in the Tawallah Group, McArthur Basin, NT. MIC'96: New developments in metallogenic research vol. 55, pp. 28–32.

Cabanis, B., Lecolle, M., 1989. The La/10-Y/15-Nb/8 diagram: a tool for distinguishing volcanic series and discovering crustal mixing and/or contamination: Comptes Rendus de l'Academie des Sciences, serie 2. Sci. Terre 309, 20.

Cathelineau, M., Boiron, M.C., Holliger, P., Poty, B., 1990. Metallogenesis of the French part of the Variscan orogen. Part II: time–space relationships between U, Au and SnW ore deposition and geodynamic events—mineralogical and U/Pb data. Tectonophysics 177, 59–79.

Cathelineau, M., Boiron, M.-C., 2009. Downward penetration and mixing of sedimentary brines and dilute hot waters at 5 km depth in the granite basement at Soultz-sous Forêts (Rhine Graben, France). CR Geosci. http://dx.doi.org/10.1016/j.crte.2009.08.010.

% Discordant	(1) $^{207}Pb^*/^{206}Pb^*$	± %	(1) $^{207}Pb^*/^{235}U$	± %	(1) $^{206}Pb^*/^{238}U$	± %	err corr	rejected
1.829	0.1149	0.379	5.2515	1.91	0.331	1.872	0.98	
2.044	0.114	0.529	5.1534	1.989	0.328	1.918	0.964	
1.543	0.1147	0.44	5.2467	1.942	0.332	1.891	0.974	
2.717	0.1143	0.375	5.1394	1.91	0.326	1.873	0.981	
−3.274	0.1129	0.315	5.3699	1.91	0.345	1.883	0.986	
−0.455	0.1147	0.613	5.3711	2.093	0.34	2.002	0.956	
0.827	0.1139	0.358	5.2114	1.9	0.332	1.866	0.982	
2.672	0.1138	0.785	5.0926	2.376	0.325	2.243	0.944	
2.457	0.1134	0.483	5.0718	1.972	0.324	1.912	0.969	
−1.556	0.1135	1.136	5.3134	2.229	0.34	1.918	0.86	
0.285	0.1149	0.689	5.3437	2.346	0.337	2.242	0.956	
−0.386	0.114	0.471	5.2936	1.956	0.337	1.898	0.971	
4.981	0.1147	0.838	5.0472	2.217	0.319	2.053	0.926	
1.795	0.113	0.495	5.0728	1.957	0.325	1.893	0.968	
1.187	0.1136	0.531	5.1593	1.976	0.329	1.903	0.963	
1.032	0.1145	0.662	5.2598	2.047	0.333	1.937	0.946	
−0.42	0.113	0.738	5.1934	2.208	0.333	2.081	0.942	
2.017	0.1139	0.483	5.138	2.211	0.327	2.158	0.976	
2.213	0.1136	0.626	5.1021	2.009	0.326	1.909	0.95	
0.512	0.114	0.623	5.2433	2.105	0.333	2.01	0.955	
1.504	0.1135	0.464	5.1328	1.935	0.328	1.878	0.971	
2.431	0.1136	0.564	5.0937	2.021	0.325	1.94	0.96	
3.054	0.1145	0.486	5.1393	1.943	0.326	1.882	0.968	
4.182	0.1137	0.979	5.0026	2.376	0.319	2.165	0.911	
2.015	0.1135	0.481	5.102	1.938	0.326	1.877	0.969	
9.37	0.1138	0.53	4.7431	1.997	0.302	1.925	0.964	X
5.283	0.1142	0.724	4.9903	2.024	0.317	1.89	0.934	
11.64	0.114	0.733	4.6497	2.056	0.296	1.921	0.934	X
6.916	0.1131	0.813	4.7998	2.719	0.308	2.595	0.954	X
11.35	0.113	0.715	4.5733	2.035	0.294	1.905	0.936	X
2.217	0.1133	0.472	5.0764	1.922	0.325	1.863	0.969	
1.459	0.1138	0.635	5.1643	1.994	0.329	1.89	0.948	
20.63	0.1141	0.76	4.2682	2.105	0.271	1.963	0.933	X
3.361	0.1145	0.621	5.1212	1.973	0.324	1.873	0.949	
11.4	0.1137	0.653	4.6361	2.022	0.296	1.914	0.946	X
9.805	0.1138	0.682	4.7181	1.983	0.301	1.862	0.939	X
6.537	0.1108	1.016	4.6149	2.174	0.302	1.923	0.884	X
9.559	0.1142	0.786	4.7618	2.081	0.303	1.927	0.926	X
19.59	0.1133	0.877	4.2445	2.092	0.272	1.899	0.908	X
1.024	0.1145	0.683	5.2539	1.998	0.333	1.877	0.94	
27.38	0.1142	0.963	4.0181	2.277	0.255	2.064	0.906	X
2.771	0.1146	1.663	5.1667	2.542	0.327	1.923	0.756	
24.56	0.1143	2.713	4.1337	3.479	0.262	2.178	0.626	X
47.3	0.1134	1.721	3.3747	3.503	0.216	3.051	0.871	X
117.5	0.1115	2.591	2.1345	3.287	0.139	2.022	0.615	X

Chipley, D., Polito, P.A., Kyser, T.K., 2007. Measurement of U–Pb ages of uraninite and davidite by laser ablation-HR-ICP-MS. Am. Mineral. 92, 1925–1935.

Claoué-Long, J.C., Compston, W., Roberts, J., Fanning, C.M., Aubrey, M.-P., Hardenbol, J., 1995. In: Berggren, W.A., Kent, D.V. (Eds.), Geochronology Time Scales and Global Stratigraphic Correlation. SEPM (Society for Sedimentary Geology) Special Publication vol. 54, pp. 3–21.

Clauer, N., 2013. The K-Ar and $^{40}Ar/^{39}Ar$ methods revisited for dating fine-grained K-bearing clay minerals. Chem. Geol. 354, 163–185.

Cloutier, J., Kyser, K., Olivo, G.R., Alexandre, P., 2010. Contrasting patterns of alteration at the wheeler river area, Athabasca Basin, Saskatchewan, Canada: insights into the apparently uranium-barren zone K alteration system. Econ. Geol. 105 (2), 303–324.

Craig, M.A. (Ed.), 2011. Geological and energy implications of the Pine Creek region airborne electromagnetic (AEM) survey, Northern Territory, Australia. Geoscience Australia Record 2011/18 (292 pp.).

Craw, D., 2002. Geochemistry of late metamorphic hydrothermal alteration and graphitisation of host rock, Macraes gold mine, Otago schist, New Zealand. Chem. Geol. 191 (4), 257–275.

Cui, T., Yang, J., Samson, I.M., 2012. Tectonic deformation and fluid flow: implications for the formation of unconformity-related uranium deposits. Econ. Geol. 107 (1), 147–163.

Dargent, M., Truche, L., Dubessy, J., Bessaque, G., Marmier, H., 2015. Reduction kinetics of aqueous U (VI) in acidic chloride brines to uraninite by methane, hydrogen or C-graphite under hydrothermal conditions: Implications for the genesis of unconformity-related uranium ore deposits. Geochimica et Cosmochimica Acta 167, 11–26.

Derome, D., Cathelineau, M., Cuney, M., Fabre, C., Lhomme, T., Banks, D.A., 2005. Mixing of sodic and calcic brines and uranium deposition at McArthur River, Saskatchewan, Canada: a Raman and laser-induced breakdown spectroscopic study of fluid inclusions. Econ. Geol. 100 (8), 1529–1545.

Derome, D., Cathelineau, M., Fabre, C., Boiron, M.-C., Banks, D., Lhomme, T., Cuney, M., 2007. Paleo-fluid composition determined from individual fluid inclusions by Raman and LIBS: application to mid-Proterozoic evaporitic Na–Ca brines (Alligator Rivers Uranium Field, Northern Territories Australia). Chem. Geol. 237, 240–254.

Derome, D., Cuney, M., Cathelineau, M., Fabre, C., Dubessy, J., Bruneton, P., Hubert, A., 2003. A detailed fluid inclusion study in silicified breccias from the Kombolgie sandstones (Northern Territory, Australia): inferences for the genesis of middle-Proterozoic unconformity-type uranium deposits. J. Geochem. Explor. 80 (2), 259–275.

Donnelly, T.H., Ferguson, J., 1980. A Stable Isotope Study of Three Deposits in the Alligator Rivers Uranium Field, NT. In: Ferguson, J., Gobely, A.B. (Eds.), Uranium in the Pine Creek Geosyncline. International Atomic Energy Agency, Vienna, pp. 397–406.

Eggins, S.M., Woodhead, J.D., Kinsley, L.P.J., Mortimer, G.E., Sylvester, P., McCulloch, M.T., Hergt, J.M., Handler, M.R., 1997. A simple method for the precise determination of >40 trace elements in geological samples by ICPMS using enriched isotope internal standardisation. Chem. Geol. 134, 311–326.

Eupene, G.S., Fee, P.H., Colville, R.G., 1975. Ranger One Uranium Deposits. In: Knight, C.L. (Ed.), Economic Geology of Australia and Papua New Guinea Monograph 5. Australasian Institute of Mining and Metallurgy, pp. 308–317.

Ewers, G.R., Ferguson, J., 1980. Mineralogy of the Jabiluka, Ranger, Koongarra and Nabarlek Uranium Deposits. In: Ferguson, J., Gobely, A.B. (Eds.), Uranium in the Pine Creek Geosyncline. International Atomic Energy Agency, Vienna, pp. 363–374.

Fayek, M., Kyser, T.K., 1997. Characterisation of multiple fluid-flow events and rare-earth elements mobility associated with formation of unconformity-related uranium deposits in the Athabasca Basin,Saskatchewan. Can. Mineral. 35, 627–658.

Appendix Table 3
Summary of SHRIMP U–Pb titanite data for sample S3PD730 371.2 m, Ranger 1 No. 3 orebody.

Grain.Spot	% $206Pb_c$	ppm U	ppm Th	232Th/238U	ppm $206Pb^*$	(1) 206Pb/238U Age	(1) 207Pb/206Pb Age	% Dis-cor-dant	(1) $^{207}Pb^*/^{206}Pb^*$	±%	(1) $^{207}Pb^*/^{235}U$	±%	(1) $^{206}Pb^*/^{238}U$	±%	err corr
1.1	1.05	52	5	0.11	14.1	1745 ± 24	1847 ± 25	6	0.1129	1.4	4.84	2.1	0.3108	1.6	.758
1.2	0.16	216	86	0.41	54.9	1665 ± 18	1840.4 ± 6.8	10	0.11252	0.38	4.573	1.3	0.2948	1.2	.954
1.3	0.28	209	74	0.37	56.3	1758 ± 19	1850.1 ± 7.6	5	0.11312	0.42	4.888	1.3	0.3134	1.2	.946
1.4	1.80	41	4	0.10	11.1	1756 ± 28	1847 ± 34	5	0.1129	1.9	4.88	2.6	0.3132	1.8	.695
2.1	0.25	117	13	0.11	31.6	1753 ± 21	1852.2 ± 8.9	5	0.11325	0.49	4.878	1.4	0.3124	1.3	.940
2.2	0.44	77	36	0.49	20.5	1742 ± 22	1840 ± 13	5	0.11248	0.7	4.812	1.6	0.3103	1.5	.901
2.3	0.18	180	82	0.47	49.8	1794 ± 21	1838 ± 11	2	0.11236	0.59	4.972	1.5	0.321	1.4	.919
2.4	0.31	169	82	0.50	41.3	1609 ± 18	1843.7 ± 9.2	13	0.11272	0.51	4.406	1.4	0.2835	1.3	.930
3.1	0.23	212	73	0.36	56.8	1747 ± 18	1843.5 ± 6.5	5	0.11271	0.36	4.836	1.2	0.3112	1.2	.958
3.2	0.32	115	19	0.17	31.1	1756 ± 20	1843.8 ± 9.2	5	0.11273	0.51	4.868	1.4	0.3132	1.3	.933
3.2.2	7.02	39	14	0.37	7.69	1250 ± 28	1716 ± 150	27	0.1051	8.2	3.1	8.5	0.214	2.5	.290
3.3	0.35	111	24	0.23	29.3	1726 ± 20	1841 ± 11	6	0.11257	0.58	4.766	1.4	0.3071	1.3	.913
3.4	1.06	298	83	0.29	49.3	1124 ± 42	1732 ± 35	35	0.106	1.9	2.78	4.5	0.1904	4.1	.907
3.5	0.16	249	98	0.41	60.7	1610 ± 16	1852.4 ± 5.5	13	0.11326	0.31	4.43	1.2	0.2837	1.2	.967
3.6	0.20	205	32	0.16	55.5	1765 ± 18	1842.5 ± 6.5	4	0.11264	0.36	4.892	1.2	0.315	1.2	.958
5.1	0.42	70	11	0.17	18.4	1717 ± 23	1850 ± 13	7	0.11311	0.74	4.759	1.7	0.3051	1.5	.902
5.2	0.23	106	15	0.15	28.3	1735 ± 20	1842.4 ± 8.8	6	0.11264	0.49	4.797	1.4	0.3088	1.3	.940
5.3	0.24	181	24	0.14	48.6	1750 ± 21	1850 ± 12	5	0.11309	0.64	4.863	1.5	0.3119	1.4	.908
5.4	0.45	218	36	0.17	34.9	1097 ± 12	1824 ± 11	40	0.11153	0.59	2.851	1.3	0.1854	1.2	.895
6.1	0.43	92	18	0.21	25.6	1800 ± 22	1844 ± 12	2	0.11274	0.66	5.007	1.6	0.3221	1.4	.907

Errors are 1-sigma; Pb_c and Pb^* indicate the common and radiogenic portions, respectively.
Error in Standard calibration was 0.36% (not included in above errors but required when comparing data from different mounts).
(1) Common Pb corrected using measured ^{204}Pb.

Appendix Table 4
Cameca ion probe analyses of uraninite, drillhole samples S3PD759-408.0 m, S3PD1050 424.0 m and S3PD730 459.7 m.

Sample	SIMS raw ratio			Fractionation and common Pb corrected measured isotopic ratios								Age (Ma)					
spot	$^{207}Pb/^{206}Pb$	2σ	$^{204}Pb/^{206}Pb$	2σ	$^{207}Pb/^{235}U$	2σ	$^{206}Pb/^{238}U$	2σ	Correlation	$^{207}Pb/^{206}Pb$	2σ	$^{207}Pb/^{235}U$	2σ	$^{206}Pb/^{238}U$	2σ	$^{207}Pb/^{206}Pb$	2σ
759-408.8																	
2	0.1020	0.0005	3.58E-06	5.86E-07	2.7440	0.0734	0.1947	0.0051	0.9839	0.1022	0.0048	1340	20	1147	28	1665	9
3	0.0574	0.0007	1.54E-05	5.03E-06	0.2885	0.0098	0.0365	0.0011	0.9255	0.0573	0.0129	257	8	231	7	503	28
4	0.0944	0.0019	2.25E-05	7.13E-06	1.6118	0.1053	0.1239	0.0077	0.9515	0.0944	0.0201	975	40	753	44	1515	37
5	0.0941	0.0012	8.23E-06	1.41E-06	1.7655	0.0669	0.1359	0.0049	0.9462	0.0942	0.0123	1033	24	821	28	1513	23
7	0.1000	0.0005	1.59E-06	3.28E-07	2.6074	0.0668	0.1886	0.0047	0.9826	0.1003	0.0048	1303	19	1114	26	1629	9
8	0.1020	0.0005	1.68E-06	6.83E-07	3.6117	0.1956	0.2561	0.0138	0.9955	0.1023	0.0052	1552	42	1470	70	1666	10
9	0.0921	0.0008	3.96E-06	6.31E-07	1.7330	0.0448	0.1362	0.0033	0.9368	0.0923	0.0090	1021	17	823	19	1473	17
11	0.1030	0.0007	1.86E-05	3.05E-06	2.5203	0.1626	0.1774	0.0114	0.9950	0.1030	0.0064	1278	46	1053	62	1679	12
12	0.1030	0.0004	2.30E-06	3.72E-07	2.3764	0.0881	0.1669	0.0062	0.9951	0.1033	0.0037	1236	26	995	34	1683	7
13	0.0980	0.0005	3.51E-06	5.91E-07	2.4747	0.0426	0.1828	0.0030	0.9564	0.0982	0.0050	1265	12	1082	16	1590	9
1050-424B																	
1_U2	0.0845	0.0004	-4.14E-07	2.94E-08	1.4162	0.0707	0.1221	0.0061	0.9958	0.0841	0.0004	896	29	743	35	1295	9
2_U2	0.0753	0.0014	3.37E-09	2.97E-09	0.8818	0.0278	0.0853	0.0022	0.8138	0.0750	0.0014	642	15	527	13	1069	36
3_U1	0.0842	0.0002	2.49E-07	9.45E-08	1.6060	0.0471	0.1390	0.0041	0.9973	0.0838	0.0002	973	18	839	23	1288	4
4_U1	0.0875	0.0002	-1.90E-07	8.19E-09	2.3364	0.0553	0.1944	0.0046	0.9958	0.0872	0.0002	1223	17	1145	25	1364	4
5_U1	0.0828	0.0003	-3.21E-07	3.44E-09	1.1641	0.0275	0.1024	0.0024	0.9872	0.0825	0.0003	784	13	628	14	1257	7
6_U1	0.0816	0.0007	7.90E-10	5.50E-10	1.4373	0.0474	0.1283	0.0466	0.9836	0.0813	0.0085	905	28	778	34	1228	17
7_U1	0.0874	0.0006	1.62E-08	1.49E-07	1.2838	0.0307	0.1070	0.0300	0.9780	0.0870	0.0064	839	17	655	19	1361	12
8_U1	0.0886	0.0003	2.81E-07	1.85E-07	1.9451	0.0220	0.1598	0.0216	0.9853	0.0883	0.0037	1097	15	956	19	1388	7
9_U1	0.0847	0.0004	2.78E-07	1.81E-07	1.2228	0.0237	0.1052	0.0232	0.9784	0.0843	0.0049	811	13	645	14	1299	9
10_U2	0.0860	0.0003	1.77E-07	4.10E-07	1.7456	0.0422	0.1479	0.0035	0.9911	0.0856	0.0003	1026	15	889	20	1329	6
12_U2	0.0744	0.0005	-3.21E-07	3.44E-09	0.7027	0.0166	0.0688	0.0015	0.9538	0.0741	0.0005	540	10	429	9	1045	14
15_U2	0.0747	0.0007	1.04E-07	9.72E-07	0.8434	0.0407	0.0823	0.0039	0.9785	0.0744	0.0007	621	22	510	23	1051	20
730-459.7																	
c1-1	0.0568	0.0001	0.00E+00	0.00E+00	0.4633	0.0165	0.0594	0.0021	0.9973	0.0565	0.0001	387	11	372	13	474	6
c1-2	0.0569	0.0002	-1.14E-06	1.99E-07	0.6218	0.0279	0.0796	0.0036	0.9980	0.0567	0.0002	491	17	493	21	480	6
c1-3	0.0566	0.0001	-1.14E-09	2.44E-10	0.5251	0.0200	0.0676	0.0026	0.9989	0.0563	0.0001	429	13	422	15	466	4
c1-4	0.0569	0.0001	-7.59E-10	2.93E-10	0.5542	0.0212	0.0709	0.0027	0.9987	0.0567	0.0001	448	14	442	16	479	4
c1-5	0.0566	0.0002	-4.55E-07	1.17E-08	0.4968	0.0198	0.0640	0.0025	0.9972	0.0563	0.0002	410	13	400	15	466	7
c1-6	0.0566	0.0001	-9.19E-10	3.95E-10	0.4871	0.0126	0.0627	0.0016	0.9989	0.0563	0.0001	403	9	392	10	466	3
c1-7	0.0567	0.0001	-4.56E-07	2.10E-08	0.4608	0.0173	0.0592	0.0022	0.9982	0.0564	0.0001	385	12	371	14	470	5
c1-8	0.0564	0.0002	0.00E+00	0.00E+00	0.4573	0.0148	0.0591	0.0019	0.9946	0.0561	0.0002	382	10	370	12	457	7
c1-9	0.0566	0.0002	-6.14E-10	2.04E-10	0.5173	0.0216	0.0666	0.0028	0.9977	0.0564	0.0002	423	14	415	17	467	6
c1-10	0.0567	0.0001	-4.22E-10	1.48E-10	0.5352	0.0117	0.0688	0.0015	0.9991	0.0564	0.0001	435	8	429	9	469	2
c1-12	0.0567	0.0002	0.00E+00	0.00E+00	0.5244	0.0185	0.0674	0.0024	0.9939	0.0564	0.0002	428	12	421	14	469	9
c1-13	0.0565	0.0002	-1.17E-06	2.44E-08	0.4435	0.0104	0.0571	0.0013	0.9867	0.0563	0.0002	373	7	358	8	465	8
c1-14	0.0563	0.0002	-2.29E-09	2.99E-07	0.4630	0.0175	0.0599	0.0023	0.9961	0.0561	0.0002	386	12	375	14	456	7
c1-15	0.0565	0.0001	-1.71E-09	8.66E-10	0.5042	0.0145	0.0650	0.0019	0.9969	0.0562	0.0001	415	10	406	11	462	5
c1-16	0.0570	0.0001	0.00E+00	0.00E+00	0.5854	0.0133	0.0748	0.0017	0.9990	0.0567	0.0001	468	8	465	10	481	2
c1-11	0.0566	0.0002	-1.48E-09	3.31E-10	0.3030	0.0144	0.0390	0.0018	0.9976	0.0564	0.0002	269	11	246	11	468	7
c2-3	0.0574	0.0001	2.51E-05	1.03E-06	0.5480	0.0171	0.0699	0.0022	0.9978	0.0568	0.0001	444	11	436	13	485	4
c2-15	0.0569	0.0002	2.07E-05	1.05E-06	0.5545	0.0208	0.0714	0.0027	0.9968	0.0563	0.0002	448	13	445	16	465	6

Appendix Table 5
Electron microprobe analyses of uraninite.

Sample: S3PD-		759 408.0 m (U1)		1050 424.0 m (U1 and U2)		730 459.6 m (U3)		730 459.7 m (U3)	
Analyses (n)	1 (oldest)	5	1 σ	8	1 σ	14	1 σ	28	1 σ
SiO_2 (wt.%)	<D.L.	0.14	0.19	0.60	0.14	0.53	0.20	0.52	0.17
CaO	2.69	2.6	0.10	2.28	0.11	1.82	0.28	1.69	0.30
Y_2O_3	0.29	0.32	0.10	0.38	0.09	0.39	0.06	0.51	0.07
ThO_2	<D.L.	<D.L.		<D.L.		<D.L.		<D.L.	
UO_2	75.62	74.99	0.57	84.94	0.88	87.85	0.68	87.79	0.98
PbO	19.79	18.78	1.17	8.57	1.04	5.56	0.80	5.32	0.37
Sc_2O_3	<D.L.	<D.L.		<D.L.		0.11 (13)	0.03	0.11 (27)	0.02
TiO_2	1.57	0.69	0.63	0.41	0.16	0.16 (13)	0.10	0.06 (27)	0.02
MnO	<D.L.	0.01	0.01	0.27	0.02	0.19	0.04	0.19	0.04
FeO	1.14	0.58	0.48	0.34	0.10	0.14	0.02	0.13	0.02
Eu_2O_3	<D.L.	<D.L.		<D.L.		<D.L.		<D.L.	
Yb_2O_3	0.04	0.04	0.01	0.05	0.01	0.04	0.01	0.05	0.02
P_2O_5	0.11	0.05 0.04	0.04	0.09	0.02	0.08 0.04	0.02	0.08 0.02	0.01
V_2O_3	0.04	(2)	0.01	<D.L.		(30)	0.02	(1)	
NiO	<D.L.	<D.L.		<D.L.		<D.L.		<D.L.	
ZrO_2	0.01	<D.L.		<D.L.		<D.L.		<D.L.	
MoO_3	<D.L.	<D.L.		<D.L.		<D.L. 0.05		<D.L.	
Ce_2O_3	<D.L.	0.03		0.05	0.02	(24)	0.01	0.03	0.03
Dy_2O_3	<D.L.	<D.L.		<D.L.		<D.L.		<D.L.	
WO_3	0.01	<D.L.		<D.L.		0.21	0.03	0.17	0.02
Total	101.3	98.32		98.02		97.15		96.71	
Chemical age (Ga)	1.646	1.586	0.087	0.708	0.086	0.456	0.063	0.438	0.028

<D.L. = below detection limit.
U1, U2, U3 = uraninite generation.

Fisher, L.A., Cleverley, J.S., Pownceby, M., MacRae, C., 2013. 3D representation of geochemical data, the corresponding alteration and associated REE mobility at the Ranger uranium deposit, Northern Territory, Australia. Mineral. Deposita 48 (8), 947–966.

Fontes, J.C., Matray, J.M., 1993. Geochemistry and origin of formation brines from the Paris Basin, France: 1. Brines associated with Triassic salts. Chem. Geol. 109, 149–175. http://dx.doi.org/10.1016/0009-2541(93)90068-T.

Fournier, R.O., 1985. The Behaviour of Silica in Hydrothermal Systems. In: Berger, B.R., Bethke, P.M. (Eds.), Geology and Geochemistry of Epithermal Systems. Reviews in Economic Geology vol. 2, pp. 45–61.

Gaboreau, S., Beaufort, D., Vieillard, P., Patrier, P., Bruneton, P., 2005. Aluminum phosphate–sulfate minerals associated with Proterozoic unconformity-type uranium deposits in the East Alligator River Uranium Field, Northern Territory, Australia. Can. Mineral. 43 (2), 813–827.

Gaboreau, S., Cuney, M., Quirt, D., Patrier, P., Mathieu, R., 2007. Significance of aluminum phosphate-sulfate minerals associated with U unconformity-type deposits: the Athabasca Basin, Canada. Am. Mineral. 92 (2-3), 267–280.

Giddings, J.W., Idnurm, M., 1993. Significance of overprint magnetizations in the Palaeoproterozoic Kombolgie Formation, western McArthur Basin, NT. Explor. Geophys. 24 (2), 231–238.

Grant, J.A., 1986. The isocon diagram; a simple solution to Gresens' equation for metasomatic alteration. Econ. Geol. 81 (8), 1976–1982.

Gustafson, L.B., Curtis, L.W., 1983. Post-Kombolgie metasomatism at Jabiluka, Northern Territory, Australia, and its significance in the formation of high-grade uranium mineralization in lower Proterozoic rocks. Econ. Geol. 78 (1), 26–56.

Hecht, L., Cuney, M., 2000. Hydrothermal alteration of monazite in the Precambrian crystalline basement of the Athabasca Basin (Saskatchewan, Canada): implications for the formation of unconformity-related uranium deposits. Mineral. Deposita 35, 791–795.

Hegge, M.R., Mosher, D.V., Eupene, G.S., Anthony, P.J., 1980. Geologic Setting of the East Alligator Uranium Deposits and Prospects. In: Ferguson, J., Gobely, A.B. (Eds.), Uranium in the Pine Creek Geosyncline. International Atomic Energy Agency, Vienna, pp. 259–272.

Hein, K.A.A., 2002. Geology of the Ranger uranium mine: Northern Territory, Australia: structural constraints on the timing of uranium emplacement. Ore Geol. Rev. 20, 83–108.

Hiatt, E.E., Kyser, T.K., 2000. Links between depositional and diagenetic processes in basin analysis: porosity and permeability evolution in sedimentary rocks. Fluid Basin Evol. Mineral. Assoc. Can. Short Course 28, 1–18.

Hiatt, E.E., Kyser, T.K., Fayek, M., Polito, P., Holk, G.J., Riciputi, L.R., 2007. Early quartz cements and evolution of paleohydraulic properties of basal sandstones in three Paleoproterozoic continental basins: evidence from *in situ* $\delta^{18}O$ analysis of quartz cements. Chem. Geol. 238 (1), 19–37.

Hills, J.H., Richards, J.R., 1976. Pitchblende and galena ages in the Alligator Rivers region, Northern Territory, Australia. Mineral. Deposita 11, 133–154.

Hoeve, J., Sibbald, T.I., 1978. On the genesis of Rabbit Lake and other unconformity-type uranium deposits in northern Saskatchewan, Canada. Econ. Geol. 73 (8), 1450–1473.

Hollis, J.A., Wygralak, A.S., 2012. A review of the geology and uranium, gold and iron ore deposits of the Pine Creek Orogen. Episodes News Mag. Int. Union Geol. Sci. 35 (1), 264.

Hollis, J.A., Carson, C.J., Glass, L.M., 2009. SHRIMP U–Pb zircon geochronological evidence for Neoarchean basement in western Arnhem Land, northern Australia. Precambrian Res. 174 (3), 364–380.

Hollis, J.A., Glass, L.M., Carson, C.J., Armstrong, R., Yaxley, G., Kemp, A.I.S., ... Phillips, D., 2011. The geological evolution of the Pine Creek Orogen: new pieces in the puzzle on orogen and craton scale. Annual Geoscience Exploration Seminar (AGES) (pp. 2011-003).

Idnurm, M., 2000. Towards a high resolution Late Palaeoproterozoic–earliest Mesoproterozoic apparent polar wander path for northern Australia. Aust. J. Earth Sci. 47 (3), 405–429.

Jackson, M.J., Scott, D.L., Rawlings, D.J., 2000. Stratigraphic framework for the Leichhardt and Calvert Superbasins: review and correlations of the pre-1700 Ma successions between Mt Isa and McArthur River. Aust. J. Earth Sci. 47 (3), 381–403.

James, R.H., Allen, D.E., Seyfried Jr., W.E., 2003. An experimental study of alteration of oceanic crust and terrigenous sediments at moderate temperatures (51 to 350 C): insights as to chemical processes in near-shore ridge-flank hydrothermal systems. Geochim. Cosmochim. Acta 67 (4), 681–691.

Jefferson, C.W., Thomas, D.J., Gandhi, S.S., Ramaekers, P., Delaney, G., Brisbin, D., Cutts, C., Quirt, D., Portella, P., Olson, R.A., 2007. Unconformity-Associated Uranium Deposits of the Athabasca Basin, Saskatchewan and Alberta. In: Goodfellow, W.D. (Ed.), Mineral Deposits of Canada: A Synthesis Of Major Deposit Types, District Metallogeny, The Evolution Of Geological Provinces, And Exploration Methods. Geological Assoiciation of Candada, Special Publication 5, pp. 273–305.

Johnston, D.J. 1984. Structural evolution of the Pine Creek inlier and mineralization therein. Unpublished PhD thesis, Monash University, 293 p.

Kendall, C.J., 1990. Ranger uranium deposits. In: Hughes, F.E. (Ed.), Geology of the mineral deposits of Australia and Papua New Guinea. The Australasian Institute of Mining and Metallurgy 1, pp. 799–805.

Kister P., 2003. Mobilité des éléments géochimiques dans un bassin sédimentaire clastique, du Protérozoïque à nos jours: le bassin Athabasca (Saskatchewan, Canada). Unpublished PhD thesis, INPL, p 333.

Kotzer, T.G., Kyser, T.K., 1995. Petrogenesis of the Proterozoic Athabasca Basin, northern Saskatchewan, Canada, and its relation to diagenesis, hydrothermal uranium mineralization and paleohydrogeology. Chem. Geol. 120 (1), 45–89.

Kyser, T.K., Wilson, M.R., Ruhrmann, G., 1989. Stable isotope constraints on the role of graphite in the genesis of unconformity-type uranium deposits. Can. J. Earth Sci. 26 (3), 490–498.

Kyser, T.K., Cuney, M., 2009. Unconformity-Related Uranium Deposits. In: Cuney, M., Kyser, T.K. (Eds.), Recent and Not-So-Recent Developments in Uranium Deposits and Implications for Exploration. Mineralogical Association of Canada Short Course Series 39, pp. 161–219.

Ludwig, K.R., 1999. Isoplot/ex version 2.1.0. A geochronological toolkit for Microsoft Excel. Special Publication no. 1a. Berkeley Geochronological Center.

Ludwig, K.R., 2001. SQUID 1.03, A User's Manual. Berkeley Geochronology Center Special Publication No. 2 (19 pp.).

Ludwig, K.R., 2003. Isoplot 3.00: A Geochronological Toolkit for Microsoft Excel. Berkeley Geochronology Center Special Publication No. 4 (70 pp.).

Ludwig, K.R., Grauch, R.I., Nutt, C.J., Nash, J.T., Frishman, D., Simmons, K.R., 1987. Age of uranium mineralization at the Jabiluka and Ranger uranium deposits, Northern Territory, Australia: new U–Pb isotope evidence. Econ. Geol. 82, 857–874.

Maas, R., 1989. Nd–Sr isotopic constraints on the age and origin of unconformity-type uranium deposits in the Alligator Rivers uranium field, Northern Territory, Australia. Econ. Geol. 84, 64–90.

Macdonald, C.C. 1980. Mineralogy and Geochemistry of a Precambrian Regolith in the Athabasca Basin. Unpublished M.Sc. thesis, University of Saskatchewan, (151 pp.)

McCready, A.J., Stumpfl, E.F., Lally, J.H., Ahmad, M., Gee, R.D., 2004. Polymetallic mineralisation at the Browns Deposit, Rum Jungle Mineral Field, Northern Territory, Australia. Econ. Geol. 99, 257–277.

McCready, A.J., Stumpfl, E.F., Melcher, F., 2003. U/Th-rich bitumen in Archean granites and Paleoproterozoic metasediments, Rum Jungle Mineral Field, Australia. Geofluids 3, 147–159.

Mercadier, J., Richard, A., Boiron, M.C., Cathelineau, M., Cuney, M., 2010. Migration of brines in the basement rocks of the Athabasca Basin through microfracture networks (P-Patch U deposit, Canada). Lithos 115 (1), 121–136.

Mercadier, J., Richard, A., Cathelineau, M., 2012. Boron-and magnesium-rich marine brines at the origin of giant unconformity-related uranium deposits: $\delta^{11}B$ evidence from Mg-tourmalines. Geology 40 (3), 231–234.

Mercadier, J., Annesley, I.R., McKechnie, C.L., Bogdan, T.S., Creighton, S., 2013a. Magmatic and metamorphic uraninite mineralization in the western margin of the Trans-Hudson Orogen (Saskatchewan, Canada): a uranium source for unconformity-related uranium deposits? Econ. Geol. 108 (5), 1037–1065.

Mercadier, J., Skirrow, R.G., Cross, A.J., 2013b. Uranium and gold deposits in the Pine Creek Orogen (North Australian Craton): a link at 1.8 Ga? Precambrian Res. 238, 111–119.

Miller, A.R., Needham, R.S., Stuart-Smith, P.G., 1992. Mineralogy and Geochemistry of the Pre-1.65 Ga paleosol under Kombolgie Formation sandstone of the Pine Creek Geosyncline, Northern Territory, Australia. Early Organic Evolution. Springer Berlin Heidelberg, pp. 76–105.

Needham, R.S., 1988. Geology of the Alligator Rivers Uranium Field, Northern Territory. Bureau of Mineral Resources, Geology and Geophysics, Bulletin 224 (Canberra).

Ng, R., Alexandre, P., Kyser, K., Cloutier, J., Abdu, Y.A., Hawthorne, F.C., 2013. Oxidation state of iron in alteration minerals associated with sandstone-hosted unconformity-related uranium deposits and apparently barren alteration systems in the Athabasca Basin, Canada: implications for exploration. J. Geochem. Explor. 130, 22–43.
Norrish, K., Chappell, B.W., 1977. X-ray Fluorescence Spectrometry. In: Zussman, J. (Ed.), Physical Methods in Determinative Mineralogy, 2nd edition Academic press, London, pp. 201–272.
Norrish, K., Hutton, J.T., 1969. An accurate X-ray spectrographic method for the analysis of a wide rage of geological samples. Geochim. Cosmochim. Acta 33, 431–453.
OECD, 2014. Uranium 2014: Resources, Production and Demand. Joint Report by OECD Nuclear Energy Agency and the International Atomic Energy Agency, NEA No. 7209.
Ojakangas, R.W., 1979. Sedimentation of the Basal Kombolgie Formation (Upper Precambrian-Carpentarian) Northern Territory, Australia: Possible Significance In The Genesis Of The Underlying Alligator Rivers Unconformity-Type Uranium Deposits (No. GJBX-173 (79)). Minnesota Univ., Duluth (USA) (Dept. of Geology).
Oliver, N.H., McLellan, J.G., Hobbs, B.E., Cleverley, J.S., Ord, A., Feltrin, L., 2006. 100th anniversary special paper: numerical models of extensional deformation, heat transfer, and fluid flow across basement-cover interfaces during basin-related mineralization. Econ. Geol. 101 (1), 1–31.
Page, R.W., Needham, R.S., Compston, W., 1980. Geochronology and Evolution of the Late-Archaean Basement and Proterozoic Rocks in the Alligator Rivers Uranium Field, Northern Territory, Australia. In: Ferguson, J., Gobely, A.B. (Eds.), Uranium in the Pine Creek Geosyncline. International Atomic Energy Agency, Vienna, pp. 39–68.
Page, R.W., 1996a. Samples 88126013, 88126029, 88126037, 88126038 (Kombolgie Formation). Geoscience Australia, 2014. Geochron Delivery System ((www.ga.gov.au/geochron-sapub-web/), accessed 31 October 2014).
Page, R.W. 1996b. Sample 88126035 (Oenpelli Dolerite). Unpublished data, Geochron Delivery System, Geoscience Australia. (Data not available from original source; reproduced in Table 1).
Palacky, G.J., 1987. Resistivity characteristics of geologic targets. In: Nabighian, M.N. (Ed.)-Electromagnetic methods in applied geophysics-theory 1. Society of Exploration Geophysicists, Tulsa, Oklahoma, pp. 53–129.
Polito, P.A., Kyser, T.K., Alexandre, P., Hiatt, E.E., Stanley, C.R., 2011. Advances in understanding the Kombolgie Subgroup and unconformity-related uranium deposits in the Alligator Rivers Uranium Field and how to explore for them using lithogeochemical principles. Aust. J. Earth Sci. 58 (5), 453–474.
Polito, P.A., Kyser, T.K., Marlatt, J., Alexandre, P., Bajwah, Z., Drever, G., 2004. Significance of alteration assemblages for the origin and evolution of the Proterozoic Nabarlek unconformity-related uranium deposit, Northern Territory, Australia. Econ. Geol. 99, 113–139.
Polito, P.A., Kyser, T.K., Thomas, D., Marlat, J., Drever, G., 2005. Re-evaluation of the petrogenesis of the Proterozoic Jabiluka unconformity-related uranium deposit, Northern Territory, Australia. Mineral. Deposita 40, 257–288.
Potma, W., Fisher, L., Schaubs, P., Cleverley, J., Corbel, S., Lau, I., Phang, C., Hough, R., 2012. JSU–ERA Ranger Mineral System Project Final Report. CSIRO National Research Flagships, Minerals Down Under. Northern Territory Geological Survey, Record 2012-004.
Pyke, J., 2000. Minerals laboratory staff develops new ICP-MS preparation method. AGSO Newsl. 33 (2000), 12–14.
Raffensperger, J.P., Garven, G., 1995. The formation of unconformity-type uranium ore deposits; 2, coupled hydrochemical modeling. Am. J. Sci. 295 (6), 639–696.
Richard, A., Pettke, T., Cathelineau, M., Boiron, M.C., Mercadier, J., Cuney, M., Derome, D., 2010. Brine–rock interaction in the Athabasca basement (McArthur River U deposit, Canada): consequences for fluid chemistry and uranium uptake. Terra Nova 22 (4), 303–308.
Schuhmacher, M., Fernandes, F., de Chambost, E., 2004. Achieving high reproducibility isotope ratios with the Cameca IMS 1270 in the multicollection mode. Appl. Surf. Sci. 231, 878–882.
Scott, D.L., Rawlings, D.J., Page, R.W., Tarlowski, C.Z., Idnurm, M., Jackson, M.J., Southgate, P.N., 2000. Basement framework and geodynamic evolution of the Palaeoproterozoic superbasins of north-central Australia: an integrated review of geochemical, geochronological and geophysical data. Aust. J. Earth Sci. 47 (3), 341–380.
Seewald, J.S., Seyfried, W.E., Thornton, E.C., 1990. Organic-rich sediment alteration: an experimental and theoretical study at elevated temperatures and pressures. Appl. Geochem. 5 (1), 193–209.
Seyfried, W.E., Mottl, M.J., 1982. Hydrothermal alteration of basalt by seawater under seawater-dominated conditions. Geochim. Cosmochim. Acta 46 (6), 985–1002.
Shapiro, L., Brannock, W.W., 1962. Rapid analysis of silicate, carbonate and phosphate rocks. U.S.G.S., Bulletin 1144-A.
Snelling, A.A., 1990. Koongarra uranium deposits. In: Hughes, F.E. (Ed.), The Geology of the Mineral Deposits of Australia and Papua New Guinea. Australasian Inst. Min. Metal.Monograph 14 vol. 1, pp. 807–812.
Solomon, M., Groves, D.I., 1994. The Geology and Origin of Australia's Mineral Deposits. Oxford University Press, Oxford.
Stacey, J.S., Kramers, J.D., 1975. Approximation of terrestrial lead isotope evolution by a two-stage model. Earth Planet. Sci. Lett. 26, 207–221.
Steiger, R.H., Jäger, E., 1977. Subcommision on geochronology: convention on the use of decay constants in geo- and cosmochronology. Earth Planet. Sci. Lett. 36, 359–362.
Stern, R.A., 1997. The GSC sensitive high resolution ion microprobe (SHRIMP): analytical techniques of zircon U–Th–Pb age determinations and performance evaluation. Radiogenic age and isotope studies. Report, 10.
Stuart-Smith, P.G., Needham, R.S., Page, R.W., Wyborn, L.A.I., 1993. Geology of mineral deposits of the Cullen mineral filed, Northern Territory. Aust. Geol. Surv. Organ. Bull. 229, 67–77.
Sweet, I.P., Brakel, A.T., Carson, L., 1999. The Kombolgie Subgroup a new look at an old formation. J. Earth Sci. 45 (219), 232.
Thorne, J.P., Highet, L.M., Cooper, M., Claoué-Long, J.C., Hoatson, D.M., Jaireth, S., Huston, D.L., Gallagher, R., 2014. The Australian Mafic–Ultramafic Magmatic Events GIS Dataset: Archean, Proterozoic and Phanerozoic Magmatic Events. Geoscience Australia, Canberra. http://dx.doi.org/10.4225/25/54125552CDA7C.
Weis, P., 2014. The Physical Hydrology of ore-Forming Magmatic-Hydrothermal Systems. In: Kelly, K.D., Golden, H.C. (Eds.), Building Exploration Capability for the 21st Century. Society of Economic Geologists, Special Publication Number 18, pp. 59–73.
Wilde, A.R., Wall, V.J., 1987. Geology of the Nabarlek uranium deposit, Northern Territory, Australia. Econ. Geol. 82 (5), 1152–1168.
Wilde, A.R., Mernagh, T.P., Bloom, M.S., Hoffmann, C.F., 1989. Fluid inclusion evidence on the origin of some Australian unconformity-related uranium deposits. Econ. Geol. 84 (6), 1627–1642.
Williams, I.S., 1998. U-Th-Pb geochronology by ion microprobe. In: McKibben, M.A., Shanks III, W.C., Ridley, W.I. (Eds.), Reviews of microanalytical techniques to understanding mineralising processes. 7, pp. 1–35.
Wilson, M.R., Kyser, T.K., 1987. Stable isotope geochemistry of alteration associated with the Key Lake uranium deposit, Canada. Econ. Geol. 82 (6), 1540–1557.
Wood, D.A., 1980. The application of a ThHfTa diagram to problems of tectonomagmatic classification and to establishing the nature of crustal contamination of basaltic lavas of the British Tertiary Volcanic Province. Earth Planet. Sci. Lett. 50 (1), 11–30.
Worden, K., Carson, C., Scrimgeour, I., Lally, J., Doyle, N., 2008. A revised Palaeoproterozoic chronostratigraphy for the Pine Creek Orogen, northern Australia: evidence from SHRIMP U–Pb zircon geochronology. Precambrian Res. 166, 122–144.
Wyborn, L.A.I., Bastrakova, I.V., Budd, A.R., 1998. Australian Proterozoic granites — characteristics, sources and possible mechanisms for derivation and emplacement. AGSO Record 1998/33, pp. 47–49.